

**Interaction between large deformation plasticity and strain-induced phase transformation
at high pressures and large deformations**

by

Mehdi Kamrani

A dissertation submitted to the graduate faculty
in partial fulfillment of the requirements for the degree of

DOCTOR OF PHILOSOPHY

Major: Engineering Mechanics

Program of Study Committee:
Valery I. Levitas, Major Professor
Ashraf Bastawros
Liming Xiong
Azadeh Sheidaei
Pranav Shrotriya

The student author, whose presentation of the scholarship herein was approved by the program of study committee, is solely responsible for the content of this dissertation. The Graduate College will ensure this dissertation is globally accessible and will not permit alterations after a degree is conferred.

Iowa State University

Ames, Iowa

2020

Copyright © Mehdi Kamrani, 2020. All rights reserved.

DEDICATION

I would like to dedicate this dissertation to my rock climbing shoes that helped me stay happy when it was very hard.

TABLE OF CONTENTS

	Page
ACKNOWLEDGMENTS	v
ABSTRACT.....	vi
CHAPTER 1. INTRODUCTION	1
References	4
CHAPTER 2. FEM SIMULATION OF LARGE DEFORMATION OF COPPER IN THE QUASI-CONSTRAIN HIGH-PRESSURE-TORSION SETUP	8
Abstract.....	8
Introduction	9
Problem Formulation.....	11
Geometry and boundary conditions	11
Material Model	12
Friction Model.....	15
Material Parameters and Numerical Procedure.....	17
Evolution of Stress and Plastic Strain Fields during HPT.....	19
Effect of the Different Contact Conditions.....	33
Effect of the Material Properties	37
Concluding Remarks	39
Acknowledgements	41
References	41
CHAPTER 3. COUPLED STRAIN-INDUCED ALPHA TO OMEGA PHASE TRANSFORMATION AND PLASTIC FLOW IN ZIRCONIUM UNDER HIGH PRESSURE TORSION IN A ROTATIONAL DIAMOND ANVIL CELL.....	47
Abstract.....	47
Introduction	48
Problem Formulation.....	52
Geometry and Boundary Conditions.....	52
Material Model	53
Friction Model.....	55
Material Parameters and Numerical Procedure.....	58
Study of Coupled Plastic Flow and Phase Transformations.....	59
Distribution of the Pressure and Volume Fraction of the ω Phase	59
Distribution of the Normal and Shear Stresses	66
Contact Sliding, Deformation of an Anvil, and Reduction in Sample Thickness.....	69
Concluding Remarks	73
Acknowledgements	77
Data Availability.....	77
References	77

CHAPTER 4. TENSORIAL STRESS-STRAIN FIELDS, LARGE ELASTOPLASTICITY, AND FRICTION IN DIAMOND ANVIL CELL UP TO 400 GPA	82
Abstract.....	82
Introduction	83
Model.....	85
Results	86
Concluding Remarks	94
Methods	96
Geometry and Boundary Conditions.....	96
Friction Model.....	96
Elastoplastic Material Model under Large Strains and High Pressure.....	97
Nonlinear Isotropic Elasticity for Sample.....	100
Nonlinear Anisotropic Elasticity for Diamond	100
Material Properties	101
Geometric Interpretation of the Postulate of Perfect Plasticity [24]	103
Data Availability.....	103
Acknowledgements	104
Competing interests	104
Author Contributions	104
References	104
CHAPTER 5. IMAGING STRESS AND MAGNETISM AT HIGH PRESSURES USING A NANOSCALE QUANTUM SENSOR.....	109
Abstract.....	109
References	124
Acknowledgments	126
Funding.....	127
Author Contributions.....	127
Competing Interests.....	128
Data and Materials Availability.....	128
Supplementary Materials	128
Finite Element Simulations of the Stress Tensor.....	128
CHAPTER 6. CONCLUSION.....	132

ACKNOWLEDGMENTS

I would like to thank my Ph.D.'s supervisor Prof. Valery I. Levitas for his continuous intellectual and financial support. I would have been unable to finish my projects without his constant guidance and support.

I would like to thank Dr. Biao Feng and also my committee members, Dr. Ashraf Bastawros, Liming Xiong, Azadeh Sheidaei, and Pranav Shrotriya.

ABSTRACT

Large plastic deformation of materials result in the ultrafine-grained materials with highly improved properties, like a combination of high ductility and high strength. The high-pressure-torsion (HPT) is the most effective severe plastic deformation technique that is widely used for producing nanograined materials and promotion of the phase transformations in various materials. Diamond anvil cell (DAC) and rotational diamond anvil cell (RDAC) are powerful tools to generate high pressure and large shear and in-situ studying material behavior including the phase transformations under extreme conditions. Constitutive models and finite element method (FEM) algorithms are developed, and FEM simulations are performed to study: (a) behavior of a copper sample in a HPT setup, and (b) plastic straining and strain-induced phase transformation in zirconium in different HPT setups and also in DAC and RDAC. Various experimental data are interpreted and the effect of different setups on the phase transformation is investigated. Majority of measurements and discussions about processes in DAC are related to pressure only. However, study of physical, chemical, geological, and mechanical phenomena, and synthesis of new phases in a sample, as well as the increasing range of achievable pressures, depend on knowledge of all components of the stress and plastic strain tensors. A coupled experimental-theoretical-computational approach is proposed to determine and verify all stress and plastic strain tensorial fields, elastoplastic properties, and contact friction rules for a tungsten sample at different pressures up to 382 GPa.

CHAPTER 1. INTRODUCTION

Introducing plastic strain into a sample results in the production of ultrafine-grained (UFG) materials [1-3] with highly improved properties, like a combination of high ductility and high strength [4, 5]. However, in addition to plastic strain the grain refinement is highly influenced by applied pressure. The high-pressure-torsion (HPT) technique is the most effective severe plastic deformation (SPD) technique that is widely used for materials treatment. Also, HPT promotes the phase transformation (PT) [6-10] in various materials. The essential downside of the HPT technique is that in-situ measurement is not an option as the dies are not transparent. Besides, even though the anvils are made of very strong materials (e.g. tungsten carbide) there will be plastic deformation accumulating in the anvils making the tests unrepeatable. On the other hand, the maximum achievable pressure is relatively low. A diamond anvil cell (DAC) is a powerful tool to generate high pressure and large shear and in-situ study of material behavior under extreme conditions using modern diagnostics, like x-ray, Raman, and optical techniques [11-13]. However, the size of the sample in DAC is limited to the size of the diamond. In order to study the behavior of a material at a larger scale, HPT is usually used.

Phase transformations under high pressure and plastic shear are widespread in nature and also modern technologies. For examples, deep earthquakes are related to the instability due to shear strain-induced PT; the synthesis of various chemical compounds by ball milling is caused by strain-induced PTs. DAC is widely used to study the PTs to high pressure phases at very large pressures (e.g. 400 GPa [14]) and very large deformation (e.g. 3 order of magnitude thickness reduction [14]). A rotational diamond anvil cell (RDAC), in which a large plastic shear in the sample without a hydrostatic medium is imposed by the rotation of anvils under a fixed axial compressive load [6,15-18], is utilized to study the effect of the plastic shear on PTs under high

pressure. It is known from numerous experiments that the addition of plastic shear, due to the rotation of an anvil, leads to numerous exciting phenomena such as: (1) a significant reduction of transformation pressure by a factor of 2-5 in Refs. [6,19,20] and even by a factor of nearly 100 [21], in comparison with those under a hydrostatic or nearly-hydrostatic condition; (2) the substitution of reversible PTs by irreversible ones [6-9,19,20], which allows one to retain high-pressure phases for possible practical applications; (3) the appearance of new high-pressure phases [6,9,22], which could not be obtained without plastic shear; (4) a reduction in a transformation pressure hysteresis sometimes to zero [23,24]; (5) fast, strain-controlled rather than time-controlled kinetics, in which plastic strain plays the role of a time-like parameter [6-9].

Most measurements in and discussions about processes in DAC are related to pressure only, however, it is evident that elastic deformation and fracture of the diamond and plastic flow of a sample and gasket depend on all components of the stress tensor. Various problems, such as the study of physical, chemical, geological, and mechanical phenomena and synthesis of new phases in a sample, as well as the increasing range of achievable pressures, are related to knowledge of the fields of all components of the stress, elastic, and plastic strain tensors in DAC. Contact friction between diamond and sample/gasket plays a key role in generating high pressure without fracture of the diamond. It is also well-known that phase transformations and chemical reactions in solids depend not only on pressure, but also on the deviatoric stresses and plastic strains [6,7,16,25-28]. All of these fields are extremely complex and heterogeneous, e.g. with normal stresses varying by megabar over $20\ \mu\text{m}$ [14, 29]. A coupled experimental-theoretical-computational approach can be used to determine all stress and plastic strain tensorial fields, elastoplastic properties, and contact friction rules. Such an approach suggests that all fields which can be measured should be measured. Physics-based models for elastoplastic behavior and

contact friction should be iteratively developed and refined, and all material properties should be calibrated by fitting to some experimental fields and verified by comparison with other experimental fields. With these properties, simulations provide all fields, including components of the stress and plastic strain tensors, friction stress, etc., i.e. those which cannot be directly measured. Such a model is used to reproduce the experimental pressure and thickness distribution of a tungsten (W) sample at different pressures up to 382 GPa and provide distribution of all components of stress and plastic strain tensors in the W sample and also diamond.

Recently a novel method is proposed to extract the distribution of components of stress tensor in DAC in an in-situ measurement. A similar coupled experimental-theoretical-computational procedure can be used to determine the contact pressure and the friction condition in order to reproduce the experimental stress distribution over the diamond anvil and verify the proposed procedure of measuring the component of the stress tensor. Then this numerical method, provides the distribution of all components of stress tensor within the diamond.

This thesis is organized as follows:

In Chapter 2, behavior of a copper sample is studied in a quasi-constraint HPT setup. Combined Coulomb and plastic sliding conditions are considered which is much more realistic than in the previous HPT literature where plastic sliding was neglected. The stress-strain curve is parametrized using three material parameters: the yield strength of the annealed and fully strain-hardened material, and the critical strain for saturation of strain hardening, m . Different friction coefficients and saturation strains m have been utilized in simulations in order to obtain results the closest to the known experimental data.

In Chapter 3, the strain-induced PT in zirconium (Zr) from the α phase to the ω phase under compression and torsion in RDAC is studied. Here, we performed the first study of PT in the real material (i.e. Zr) in RDAC. The results obtained will be used in comparison with those for DAC [26], to interpret the experimental phenomena, and to suggest how to improve PT conditions in RDAC.

In Chapter 4, we suggest a coupled experimental-theoretical-computational approach that allowed us to refine, calibrate, and verify models for elastoplastic behavior and contact friction for tungsten (W) and diamond up to 400 GPa and reconstruct fields of all components of stress and large plastic strain tensors in W and diamond.

In Chapter 5, using equations from elasticity theory and the finite element approach, a numerical simulation is coded in ABAQUS for the stress and strain tensor fields in the diamond anvil cell. The diamond anvil cell is approximately axially symmetric about the diamond loading axis, in this case the crystallographic (111) axis (i.e. the Z axis). This permits us to improve simulation efficiency by reducing the initially 3D tensor of elastic moduli to the 2D axisymmetric cylindrical frame of the diamond. Normal and shear contact stresses along contact surfaces are determined from the best fit to the mean in-plane stress distribution $\sigma_{\perp} = 0.5(\sigma_{RR} + \sigma_{\theta\theta})$ measured in the experiment, then distribution of all components of stress tensor are determined within the diamond.

References

- [1] Pippan R., Scheriau S., Taylor A., Hafok M., Hohenwarter A., Bachmaier A., Saturation of fragmentation during severe plastic deformation, *Annu. Rev. Mater. Res.* 40 (2010) 319-343.
- [2] Zhilyaev A.P., Langdon T.G., Using high-pressure torsion for metal processing: fundamentals and applications, *Prog. Mater. Sci.* 53 (2008) 893-979.

- [3] Valiev R.Z., Estrin Y., Horita Z., Langdon T.G., Zechetbauer M.J., Zhu Y.T., Producing bulk ultrafine-grained materials by severe plastic deformation, *Nanostruct. Mater.* 58 (2006) 33-39.
- [4] Liddicoat P.V., Liao X.Z., Zhao Y., Zhu Y., Murashkin M.Y., Lavernia E.J., Valiev R.Z., Ringer S.P., Nanostructural hierarchy increases the strength of aluminium alloys, *Nat. Commun.* (2010) 1:63.
- [5] Dalla T.F., Lapovok R., Sandlin J., Thomson P.F., Davies C.H.J., Pereloma E.V., Microstructures and properties of copper processed by equal channel angular extrusion for 1–16 passes, *Acta Mater.* 52 (2004) 4819-4832.
- [6] Blank V.D., Estrin E.I., Phase transition in solids under high pressure, CRC Press, New York, 2017.
- [7] Levitas V.I., High-pressure mechanochemistry: conceptual multiscale theory and interpretation of experiments, *Phys. Rev. B* 70 (2004) 184118.
- [8] Levitas V.I., High-Pressure Phase Transformations under Severe Plastic Deformation by Torsion in Rotational Anvils, *Material Transactions*, 60 (2019), 1294-1301.
- [9] Levitas V.I., Continuum Mechanical Fundamentals of Mechanochemistry Section in: High Pressure Surface Science and Engineering, Institute of Physics, Bristol and Philadelphia, 2003.
- [10] Edalati K., Horita Z., A review on high-pressure torsion (hpt) from 1935 to 1988, *Mater. Sci. Eng., A*, 652 (2016) 325-352.
- [11] Duffy T. S., Shen G. Y., Heinz D. L., Shu J. F., Ma Y. Z., Mao H. K., Hemley R. J., and Singh A. K., Lattice strains in gold and rhenium under nonhydrostatic compression to 37 GPa., *Phys. Rev. B*, 60 (1999) 15063.
- [12] Lazicki A., Loubeyre P., Occelli F., Hemley R. J., and Mezouar M., Static compression of LiH to 250 GPa, *Phys. Rev. B* 85 (2012) 054103.
- [13] Nisr C., Ribarik G., Ungar T., Vaughan G. B. M., Cordier P., and Merkel S., High resolution three-dimensional X-ray diffraction study of dislocations in grains of MgGeO₃ post-perovskite at 90 GPa, *J. Geophys. Res.*, 117 (2012) B03201.
- [14] Li, B. Ji, C. Yang, W. Wang, J. Yang, K. Xu, R. Liu, W. Cai, Z. Chen, J. Mao, H. K. Diamond anvil cell behavior up to 4 mbar, *PNAS* 115 (2018) 1713-1717.
- [15] Levitas V.I., Ma Y., Selvi E., Wu J., Patten J.A., High-density amorphous phase of silicon carbide obtained under large plastic shear and high pressure, *Physical Review B*, 85 (2012) 054114.

- [16] Ji C., Levitas V.I., Zhu H., Chaudhuri J., Marathe A., Ma Y., Shear-Induced Phase Transition of Nanocrystalline Hexagonal Boron Nitride to Wurtzitic Structure at Room Temperature and Lower Pressure, *Proceedings of the National Academy of Sciences*, 109 (2012) 19108-19112.
- [17] Ma Y., Selvi E., Levitas V.I., Hashemi J., Effect of Shear Strain on the α - ϵ Phase Transition of Iron: A New Approach in the Rotational Diamond Anvil Cell, *Journal of Physics: Condensed Matter*, 18 (2006) S1075.
- [18] Levitas V.I., Ma Y., Hashemi J., Holtz M., Guven N., Strain-Induced Disorder, Phase Transformations, and Transformation-Induced Plasticity in Hexagonal Boron Nitride Under Compression and Shear in a Rotational Diamond Anvil Cell: In Situ X-Ray Diffraction Study and Modeling, *Journal of Chemical Physics*, 125 (2006) 044507.
- [19] Blank V.D., Boguslavsky Y.Y., Eremets M.I., Itskevich E.S., Konyaev Y.S., Shirokov A.M., Estrin E.I., Pressure Self-Multiplication Effect on Phase-Transition under Quasi-Hydrostatic Conditions, *Zhurnal Eksperimental'noi i Teoreticheskoi Fiziki* (ISSN 0044-4510), In Russian, 87 (1984) 922-926.
- [20] Novikov N.V., Polotnyak S.B., Shvedov L.K., Levitas V.I., Regularities of Phase Transformations and Plastic Straining of Materials in Compression and Shear on Diamond Anvils: Experiments and Theory, *Journal of Superhard Materials*, 21 (1999) 39-51.
- [21] Gao Y., Ma Y., An Q., Levitas V. I., Zhang Y., Feng B., Chaudhuri J. and Goddard III W. A., Shear driven formation of nano-diamonds at sub-gigapascals and 300 K, *Carbon* 146 (2019) 364e368.
- [22] Blank V., Popov M., Buga S., Davydov V., Ivlev A.N., Mavrin B.N., Ceolin R., Szwarc H., Rassat A., Is C60 Fullerite Harder than Diamond?, *Physics Letters A*, 188 (1994) 281-286.
- [23] Feng B., Levitas V.I., Ma Y., Strain-Induced Phase Transformation under Compression in a Diamond Anvil Cell: Simulations of a Sample and Gasket, *Journal of Applied Physics*, 115 (2014) 163509.
- [24] Feng B., Levitas V.I., Zarechnyy O.M., Plastic Flows and Phase Transformations in Materials under Compression in Diamond Anvil Cell: Effect of Contact Sliding, *Journal of Applied Physics*, 114 (2013) 043506.
- [25] Bridgman, P. W. Effects of high shearing stress combined with high hydrostatic pressure. *Phys. Rev.* 48 (1935) 825–847.
- [26] Barge, N. V. Boehler, R. Effect of non-hydrostaticity on the α - ϵ transition of iron. *High Press. Res.* 6 (2006) 133–140.

- [27] Levitas, V. I. High pressure phase transformations revisited. *J. Physics: Condensed Matter* 30 (2018) 163001.
- [28] Levitas, V. I. Shvedov, L. K. Low pressure phase transformation from rhombohedral to cubic BN: experiment and theory. *Phys. Rev. B* 65 (2002) 104109.
- [29] Jeanloz, R. Godwal, B. K. Meade, C. Static strength and equation of state of rhenium at ultra-high pressures, *Nature* 349 (1991) 687-689.

CHAPTER 2. FEM SIMULATION OF LARGE DEFORMATION OF COPPER IN THE QUASI-CONSTRAIN HIGH-PRESSURE-TORSION SETUP

This Section reproduces paper Kamrani M. Levitas V.I., and Feng B., FEM simulation of large deformation of copper in the quasi-constrain high-pressure-torsion setup. Materials Science and Engineering A, 2017, Vol. 705, 219-230.

Abstract

High pressure-torsion (HPT) technique is widely used to introduce severe plastic deformation in order to obtain ultrafine-grained materials with improved properties or to enhance the phase transformation which may result in an appearance of new phases. The behavior of the copper sample under pressure and torsion in a quasi-constraint configuration is studied using finite element method (FEM). A complete system of equations for small elastic and large plastic deformations and rotations is presented. Contact friction conditions include combined Coulomb and plastic sliding. The evolution of the distribution of fields of components of the stress tensor, hydrostatic pressure, and equivalent plastic strain are studied. The effects of the critical strain for saturation of strain hardening, m , and different friction conditions are investigated. Strong heterogeneity of the plastic strain both along the radius and thickness of the sample is found, which is not well described by known approximate expressions. Torque-rotation angle response of the sample is not sensitive to the value of m but strongly depends on the friction coefficient between anvil and flash. The main conclusion is that the value of m obtained in literature from HPT (from 4.8 to 20) is highly overestimated and $m=1.57$ obtained in a homogeneous compression test should be used.

Keywords: High pressure-torsion (HPT), quasi-constraint setup, copper, severe plastic deformation, finite element simulation, contact friction.

Introduction

High pressure-torsion (HPT) technique is the most effective severe plastic deformation (SPD) technique that is widely used for materials treatment. Imposed plastic strain results in the production of ultrafine-grained (UFG) materials [1-3] with highly improved properties, like a combination of high ductility and high strength [4, 5]. However, in addition to plastic strain the grain refinement is highly influenced by applied pressure. Also, HPT promotes the phase transformation [6-9] in various materials. Thus, under superposition of a large plastic shear, the minimum required pressure at which phase transformation may occur reduces [6, 9-13] in comparison with hydrostatic conditions and new phases may appear [6-9, 14]. Based on the geometry of the anvils the HPT process can be divided into unconstraint, quasi-constraint, and constraint setups. Due to the nature of the unconstraint setup the material can easily flow radially which results in a high pressure gradient in the sample and high pressure at the central region. However, due to the material flow there is a large reduction in thickness of the sample. The pressure distribution becomes more uniform along the contact surface in the quasi-constraint and constraint setups and a larger sample thickness can be achieved. The focus of this study is HPT under the quasi-constraint setup. Results of this study can help in understanding and optimizing the process of grain size refinement and, in the future, phase transformation.

The distribution and evolution of different fields such as pressure and plastic strain with [15-20] and without [21] consideration of phase transformation is extensively studied for the unconstraint configurations. There are also numerous FEM simulations on the study of the temperature distribution [22, 23, 24], effect of the applied pressure [25, 26], sample size [27-29], friction coefficient [27-29], slop of the inclined anvil's surface [17, 28], and depth of the

depression in the anvils [30] on the material flow and distribution of the fields within the sample in the quasi-constraint configurations. Ref. [30] does not include the strain hardening of the material and a Coulomb friction model is considered along the entire contact surface. Refs. [27-29, 31-33] do not allow any plastic sliding along the contact surface. Besides, Ref. [27] treats a model material for which strain hardening does not saturate. As it is seen in Refs. [27, 28, 31-33], the sticking condition may result in uniform distribution of the equivalent plastic strain within the thickness of the sample at least away from the inclined surface of the anvil which is not the case if sliding is taken into account [24, 30, 34].

In this paper, combined Coulomb and plastic sliding conditions [15, 17, 20] are considered which is much more realistic than in the previous HPT literature where plastic sliding was neglected. The constitutive equations developed in [35, 36] are utilized in the ABAQUS FEM code [37]. The stress-strain curve is parametrized using three material parameters: the yield strength of the annealed and fully strain-hardened material, and the critical strain for saturation of strain hardening, m . Different friction coefficients and saturation strains m have been utilized in simulations in order to obtain results the closest to the known experimental data. The most important results from the point of view of material behavior is that the value of $m=1.57$ found in a strict experiment with homogeneous fields [9] should be used instead of the values in the range of 4.8 to 20 obtained in [38-40]. Significant errors in the interpretation of the experimental data was demonstrated due to strong heterogeneity of the plastic strain, which is different than what was assumed in the previous analytical models.

Problem Formulation

Geometry and boundary conditions

Figure 1 shows the main dimensions of the anvils and the sample consistent with the experimental setup in Ref. [41]. The flash which forms due to the deformation of the sample loses its contact with the anvils once it is 1.5mm long or more [41].

Due to the symmetry, just a quarter of the sample and the anvils is considered (Figure 1) in a generalized axisymmetric formulation, i.e., when geometry is axisymmetric but loading includes torsion. In order to avoid probable divergence problems a smooth transition is considered at the junction of the inclined surface and the lower flat surface of the anvils, with a radius of less than 0.1 of the depression size in the anvils.

In the experimental setup the upper anvil is fixed and torsion is applied on the lower anvil. In the simulations the rotation angle of the sample on the symmetry plane (the plane in the mid-thickness of the sample) is set to be zero and the applied rotation angle is half of that in the experiments.

The boundary conditions for the sample and the anvils are as follows:

A normal compressive load of $F=150$ kN [41] is applied on the top surface of the anvil in the compression step. This load remains fixed while an increasing rotation angle is applied to the upper anvil.

At the symmetry axis $r = 0$, the radial displacement $u_r = 0$ and the radial components of shear stress $\tau_{rz} = 0$. Also, at the symmetry plane ($z = 0$), the radial components of shear stress $\tau_{rz} = 0$, circumferential and the axial displacement are all zero $u_\phi = u_z = 0$.

On the contact surfaces between the sample and the anvil, a combined plastic and Coulomb friction model is used which is described below.

Other surfaces which are not mentioned above are stress-free.

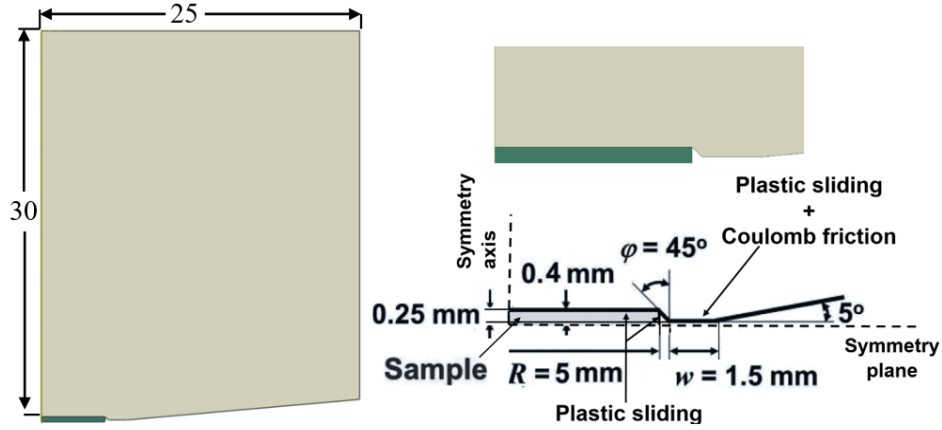


Figure 1. Main dimensions of the anvil and the sample. Due to the symmetry just a quarter of the geometries are shown.

Material Model

We consider initially-isotropic polycrystalline metals. Since the maximum pressure is only 3 GPa in this paper the pressure independency of the yield criteria is assumed. We assume isotropic elastic and plastic behavior, because there is no data that allows one to quantify the evolution of strain-induced anisotropy of elastic and plastic properties at large strains. Additional data justifying the neglect of plastic anisotropy was presented in [35, 36] for large accumulative plastic strain $q > 0.6 - 1$ and for deformation paths in the strain space without sharp changes in directions (monotonous deformation). Thus, it was found for more than 60 materials from various material classes (*e.g.*, metals and alloys, compacted powders, rocks, oxides, etc.) that above some critical q the polycrystalline, initially-isotropic materials deform as the perfectly plastic and isotropic ones with a strain-history-independent limit surface of the perfect plasticity. Additional confirmations under high pressure were presented in [42] for alloyed steel and NaCl. An isotropic perfectly plastic model offers a good comparison with the experiment on the pressure distribution in a rhenium sample compressed in a diamond anvil cell up to 300 GPa

[19]. The above results were extracted by analyzing nonuniform fields in a sample. In Ref. [43] uniform compression for six metals, including copper, for q up to 1.5 was performed, and perfectly plastic behavior was strictly demonstrated. Saturation of the strain hardening for metals is currently generally accepted, see review [9]; however, strain required for saturation varies significantly.

Below we present a model for small elastic and large plastic deformations and material rotations developed in [25, 36]. Tensors and vectors are denoted with bold face letters.

Decomposition of the deformation gradient ($\mathbf{F} = \partial \mathbf{r} / \partial \mathbf{r}_0$) into elastic \mathbf{F}_e and plastic \mathbf{F}_p parts:

$$\mathbf{F} = \mathbf{F}_e \cdot \mathbf{F}_p, \quad (1)$$

where \mathbf{r}_0 and \mathbf{r} are position vectors in the undeformed and deformed states.

Kinematic decomposition of the deformation rate \mathbf{d} :

$$\mathbf{d} = \left(\dot{\mathbf{F}} \cdot \mathbf{F}^{-1} \right)_s^{\nabla} = \boldsymbol{\varepsilon}_e + \mathbf{d}_p, \quad (2)$$

where $\boldsymbol{\varepsilon}_e$ is the objective Jaumann time derivative of the elastic strain, and subscript s denotes symmetrization.

Hooke's elasticity law:

$$\boldsymbol{\varepsilon}_e = \frac{1}{E} \left[\boldsymbol{\sigma} - \nu \left(\text{tr}(\boldsymbol{\sigma}) \mathbf{I} - \boldsymbol{\sigma} \right) \right], \quad \text{tr}(\boldsymbol{\sigma}) = \sigma_{rr} + \sigma_{zz} + \sigma_{\varphi\varphi}, \quad (3)$$

where $\boldsymbol{\sigma}$ is the true (Cauchy) stress tensor, E is the Young's modulus, and ν is the Poisson's ratio.

Stress-strain curve and yield criterion:

$$\sigma_i = \left(\frac{3}{2} \mathbf{s} : \mathbf{s} \right)^{0.5} \leq \sigma_y(q), \quad (4)$$

$$\begin{aligned} \sigma_y(q) &= \sigma_y^\infty + \frac{\sigma_{y0} - \sigma_y^\infty}{m^2} (q - m)^2 \quad \text{for } \frac{q}{m} \leq 1; \\ \sigma_y(q) &= \sigma_y^\infty \quad \text{for } \frac{q}{m} > 1. \end{aligned} \quad (5)$$

Equivalent plastic strain rate:

$$\dot{q} = \left(\frac{2}{3} \mathbf{d}_p : \mathbf{d}_p \right)^{0.5}, \quad (6)$$

Here σ_i is the effective stress, \mathbf{s} is the deviator of the Cauchy stress $\boldsymbol{\sigma}$, σ_y^∞ is the saturated (ultimate) yield strength, σ_{y0} is the initial yield strength at $q=0$, and m is the equivalent plastic strain above which material behaves as the perfectly plastic one.

J_2 flow rule:

$$\sigma_i = \sigma_y(q) \quad \text{and} \quad \mathbf{d}_p = \lambda \mathbf{s}, \quad \lambda \geq 0, \quad (7)$$

where λ is a parameter that is determined by iterative satisfaction of the yield condition.

Equilibrium equation:

$$\nabla \cdot \boldsymbol{\sigma} = 0 \quad (8)$$

There is a significant discrepancy in literature in the value of equivalent plastic strain m required for the transition to ideal plasticity [34, 38-41, 44, 45]. Thus, for homogeneous uniaxial compression in [43] $m=0.44$ for cast iron; m varies from 0.82 to 1.35 for different steels, and $m=1$ for copper. Parameter m in [43] was evaluated both by saturation of flow stress and hardness, which coincide. The equivalent plastic strain was determined as $q = \ln(H_0/H)$, where H_0 is the initial and H is the current height of the sample. Due to the homogeneity of stress-strain state, the results in [43] are strict.

However, the value of m is from several times to an order of magnitude larger in [43]. For example, for copper $m=4.8$ in [38] while it is 15 in [39] and is 20 in [40]. It should be mentioned that in Ref. [38] the material properties are given as a curve of hardness HV versus equivalent plastic strain. The yield strength is related to the hardness assuming $\sigma_y = HV/3$ [46], and equivalent plastic strain is determined as

$$q(r) = \frac{\gamma}{\sqrt{3}} = \frac{2\pi r N}{h_0 \sqrt{3}} \quad (9)$$

where N is the number of turns of the anvils, h_0 is the initial thickness of the sample and r is the distance from the center of the disk, and γ is plastic shear calculated for the traditional torsion problem. This equation is based on several strong assumptions which may introduce significant error in the value m and consequently the entire stress-strain curve. This topic will be discussed after obtaining the results of the simulation.

Friction Model

According to the Coulomb friction model there is no sliding between contact pairs unless shear stress reaches the critical shear stress $\tau_{crit} = \mu\sigma_c$, where μ is the friction coefficient and σ_c is the normal contact stress. In literature devoted to the simulation of HPT [27-29, 31-34, 41] cohesion and Coulomb friction model are used, neglecting plastic friction. For the plastic friction model if the shear stress reaches the yield strength in shear τ_y ($\tau_y = \sigma_y/\sqrt{3}$, based on von Mises yield criterion), regardless of the Coulomb friction model being satisfied, there will be plastic sliding between contact pairs. Therefore, critical friction is redefined [15, 17, 20] as

$\tau_{crit} = \min(\mu\sigma_c, \tau_y)$. Moreover, because in the current study plastic behavior of the copper sample includes strain hardening, the yield strength in shear is a function of the accumulated

plastic strain q , which was not considered in the above mentioned literature. The maximum pressure in this study is around 3 GPa, hence the yielding and consequently plastic friction are considered to be pressure-independent [47]. If the plastic sliding is ignored in the contact formulation, then, as shown in [48-53], the plastic deformation localizes in a one-element-thick layer beneath the contact surface.

The threshold-type change from cohesion to sliding causes convergence issues in numerical simulations. Hence, cohesive contact condition (when total shear stress is less than critical friction stress) is replaced with a small elastic sliding u_e . In other words, the relative sliding between contact pairs is considered [15, 17, 20] as elastic (reversible) sliding u_e and plastic (irreversible) sliding u_s portions, i.e., $u_c = u_e + u_s$ is the total sliding between contact pairs. When a pair of surfaces is coming into contact their asperities penetrate into one another and hence the elastic sliding represents the elastic deformation of these asperities or the thin contact layer, while plastic sliding corresponds to the relative sliding between two surfaces caused by cutting of asperities or plastic flow in the contact layer. A linear relation [15, 17, 20] $\tau = k_s u_e$ is considered between the elastic sliding and the shear stress where k_s is the contact stiffness defined as $\tau_{crit} = k_s u_{crit}$. In this equation u_{crit} is the maximum permissible elastic sliding between the contact pairs which according to ABAQUS documentation [37] is accepted as 0.5% of the average element size. The complete system of equations for the contact model is as follows:

Additive decomposition of total contact displacement into elastic and plastic sliding

$$u_c = u_e + u_s, \quad (10)$$

Critical shear stress:

$$\tau_{crit} = \min(\mu\sigma_n, \tau_y(q)), \quad (11)$$

Elastic sliding vector:

$$\mathbf{u}_e = \begin{cases} \frac{u_{crit}}{\mu\sigma_n} \boldsymbol{\tau}, & \text{if } \mu\sigma_n < \tau_y(q) \\ \frac{u_{crit}}{\tau_y(q)} \boldsymbol{\tau}, & \text{if } \mu\sigma_n \geq \tau_y(q) \end{cases} \quad (12)$$

Sliding rule:

$$\begin{aligned} \text{if } \tau = |\boldsymbol{\tau}| = (\tau_{rz}^2 + \tau_{\phi z}^2)^{0.5} < \tau_{crit} \quad & |\dot{\mathbf{u}}_s| = 0, \\ \text{if } \tau = |\boldsymbol{\tau}| \geq \tau_{crit} \quad & \dot{\mathbf{u}}_s = \begin{cases} \frac{|\dot{\mathbf{u}}_s|}{\mu\sigma_n} \boldsymbol{\tau}, & \text{if } \mu\sigma_n \leq \tau_y(q) \\ \frac{|\dot{\mathbf{u}}_s|}{\tau_y(q)} \boldsymbol{\tau}, & \text{if } \mu\sigma_n > \tau_y(q) \end{cases} \end{aligned} \quad (13)$$

In the experiments the roughness on the top and inclined surfaces of the anvils is highly increased [34, 41]. Hence, a very large friction coefficient is considered and cohesion or plastic sliding occur only. However, for the lower flat surface of the anvil Coulomb friction model with a wide range of friction coefficients from 0.12 up to 0.5 along with the plastic sliding is considered.

Material Parameters and Numerical Procedure

Anvils, which are made of tool steel [34, 41], are assumed to deform as isotropic elastic solid with Young's modulus E of 210 GPa and Poisson's ratio ν of 0.3. In the previous publications [27-31, 41, 54] anvils were treated as rigid ones. For copper Young's modulus E of 110 GPa and Poisson's ratio ν of 0.33 are used.

In the current paper for copper the following two sets of material parameters will be used. In Ref. [43] $\sigma_{y0} = 330 \text{ MPa}$, $\sigma_y^\infty = 430 \text{ MPa}$, and $m=1$, while in Ref. [38] for annealed copper $\sigma_{y0} = 150 \text{ MPa}$, $\sigma_y^\infty = 457.8 \text{ MPa}$, and $m=4.8$. Saturated yield strength is close for both papers, but initial strength is much higher in Ref. [43] because the material was not annealed and was already subjected to plastic deformation. We will use the following properties in our simulations: (a) data from [38] mentioned above and (b) the same $\sigma_{y0} = 150 \text{ MPa}$ and $\sigma_y^\infty = 457.8 \text{ MPa}$ like in (a) but $m=1.57$ obtained from extrapolating the stress-strain curve in [43] down to the annealed value $\sigma_{y0} = 150 \text{ MPa}$ using Eq. [5].

To solve the friction model the user subroutine FRIC in ABAQUS [37] is utilized. In ABAQUS the equivalent plastic strain is available for the integration points while the friction model is applied for those nodes which meet the contact requirements. For each node in contact the average equivalent plastic strain of those contact elements which share that node is considered as the equivalent plastic strain for calculation of the yield strength in shear. The critical shear stress and the equivalent plastic strain are determined and updated in each iteration of each loading increment.

Due to the intense material flow there is a high distortion of the elements; hence, map-solution technique, which is one of the available remeshing methods in ABAQUS, is used to always keep the shape and aspect ratio of the elements in a proper range. Once excessive distortion occurs in the elements the deformed configuration is remeshed with better shaped and distributed elements. Then distributions of all fields are mapped onto this new mesh from the previous mesh, and the simulation is continued. In this procedure the gradient of fields will be slightly smoothed which can be mitigated by using a proper number of elements, having a proper concentration of the elements in locations with higher gradients of different fields, and

increasing/decreasing the number of the mappings. 4-node generalized bilinear axisymmetric quadrilateral, reduced integration elements are used in the simulations. In the literature [29, 31, 32, 34] 3D models are usually used in simulations and even if axisymmetric models are studied [27, 30] the total number of elements are less than 3000. In the current paper, 8000-13000 elements are used in the model excluding the formed flash which gives the simulations a higher accuracy.

Evolution of Stress and Plastic Strain Fields during HPT

As it will be discussed in the following sections, the friction coefficient of 0.12 on the lower flat surface of the anvils gives the best match between the obtained results and experimental results given in Ref. [41]. Therefore, the friction coefficient is considered to be 0.12 unless otherwise is mentioned. Besides, as in Ref. [41] a material property $m=4.8$ is used unless otherwise is stated.

In this section the distribution and evolution of different fields within the sample for the radius of $r \leq 5$ mm are discussed.

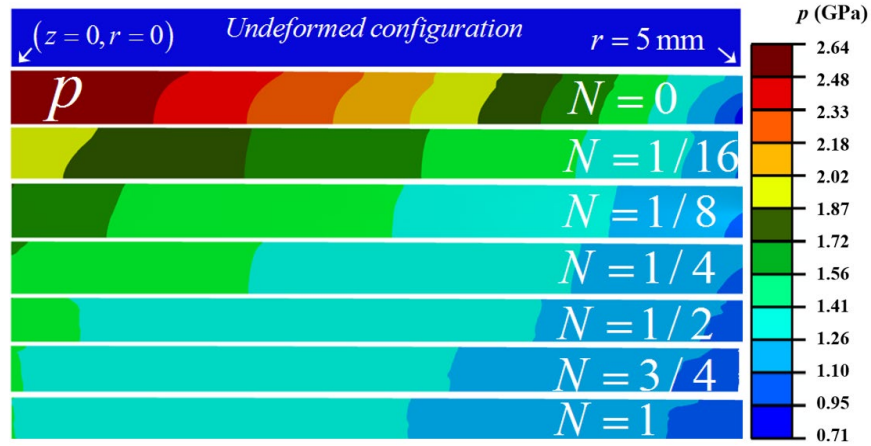


Figure 2. Distributions of pressure p in the sample for different numbers of turns of the anvil, N .

Figures 2 and 3 present the distribution and evolution of pressure in the sample for $r \leq 5$ mm before and during the rotation of the anvil as the sample is compressed under the applied force of $F = 150$ kN. After the compression step, as shown in Figure 2, the distribution of the pressure is close to parabolic along the thickness of the sample and there is a gradient in pressure in the radial direction with the maximum pressure at the symmetry axis. Due to the rotation of the anvil, the circumferential component of shear stress $\tau_{\phi z}$ increases (Figures 6 and 7) as the radial component of the shear stress τ_{rz} decreases. The reduction in the radial component of the shear stress causes the radial material flow which results in the formation of a longer flash. Consequently, new contact surfaces are formed between the anvil and the sample and hence, a part of the applied load on the anvils is imposed to the formed flash. Therefore, pressure reduces in the sample for $r \leq 5$ mm during rotation of the anvil, as also shown in Figure 3. On the other hand, the gradient of pressure in the radial direction reduces. Once the flash is getting longer than the anvil and the contact surface does not increase, the pressure distribution becomes almost stationary. Also, according to Figure 7, the radial component of shear stress almost saturates to a uniform distribution after $\frac{1}{2}$ turns of the anvil, and also the thickness reduction levels off as shown in Figure 4. Hence for larger rotation angles there is an almost uniform pressure distribution within the sample for $r \leq 5$ mm.

Still, further rotation of the anvils results in a small reduction of the pressure for $r \leq 5$ mm due to the formation of the new contact surface between the flash and the anvils along the 5° -inclined surface, which is due to further thickness reduction. Also, plastic deformation on the formed flash increases and, because of the strain hardening, this region bears a larger share of the total applied load causing a slight reduction of the pressure for $r \leq 5$ mm.

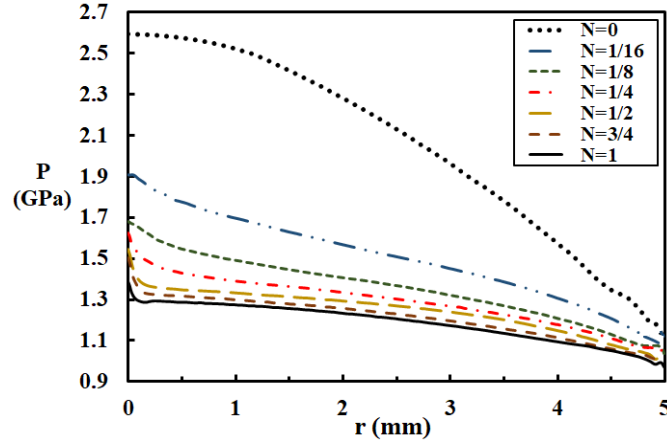


Figure 3. Distributions of pressure p in the sample along the contact surface.

As far as possible phase transformations are concerned the obtained results have two consequences. First, significant reduction in pressure in comparison with unconstrained torsion may lead to the reverse phase transformation to the low-pressure phase. Therefore, the applied load should be carefully chosen in a way that the minimum pressure exceeds the required pressure for the strain-induced reverse phase transformation. Second, a small pressure gradient and pressure close to a homogeneous one, at least at the center of the sample, is desirable for some experiments for easier extraction of material properties from the comparison of simulation and experiment [12, 13, 15, 17]. Also, a large pressure gradient leads to pressure in the high-pressure phase which is much higher than required for transformation, thus damaging anvils [12, 13, 15, 17, 50]. However, if a very large pressure is required the quasi-constraint configuration is not a good choice.

The trend in the thickness reduction shown in Figure 4 is in agreement with experiments in Ref. [38]. Almost reaching the stationary thickness and maximum pressure implies that if a larger pressure or pressure gradient is of interest, the applied compressive force should be increased.

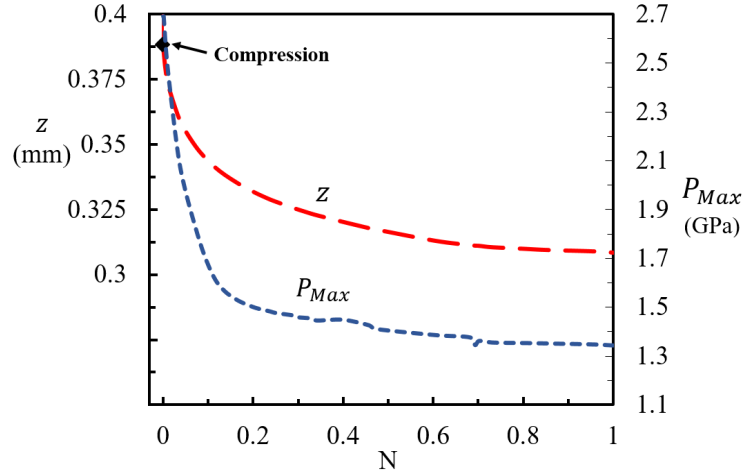


Figure 4. Variation of the maximum pressure and the thickness versus the number of turns of the anvil, N .

Distributions of normal and shear stresses are shown in Figures 5 and 6, respectively.

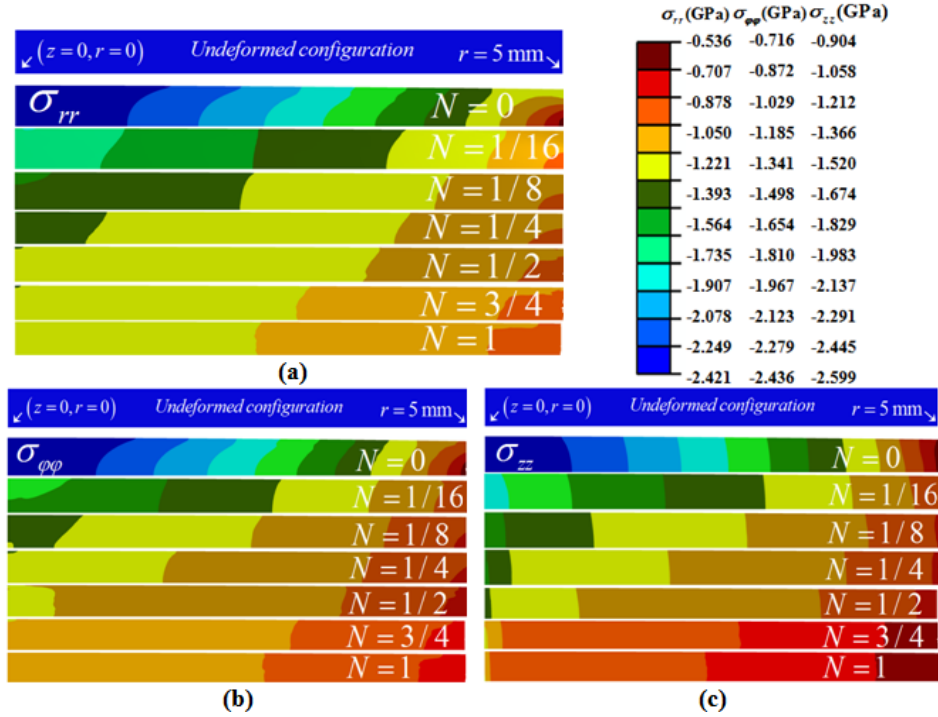


Figure 5. Distributions of normal stresses (a) σ_{rr} , (b) $\sigma_{\phi\phi}$, and (c) σ_{zz} in the sample for different numbers of turns of the anvil, N .

After the compression stage there is an almost uniform distribution of σ_{zz} along the thickness of the sample and a radial gradient of normal stresses with the maximum at the center. The distributions of $\sigma_{\phi\phi}$ and σ_{rr} are almost the same with a parabolic distribution along the thickness. With increasing rotation angle the distributions of all normal components of stress become close to uniform within the entire sample for $r \leq 5 \text{ mm}$. These results are similar to the distribution of pressure in Figure 3.

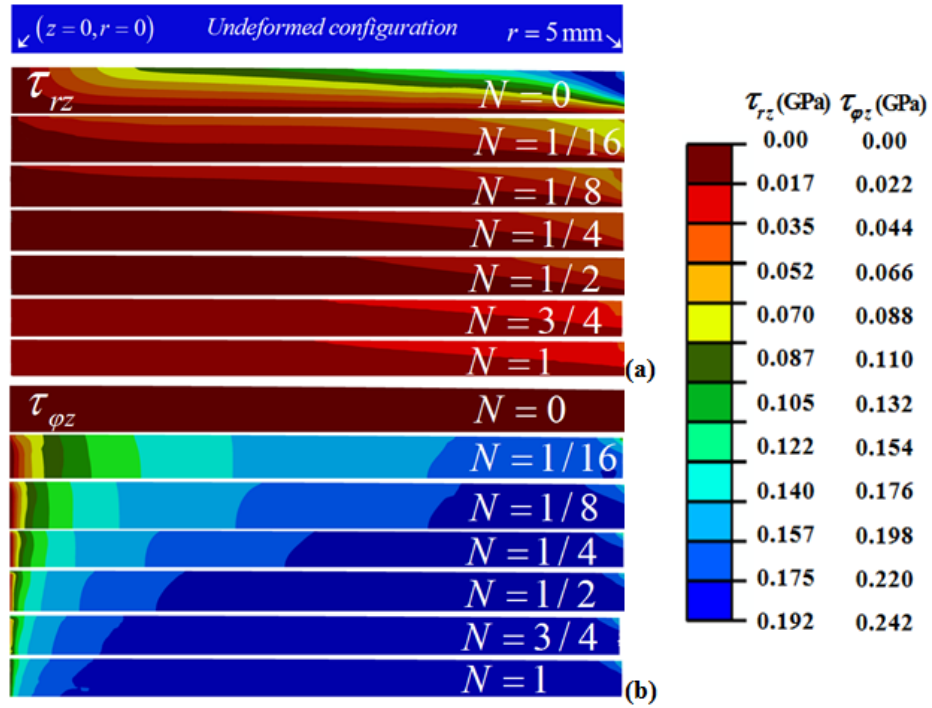


Figure 6. Distribution of shear stresses (a) τ_{rz} and (b) $\tau_{\phi z}$ in the sample for different numbers of turns of the anvil, N .

Due to the symmetry, the radial component of shear stress τ_{rz} is zero at the symmetry axis and the symmetry plane. Just before torsion τ_{rz} increases as expected toward the contact surface and larger radii and reaches its maximum close to the corner of the anvil at the contact

surface (Figure 7). The circumferential component of shear stress $\tau_{\varphi z}$ is zero within the entire sample. Once the torsion is applied and therefore $\tau_{\varphi z}$ increases, τ_{rz} on the contact surface reduces to keep the total shear stress $\tau = (\tau_{rz}^2 + \tau_{\varphi z}^2)^{0.5}$ equal to the yield strength in shear. A reduction in the radial component of shear stress τ_{rz} results in the radial material flow and therefore thickness reduction (Figure 4). A stagnation zone forms at the corner of the anvil (Figure 8) where material moves almost with the anvil, and hence there is a reduction in shear stress at this region. With increasing rotation, τ_{rz} and $\tau_{\varphi z}$ tend to the stationary distribution, because the total shear stress reaches the saturated yield strength in shear. Thus, after a $\frac{1}{2}$ turn rotation of the anvil there are almost no changes in the magnitude and the distribution of the components of the shear stresses in the major part of the sample. This is also consistent with a small change in the distributions of pressure and normal stresses for $r \leq 5$ mm .

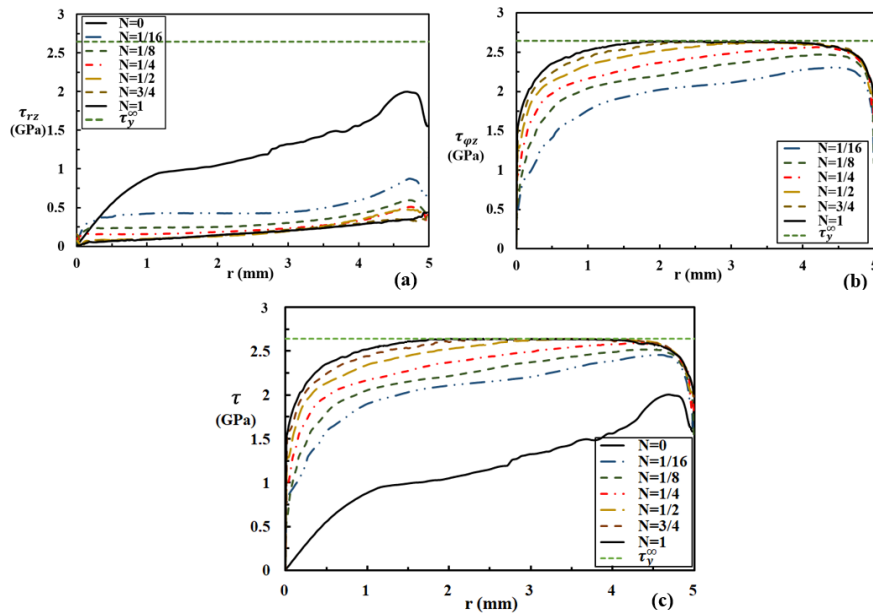


Figure 7. Distribution of shear stresses along the contact surface: (a) τ_{rz} , (b) $\tau_{\varphi z}$, and (c) τ ,

$$\tau = (\tau_{rz}^2 + \tau_{\varphi z}^2)^{0.5} .$$

Distribution of the equivalent plastic strain q in the sample for $m = 4.8$ is shown in Figure 8.

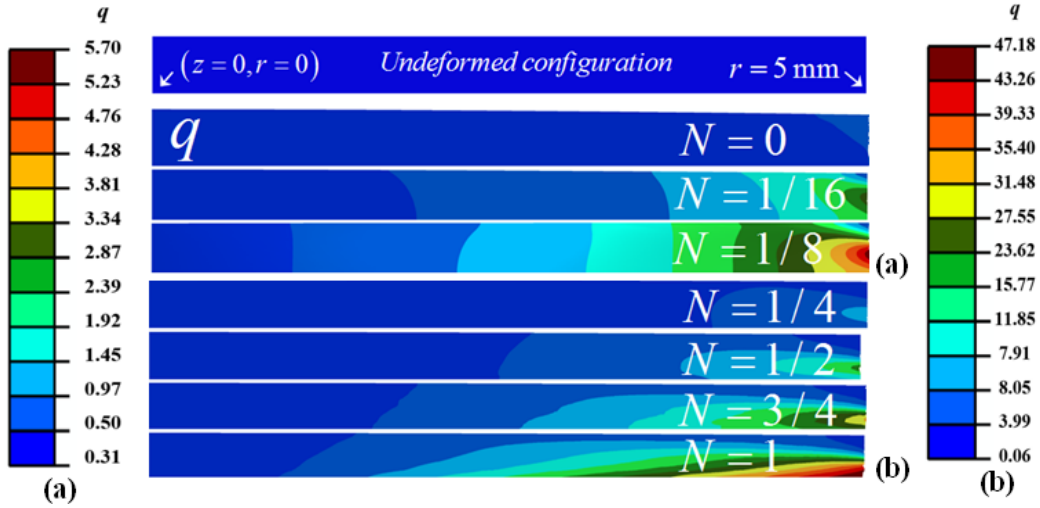


Figure 8. Distributions of equivalent plastic strain q within the sample for different numbers of turns of the anvil, N .

After the compression stage there is a small plastic strain in the sample which is mostly localized close to the inclined surface of the anvils. During torsion the plastic strain increases with the minimum at the symmetry axis (where the only source of the plastic strain is the reduction in the thickness) and the maximum close to the inclined surface of the anvil. A dead metal zone or stagnation region is visible at the corner of the anvil. By increasing rotation angle the gradient of plastic strain within the thickness increases (see Figures 9 and 10). This gradient was also observed in [27, 29, 30, 55]. There is no large gradient in plastic strain within the thickness of the sample for small radii, especially at small rotation angles (Figure 8a), which is observed in experiments in Ref. [56]. As already discussed, after a $\frac{1}{2}$ turn rotation of the anvil further rotation weakly affects the fields of stresses but it increases plastic strain, which results in stronger grain refinement. The distributions of the equivalent plastic strain q along the contact

surface and the symmetry plane during torsion are shown and compared with some analytical distributions in Figure 9.

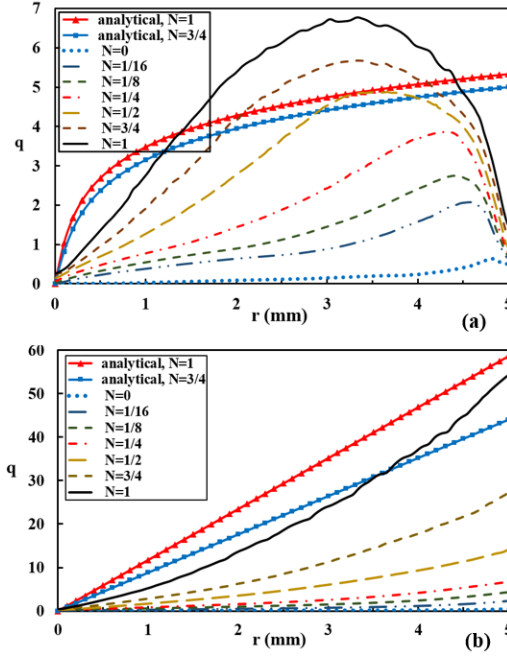


Figure 9. Comparison between the analytical and FEM distributions of the equivalent plastic

strain q along the: (a) contact surface and $q(r) = \frac{2}{\sqrt{3}} \ln \left[\left(1 + \bar{\gamma}^2 / 4 \right)^{1/2} + \bar{\gamma} / 2 \right]$ [57], and (b) symmetry

plane and $q(r) = \bar{\gamma} / \sqrt{3}$, where $\bar{\gamma} = 2\pi r N / h$.

The maximum plastic strain on the contact surface is located close to the inclined surface of the anvils and with increasing rotation the maximum moves toward the center and increases its magnitude. This is in contrast to the simple torsion model in which plastic shear is proportional to the radius. There is a small increase in plastic strain in the sample at the symmetry axis caused by the thickness reduction. The rate of this increase reduces during rotation because the rate of thickness reduction decreases (Figure 4). A large gradient in the plastic strain should cause the gradient in the grain refinement in the central region. However,

close to uniform refinement was observed in the experiments [44] and [29]. Vorhauer and Pippan [44], producing a near-ideal torsional deformation, found that the disappearance of the near-undeformed central region and high grain refinement in it is due to the misalignment of the axes of the anvils or other deviations from idealized HPT processing. There is also a significant gradient in plastic strain close to the top corner of the anvil leading to the formation of a stagnation or dead metal zone, which was also observed in experiments [28, 30, 48]. This significant gradient in the plastic strain may lead to a detachment of the stagnation region from the sample when it is taken out of the experimental setup [28]. The analytical curves will be discussed in following sections.

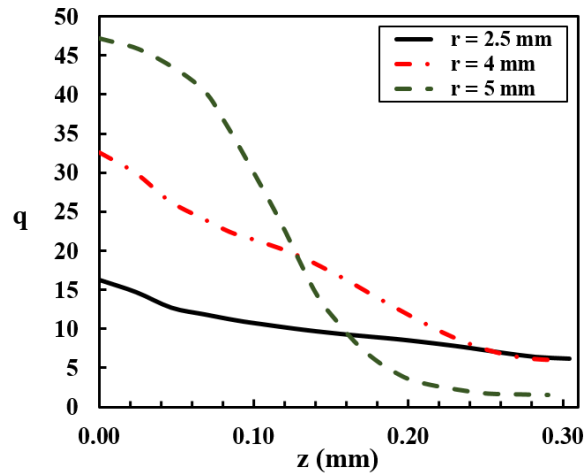


Figure 10. Distributions of the equivalent plastic strain along the thickness of the sample, $N=1$.

In order to better capture the material behavior the distribution of yield strength within the sample during the torsion is shown in Figure 11. After a one turn of the anvil the saturation in the yield is reached in almost the entire sample except for the central region. In experimental measurements the hardness of the material is measured along the radius and thickness. Then, this

hardness is related to the yield strength by $\sigma_y = \frac{HV}{3}(0.1)^{n-2}$ [46], where σ_y is the yield strength in MPa, HV is the Vickers hardness, and n is 2.5 for fully annealed and is 2 for fully strain-hardened material. Figures 12(a) and (b) show the distribution of the hardness along the symmetry plane and along the thickness, respectively based on this relation. As it is seen in Figure 12, after one turn of the anvil there is a uniform and constant hardness distribution along the sample in radial and thickness directions except for the central region which is in agreement with experiments [33, 39, 41, 44, 45, 48, 58, 59]. Along the symmetry axis the plastic strain has its maximum at the center of the sample and its minimum on the contact surface (Figure 10) which results in the similar distribution of hardness in Figure 12b. The FEM result for distribution of the hardness along the symmetry plane from Ref. [38] is also shown in Figure 12a.

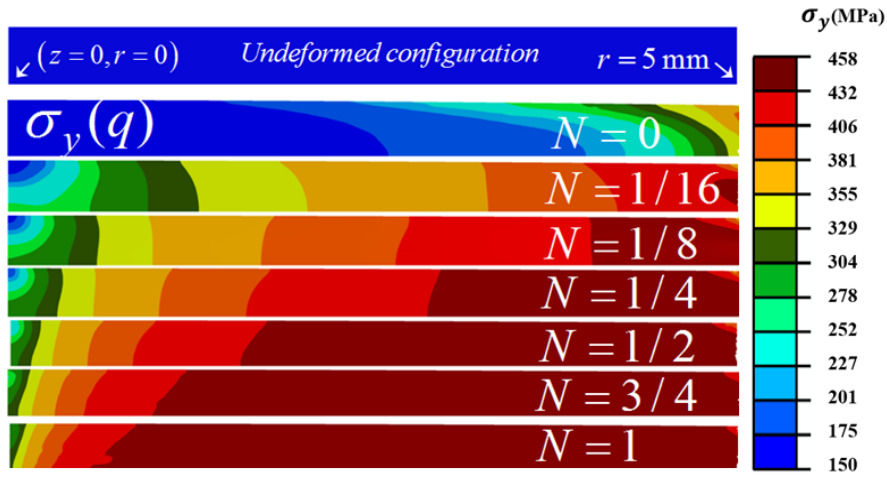


Figure 11. Distributions of the yield strength σ_y within the sample for different numbers of turns of the anvil, N .

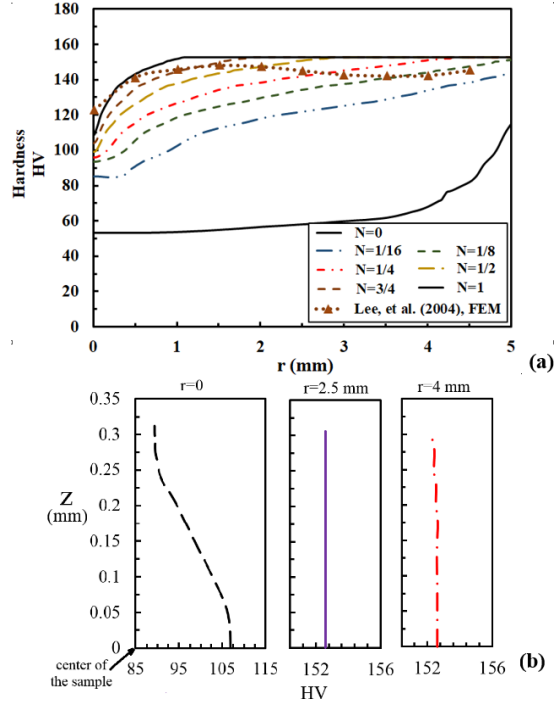


Figure 12. Distributions of hardness HV in the sample along the: (a) symmetry plane during torsion, including FEM from Ref. [38] and (b) thickness for three different radii after one turn rotation of the anvil.

Figure 13 presents the circumferential relative displacement between the sample and the anvil along the contact surface in terms of the number of rotations, N . Minimum slip between the sample and the anvil, as expected, occurs at the stagnation region at the top corner of the anvil and at the symmetry axis. According to Figures 8 and 9 the minimum plastic stain is located in the central region of the sample close to the symmetry axis. That is why the yield strength in shear in the friction model is smaller in the central region of the sample promoting plastic sliding. The sliding decreases along the radius from the point where it is maximal to both zeros. The magnitude of the sliding increases as the rotation angle increases. Maximum sliding for $N=1$ slightly exceeds 20%. For a larger rotation the displacement discontinuity within the material near the stagnation zone is expected, which eliminates zero sliding near the corner of the anvil

and strongly increases sliding along the entire surface. For unconstraint HPT the analytical expression for relative sliding angle is [7, 8, 10]

$$\omega - \omega_a = -\frac{0.204x}{1 + 0.204x} \omega_a, \quad x := R/h_0, \quad (14)$$

where ω and ω_a are the angular velocities of the material and anvil. For $R=5$ mm and $h_0=0.8$ mm, $\omega - \omega_a = -0.56\omega_a$, i.e., the rotation of a material is almost two times smaller than the rotation of an anvil. Note that Eq. [14] is in good correspondence with FEM simulations in [21].

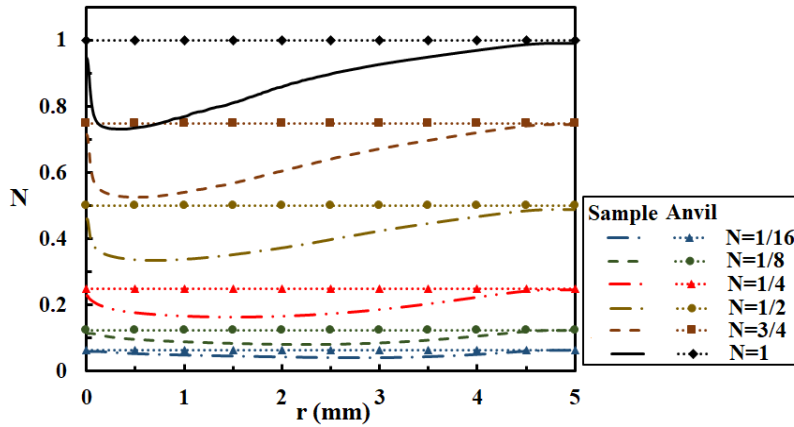


Figure 13. Circumferential relative displacement between the sample and the anvil along the contact surface in terms of the numbers of turns, N .

In experiments the torque-rotation angle response of the sample is usually measured and then, based on [60] $\sigma_i = \sqrt{3}T(3 + M + N)/2\pi r^3$, where σ_i is the effective (von Misses) stress, T is torque, $M = (\partial \ln T / \partial \ln \dot{\theta})$, $N = (\partial \ln T / \partial \ln \theta)$, r is radius, and θ is rotation angle, and Eq. [9], the stress-strain curve of the material is derived. It is also possible, as mentioned, to measure the hardness and relate it to the yield strength $\sigma_y = HV/3$ [46]. The contact layer is

usually polished away before hardness measurements in order to exclude the region with highly localized plastic flow and strain hardening. Eq. [9] gives a linearly-increasing accumulated strain which is not the case in the quasi-constraint case along the contact surface but is more accurate and closer to the symmetry plane (Figures 9 and 14) after a certain rotation angle. The error in the calculated equivalent plastic strain along the contact surface strongly increases with radius. The effective stress is usually measured on the outer edges of the sample where inaccuracy in the calculated q is large. Also, these measurements give significantly different results if conversion of the torque-rotation angle to the effective stress-strain is done for different radii r . Therefore, different material properties may be reported for the same material. Even the same authors for the same material report very different material properties. For example, for pure copper the saturation strain $m=4.8$ in [38], while it is 15 in [39] and is 20 in [40]. As mentioned, measured hardness over a point can be related to the effective stress. Based on our simulations both hardness and q should be measured and evaluated at the symmetry plane (Figures 9 and 14). However, even in such a case, the position of the measuring point highly affects the calculated plastic strain and hence derived the material properties.

As already mentioned the analytical equivalent plastic strain in pressure-torsion studies is usually determined by Eq. [9] [22, 23, 41, 45]. This equation is based on the assumption that rotation angle of the sample is equal to that of the anvils, and there is no radial flow and thickness reduction. Also, the distribution of the equivalent plastic strain is not a linearly-increasing function of radius (Figure 9) and is not uniform along the thickness of the sample. That is why the magnitude of q obtained with FEM is lower than that based on Eq. [9], essentially at the symmetry plane and drastically at the contact surface (see Figure 14). Including the real rotation angle of the sample in Eq. [9] makes the correspondence with the FEM results

slightly better. Two alternative definitions of the equivalent plastic strain, $q(r) = \ln(\bar{\gamma})$ [61-63] and $q(r) = \frac{2}{\sqrt{3}} \ln \left[\left(1 + \bar{\gamma}^2 / 4 \right)^{1/2} + \bar{\gamma} / 2 \right]$ [57] with $\bar{\gamma} = 2\pi r N / h$, show a better agreement at the symmetry plane (Figures 9 and 14). Note that these definitions do not correspond to Eq. [6] and to be legible must be formulated for an arbitrary loading in terms of plastic deformation rate \mathbf{d}_p . As shown in Figure 9, even for alternative relations for the equivalent plastic strain, the accuracy of the results depends on the rotation angle. An error of the calculated plastic strain decreases with an increase in rotation angle, i.e., the derived material properties for small rotation angles are not accurate.

Thus, analytical predictions of the distribution of the equivalent plastic strain are quite poor, mostly due to heterogeneity of plastic strain along the thickness. This explains the significant overestimate and the scatter in the value of saturation strain, m , based on saturation of hardness: equivalent strain q taken from Eq. [9] is drastically larger than that obtained by FEM at the contact surface, and their ratio strongly varies along the radius. Since the sample is often polished before measurement [29, 32, 39, 40, 64, 65], because of the large gradient of q along the thickness, results strongly depend on the width of the removed material. The best approach is to polish half of the sample and to use FEM for interpretation of the experiments. If accurate material properties are of interest, the homogeneous compression test is a reliable option.

Figure 15 shows the profile of the deformed sample after one turn of the anvil. Because maximum pressure does not exceed 3 GPa (Figure 4), maximum deformation of the anvil is less than 0.5% of the sample's initial thickness. In other words, deformation of the anvil can be neglected.

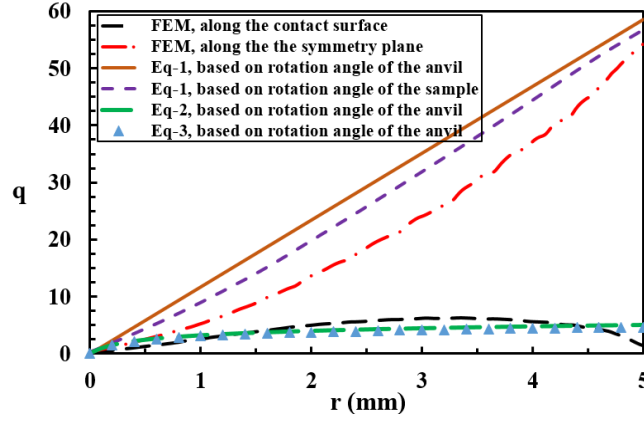


Figure 14. Comparison between distributions of the equivalent plastic strain q determined by

FEM and the analytical curves for $N=1$. Eq.1: $q(r) = \gamma/\sqrt{3}$, Eq.2: $q(r) = \frac{2}{\sqrt{3}} \ln \left[\left(1 + \bar{\gamma}^2 / 4 \right)^{1/2} + \bar{\gamma} / 2 \right]$,

and Eq.3: $q(r) = \ln(\bar{\gamma})$, where $\bar{\gamma} = 2\pi r N / h$.

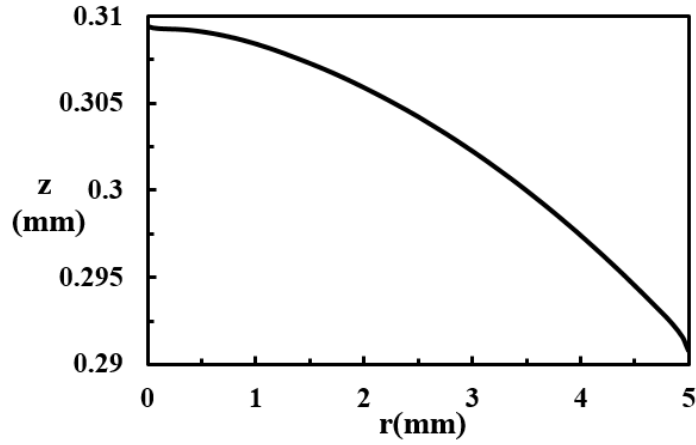


Figure 15. Profile of the sample's top contact surface, $N=1$.

Effect of the Different Contact Conditions

In this section the torque-rotation angle response of the sample is studied in detail in order to determine the proper contact conditions for FEM simulations which give the best match

with experimental results in [41]. Then the effect of different friction conditions on the behavior of the material is studied.

Edalati et al. [41] performed multiple experiments and simulations on the torque-rotation angle response of the sample, with one of the sets shown in Figure 16. Before doing the experiments they increased the roughness on the top and inclined surfaces of the anvils based on which they have considered the cohesive contact condition over the entire contact surface. Figure 16 shows the comparison between their experimental and FEM [41] results and our FEM results for five different cases. The cohesive contact along the entire contact surface (similar to the contact condition in Ref. [41]) and with plastic friction/sliding demonstrate a large difference compared to the FEM and experimental results in Ref. [41]. Note that the estimate of the upper bound for torque $M = \int 2\pi\tau_y^{\infty} r^2 dr$, assuming that $\tau_{\phi z} = \tau_y^{\infty}$ (which is not so far from reality based on Figure 7) and flash being in contact with the entire horizontal ring of width w , gives $M=174.3$ Nm, similar to our FEM results for the above two cases but much larger than 90 Nm in FEM simulations and around 110 Nm in experimental curve given in Ref. [41]. Such an overestimate in comparison with experiments indicates that plastic sliding alone is not an adequate friction model. We supplemented it with the Coulomb friction along a horizontal ring of width w (Figure 1) with the friction coefficients μ of 0.12, 0.2 and 0.5. It's worth mentioning that the observed steps in the curve related to the cohesive contact in our FEM simulations in Figure 16 are due to the inaccuracies associated with the remeshing and map-solution technique. When the plastic sliding is allowed the number of the required mappings are much smaller (because of smaller localization of shear distortion in the contact elements), which results in smoother curves.

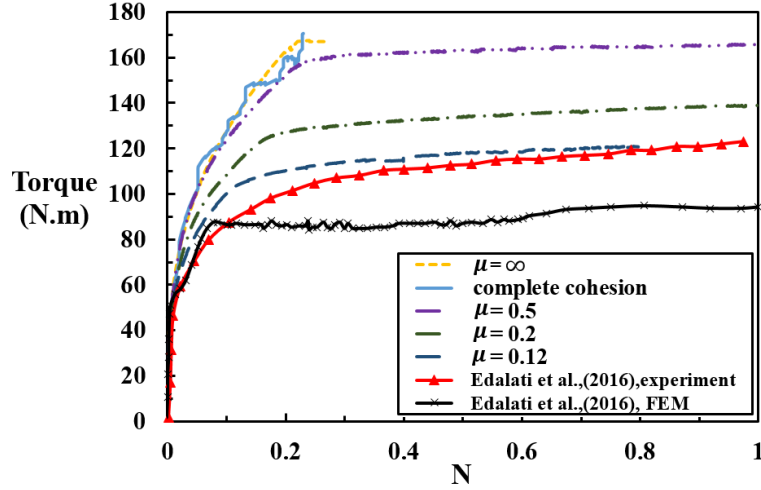


Figure 16. Plots torque vs. number of turns of the anvil for different contact conditions in our FEM results and in experiments and FEM simulation in [41].

With the Coulomb friction, results for $\mu=0.2$ are slightly lower than for plastic friction ($\mu=\infty$). With reduction in μ torque reduces and gets close to the experimental curve at $\mu=0.12$ (which is used in all the simulations in Section III). Therefore, although the length of the lower flat surface of the anvils is just 30% of the initial sample radius and is usually ignored in experimental considerations, it contributes significantly to the force and especially torque due to large radius and area. In particular, the torque–rotation angle response is usually translated to stress-strain response of the material and is commonly used to determine the yield strength in shear of the material. Figure 16 shows that it cannot be used for this purpose unless the exact friction condition along the entire contact surface is known. This fact is one of the reasons for the large discrepancy of the reported torque–rotation angle responses and therefore material properties in the literature. A solution to this problem can be increasing the roughness over the entire contact surfaces in a way that it leads to the plastic friction along the entire contact surface. Then at least τ_y^∞ can be determined after the torque has reached its maximum value.

Figures 17 and 18 show that the accumulated plastic strain within the sample for $r \leq 5$ mm after a 1/4 turn of the anvil slightly reduces and flash size essentially reduces with increasing μ .

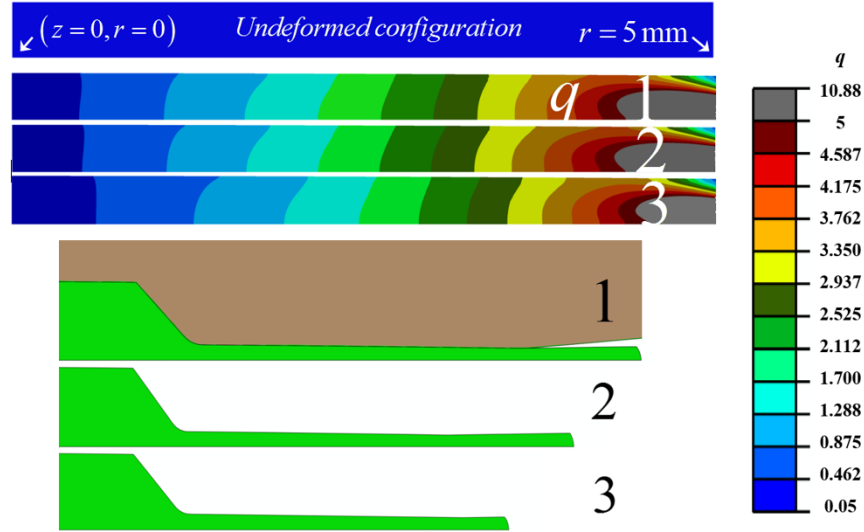


Figure 17. (a) Distributions of equivalent plastic strain q in the sample and (b) size of the formed flash for $N=1/4$. 1: $\mu=0.12$; 2: $\mu=0.2$; 3: $\mu=0.5$.

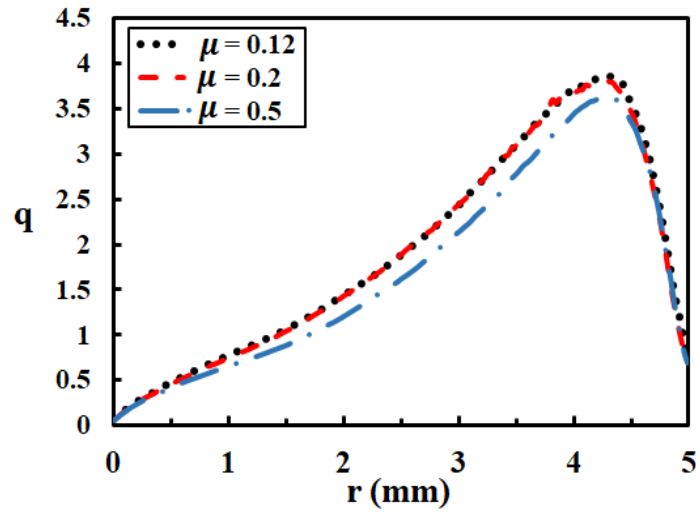


Figure 18. Distributions of equivalent plastic strain q in the sample along the contact surface for different friction coefficients for $N=1/4$.

Effect of the Material Properties

Here we compare the results for two different saturation strains, $m=1.57$ [43] and $m=4.8$ [38] with all other parameters being the same. The torque-rotation angle responses for these two cases are shown in Figure 19, and their difference is negligible. Therefore, the torque-rotation angle response of the material is not sensitive to m and cannot be used to determine m . The reason is that the main contribution for the torque comes from large radii, where plastic strains are large and reach m for small rotations. This is another explanation for the large scatter of values for m in the literature.

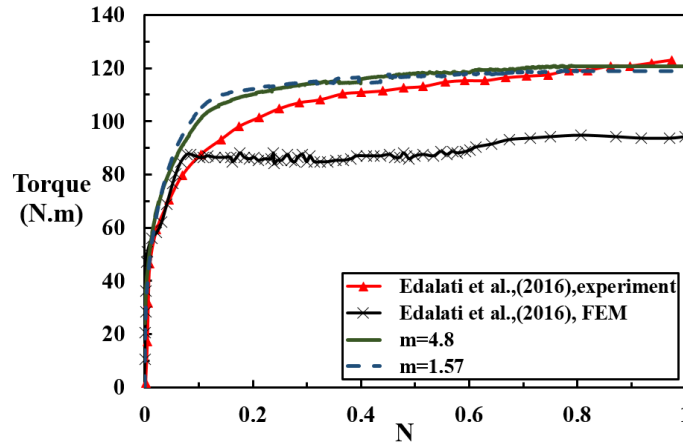


Figure 19. Variation of the torque vs. number of turns of the anvils for $m=4.8$ and $m=1.57$, and their comparison to the experimental and FEM results in Ref. [41].

The distribution of equivalent plastic strain over the contact surface and the distribution of hardness along the symmetry plane are compared for these two cases in Figures 20 and 21, respectively. Smaller yield stress for $1.57 < q < 4.8$ for $m=4.8$ causes smaller friction stress for plastic friction, larger contact sliding and larger plastic deformation for the same rotation angle of the anvil.

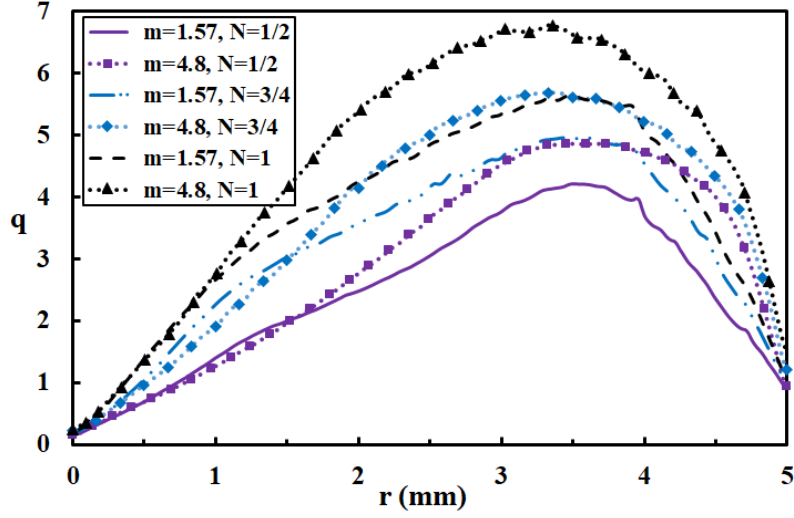


Figure 20. Comparison of distributions of equivalent plastic strain along the contact surface for $m=4.8$ and $m=1.57$.

On the other hand, a smaller $m=1.57$ can be reached in a larger portion of the sample than for larger $m=4.8$. Therefore, a broader sample region with the uniform distribution of the hardness is obtained for $m=1.57$ as seen in Figure 21.

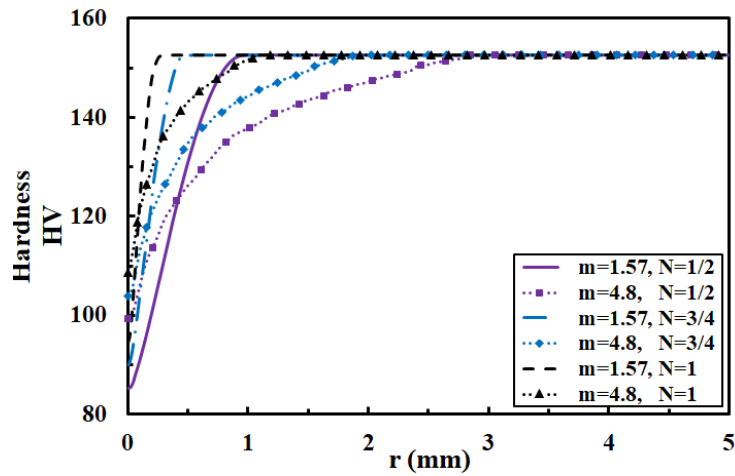


Figure 21. Comparison of distributions of hardness HV along the symmetry plane $m=4.8$ and $m=1.57$.

Concluding Remarks

In this paper the behavior of the sample under HPT in a quasi-constraint configuration is studied using FEM method. The effect of different contact conditions and material properties on the distribution of different fields and torque-rotation angle response of the sample is shown.

It is shown that considering complete cohesion along the entire contact surfaces ends up in an overestimation in the torque-rotation angle response of the sample in comparison to the available experimental data. Therefore, the friction model is advanced to include both Coulomb and plastic sliding. Results show that the torque-rotation angle behavior of the sample is highly dependent on the friction condition in the flash region, which was ignored in the analyses of experiments due to its small size compared to the initial diameter of the sample. Simulations show that variation in the friction coefficient in the flash region from 0.12 up to 0.5 results in 45% increase in the calculated torque. Also, the torque-rotation angle curve is practically independent of the saturation strain m . Both results show that the torque-rotation angle cannot be used for determining the stress-strain curve of materials.

While initial yield strength of the annealed material and the saturation (maximum) yield strength of the ultimately hardened material can be easily determined experimentally through a standard stress-strain curve for homogeneous stress-strain fields at moderate strains and ultimate hardness of material, respectively, the main fundamental problem is in finding saturation strain m . It strongly varies in HPT literature, from 4.8 [38] to 20 [40] for copper. Our simulations showed that determination of m in HPT experiments based on determination of plastic strain required for saturation of the hardness contained large errors (a) due to large heterogeneity of the plastic strain both along the radius and thickness, which is not accurately described by existing simplified analytical models, and (b) due to some contact sliding. Utilizing the symmetry plane for determination of m is much more reliable than the contact surface. Even in such a case the

accuracy of the analytically-determined equivalent plastic strain depends on the measuring radius and the rotation angle of the anvils. At the same time the methods for determining the stress-strain curves for the homogeneous compression test of a special sample is strict and gives $m=1$ for preliminary-treated material [43] and an extrapolated value of $m=1.57$ for annealed copper. This value corresponds to the range estimated in [35, 36, 43] for most of materials.

As the sample deforms, the contact surface between the sample and the anvils increases, then the contact area between formed flash and the anvils does not change anymore. Consequently, the maximum pressure gradient and pressure in the central region of a sample initially reduces during rotation and after a certain rotation angle of the anvils, the gradient in pressure distribution almost vanishes and maximum pressure practically does not change. All stress fields reach an almost stationary and uniform distribution along the entire sample. Increasing rotation of the anvil increases plastic strain which results in smaller grain sizes.

From the point of view of studying the phase transformations, quasi-constraint torsion has some drawbacks and advantages. Advantages are in the quasi-homogeneous stress distribution, which is desirable for extracting kinetic equations for phase transformations from comparing simulation and experiment [12, 13, 15, 17]. Also, for a small stress gradient, anvils are not overloaded above pressure, which is required for phase transformation after completing transformation, like in [12, 13, 15, 17, 50]. However, a non-monotonous change in pressure with plastic straining significantly complicates the extraction of kinetic information. In particular, the reduction of the pressure due to the torsion may cause the reverse phase transformation. Also, a quasi-homogeneous pressure distribution prevents achieving high pressure, in contrast to HPT in the unconstraint configuration. Phase transformations under HPT in quasi-constraint configuration will be studied in a future paper.

Acknowledgements

The support of NSF (DMR-1434613), ARO (W911NF-17-1-0225), and Iowa State University (Schafer 2050 Challenge Professorship and Vance Coffman Faculty Chair Professorship) is gratefully acknowledged.

References

- [1] R. Pippan, S. Scheriau, A. Taylor, M. Hafok, A. Hohenwarter, A. Bachmaier, Saturation of fragmentation during severe plastic deformation, *Annu. Rev. Mater. Res.* 40 (2010) 319-343.
- [2] A.P. Zhilyaev, T.G. Langdon, Using high-pressure torsion for metal processing: fundamentals and applications, *Prog. Mater. Sci.* 53 (2008) 893-979.
- [3] R.Z. Valiev, Y. Estrin, Z. Horita, T.G. Langdon, M.J. Zechetbauer, Y.T. Zhu, Producing bulk ultrafine-grained materials by severe plastic deformation, *Nanostruct. Mater.* 58 (2006) 33-39.
- [4] P.V. Liddicoat, X.Z. Liao, Y. Zhao, Y. Zhu, M.Y. Murashkin, E.J. Lavernia, R.Z. Valiev, S.P. Ringer, Nanostructural hierarchy increases the strength of aluminium alloys, *Nat. Commun.* 1:63 (2010).
- [5] T.F. Dalla, R. Lapovok, J. Sandlin, P.F. Thomson, C.H.J. Davies, E.V. Pereloma, Microstructures and properties of copper processed by equal channel angular extrusion for 1–16 passes, *Acta Mater.* 52 (2004) 4819-4832.
- [6] V.D. Blank, E.I. Estrin, *Phase transition in solids under high pressure*, CRC Press, New York, 2017.
- [7] V.I. Levitas, High-pressure mechanochemistry: conceptual multiscale theory and interpretation of experiments, *Phys. Rev. B* 70 (2004) 184118.
- [8] V.I. Levitas, *Continuum Mechanical Fundamentals of Mechanochemistry* Section in: *High Pressure Surface Science and Engineering*, Institute of Physics, Bristol and Philadelphia, 2003.
- [9] K. Edalati, Z. Horita, A review on high-pressure torsion (hpt) from 1935 to 1988, *Mater. Sci. Eng., A* 652 (2016) 325-352.
- [10] V.I. Levitas, A microscale model for strain-induced phase transformations and chemical reactions under high pressure, *Europhys. Lett.* 66 (2004) 687-693.

- [11] V.I. Levitas, O.M. Zarechnyy, Kinetics of strain-induced structural changes under high pressure, *J. Phys. Chem. B* 110 (2006) 16035-16046.
- [12] V.I. Levitas, J. Hashemi, Y. Ma, Strain-induced disorder and phase transformation in hexagonal boron nitride under quasi-homogeneous pressure: in situ x-ray study in a rotational diamond anvil cell," *Europhys. Lett.* 68 (2004) 550-556.
- [13] V.I. Levitas, Y. Ma, J. Hashemi, M. Holtz, N. Guven, Strain-induced disorder, phase transformations, and transformation-induced plasticity in hexagonal boron nitride under compression and shear in a rotational diamond anvil cell: in situ x-ray diffraction study and modeling, *J. Chem. Phys.* 125 (2006) 1-14.
- [14] V.I. Levitas, Y. Ma, E. Selvi, J. Wu, J.A. Patten, High-density amorphous phase of silicon carbide obtained under large plastic shear and high pressure, *Phys. Rev. B* 85 (2012) 054114.
- [15] B. Feng, V.I. Levitas, Effects of gasket on coupled plastic flow and strain-induced phase transformations under high pressure and large torsion in a rotational diamond anvil cell, *J. Appl. Phys.* 119 (2016) 015902.
- [16] B. Feng, O.M. Zarechnyy, V.I. Levitas, Strain-induced phase transformations under compression, unloading, and reloading in a diamond anvil cell, *J. Appl. Phys.* 113 (2013) 173514.
- [17] B. Feng, V.I. Levitas, Y. Ma, Strain-induced phase transformation under compression in a diamond anvil cell: simulations of a sample and gasket, *J. Appl. Phys.* 115 (2014) 163509.
- [18] B. Feng, V.I. Levitas, O.M. Zarechnyy, Strain-induced phase transformations under high pressure and large shear in a rotational diamond anvil cell: Simulation of loading, unloading, and reloading, *Comput. Mater. Sci.* 84 (2014) 404-416.
- [19] B. Feng, V.I. Levitas, R. Hemley, Large elastoplasticity under static megabar pressures: Formulation and application to compression of samples in diamond anvil cells, *Int. J. Plast.* 84 (2016) 33-57.
- [20] B. Feng, V.I. Levitas, Coupled phase transformations and plastic flows under torsion at high pressure in rotational diamond anvil cell: Effect of contact sliding, *J. Appl. Phys.* 114 (2013) 213514.
- [21] V.I. Levitas, O.M. Zarechnyy, Numerical study of stress and plastic strain evolution under compression and shear of a sample in a rotational anvil cell, *High Press. Res.* 30 (2010) 653-669.
- [22] K. Edalati, R. Miresmaeili, Z. Horita, H. Kanayama, R. Pippan, Significance of temperature increase in processing by high-pressure torsion, *Mater. Sci. Eng. A* 528 (2011) 7301-7305.

- [23] R.B. Figueiredo, P.H.R. Pereira, M. Aguila, P.R. Cetlin, T.G. Langdon, Using finite element modeling to examine the temperature distribution in quasi-constrained high-pressure torsion, *Acta Mater.* 60 (2012) 3190-3198.
- [24] P.H.R. Pereira, R.B. Figueiredo, P.R. Cetlin, T.G. Langdon, Using finite element modelling to examine the flow process and temperature evolution in HPT under different constraining conditions, *Mater. Sci. Eng.* 63 (2014) 012041.
- [25] Y. Song, W. Wang, D. Gao, E.Y. Yoon, D.J. Lee, C. Lee, H.S. Kim, Hardness and microstructure of interstitial free steels in the early stage of high-pressure torsion, *J. Mater. Sci.* 48 (2013) 4698-4704.
- [26] W. Wang, Y. Song, D. Gao, E.Y. Yoon, D.J. Lee, C. Lee, H.S. Kim, Analysis of stress states in compression stage of high pressure torsion using slab analysis method and finite element method, *Met. Mater. Int.* 19 (2013) 1021-1027.
- [27] R.B. Figueiredo, M.T.P. Aguilar, P.R. Cetlin, T.G. Langdon, Analysis of plastic flow during high-pressure torsion, *J. Mater. Sci.* 47 (2012) 7807-7814.
- [28] D.J. Lee, H.S. Kim, Finite element analysis for the geometry effect on strain inhomogeneity during high-pressure torsion, *J. Mater. Sci.* 49 (2014) 6620-6628.
- [29] R.B. Figueiredo, T.G. Langdon, Heterogeneous flow during high-pressure torsion, *Mater. Res.* 16 (2013) 571-576.
- [30] Y. Song, M. Chen, B. Gao, J. Guo, L. Xu, Z. Wang, H.S. Kim, Effects of friction and anvil design on plastic deformation during the compression stage of high-pressure torsion, *Korean J. Met. Mater.* 54 (2016) 831-837.
- [31] Y. Song, W. Wang, D. Gao, E.Y. Yoon, D.J. Lee, H.S. Kim, Finite element analysis of the effect of friction in high pressure torsion, *Met. Mater. Int.* 20 (2014) 445-450.
- [32] D.J. Lee, E.Y. Yoon, L.J. Park, H.S. Kim, The dead metal zone in high-pressure torsion, *Scripta Mater.* 67 (2012) 384-387.
- [33] Y. Song, W. Wang, D.J. Lee, H.J. Jeong, S. Lee, H.S. Kim, Thickness inhomogeneity in hardness and microstructure of copper after the compressive stage in high-pressure torsion, *Met. Mater. Int.* 21 (2015) 7-13.
- [34] D.J. Lee, E.Y. Yoon, S.H. Lee, H.S. Kim, Finite element analysis for compression behavior of high pressure torsion processing, *Rev. Adv. Mater. Sci.* 31 (2012) 25-30.
- [35] V.I. Levitas, Large elastoplastic deformations of materials at high pressure, Kiev: Naukova Dumka, 1987.

- [36] [V.I. Levitas, Large deformation of materials with complex rheological properties at normal and high pressure, Nova Science Publishers, New York, 1996.
- [37] Abaqus V6.11. User Subroutines. Providence RI, USA: Abaqus INC (2011).
- [38] D.J. Lee, E.Y. Yoon, D.H. Ahn, B.H. Park, H.W. Park, L.J. Park, Y. Estrin, H.S. Kim, Dislocation density-based finite element analysis of large strain deformation behavior of copper under high-pressure torsion, *Acta Mater.* 76 (2014) 281-293.
- [39] K. Edalati, T. Fujioka, Z. Horita, Microstructure and mechanical properties of pure Cu processed by high-pressure torsion, *Mater. Sci. Eng. A* 497 (2008) 168-173.
- [40] K. Edalati, Y. Ito, K. Suehiro, Z. Horita, Softening of high purity aluminum and copper processed by high pressure torsion, *Int. J. Mater. Res.* 100 (2009) 1668-1673.
- [41] K. Edalati, D.J. Lee, T. Nagaoka, M. Arita, H.S. Kim, Z. Horita, R. Pippan, Real hydrostatic pressure in high-pressure torsion measured by bismuth phase transformations and fem simulations, *Mater. Trans.* 57 (2016) 533-538.
- [42] N.V. Novikov, S.B. Polotnyak, L.K. Shvedov, V.I. Levitas, Regularities of phase transformations and plastic straining of materials in compression and shear on diamond anvils: experiments and theory, *J. Superhard Mater.* 21 (1999) 36-48.
- [43] V.I. Levitas, I.E. Stashkevich, A.B. Nemirovskii, Stress-strain diagrams of metals under large uniform compressive strains, *Strength of Materials* 26 (1994) 676-680.
- [44] A. Vorhauer, R. Pippan, On the homogeneity of deformation by high pressure torsion, *Scripta Mater.* 51(2004) 921-925.
- [45] F. Wetscher, A. Vorhauer, R. Pippan, Strain hardening during high pressure torsion deformation, *Mater. Sci. Eng. A* 410-411 (2005) 213-216.
- [46] G.E. Dieter, Mechanical metallurgy, New York, McGraw-Hill, 1976.
- [47] T. Wanheim, Friction at high normal pressures, *Wear*, 25 (1973) 225-244.
- [48] A. Hohenwartera, A. Bachmaier, B. Gludovatz, S. Scheriau, R. Pippan, Technical parameters affecting grain refinement by high pressure torsion, *Mater. Res.* 100 (2009) 1653-1661.
- [49] R.B. Figueiredo, M.T.P. Aguilar, P.R. Cetlin, T.G. Langdon, Deformation heterogeneity on the cross-sectional planes of a magnesium alloy processed by high-pressure torsion, *Metall. Mater. Trans. A* 42 (2011) 3013-3021.

- [50] V.I. Levitas, O.M. Zarechnyy, Modeling and simulation of strain-induced phase transformations under compression in a diamond anvil cell, *Phys. Rev. B* 82 (2010) 174123.
- [51] B. Feng, V.I. Levitas, O.M. Zarechnyy, Plastic flows and phase transformations in materials Plastic flows and phase transformations in materials contact sliding, *J. Appl. Phys.* 14 (2013) 043506.
- [52] V.I. Levitas, O.M. Zarechnyy, Modeling and simulation of strain-induced phase transformations under compression and torsion in a rotational diamond anvil cell, *Phys. Rev. B* 82 (2010) 174124.
- [53] V.I. Levitas, O.M. Zarechnyy, Modeling and simulation of mechanochemical processes in a rotational diamond anvil cell, *Europhys. Lett.* 88 (2009) 16004.
- [54] R.B. Figueiredo, P.R. Cetlin, T.G. Langdon, Using finite element modeling to examine the flow processes in quasi-constrained high-pressure torsion, *Mater. Sci. Eng. A* 528 (2011) 8198-8204.
- [55] H.J. Jeong, E.Y. Yoon, D.J. Lee, N.J. Kim, S. Lee, H.S. Kim, Nanoindentation analysis for local properties of ultrafine grained copper processed by high pressure torsion, *J. Mater. Sci.* 47 (2012) 7828-7834.
- [56] P. Wei, C. Lu, A.K. Tieu, G. Deng, A study of plastic deformation behavior during high pressure torsion process by crystal plasticity finite element simulation, *Mater. Sci. Eng.* 63 (2014) 012045.
- [57] N.H. Polakowski, E.J. Ripling, *Strength and structure of engineering materials*, Englewood Cliffs, Prentice-Hall, 1966.
- [58] H. Hebesberger, H.P. Stuwe, A. Vorhauer, F. Wetscher, R. Pippan, Structure of Cu deformed by high pressure torsion, *Acta Mater.* 53 (2005) 393-402.
- [59] Y. Song, E.Y. Yoon, D.J. Lee, J.H. Lee, H.S. Kim, Mechanical properties of copper after compression stage of high-pressure torsion, *Mater. Sci. Eng. A* 528 (2011) 4840-4844.
- [60] J.J. Jonas, F. Montheillet, L.S. Toth, C. Ghosh, Effects of varying twist and twist rate sensitivities on the interpretation of torsion testing data, *Mater. Sci. Eng. A* 591 (2014) 9-17.
- [61] M.V. Degtyarev, T.I. Chashchukhina, L.M. Voronova, A.M. Patselov, V.P. Pilyugin, Influence of the relaxation processes on the structure formation in pure metals and alloys under high-pressure torsion, *Acta Mater.* 55 (2007) 6039.
- [62] N.A. Smirnova, V.I. Levit, V.P. Pilyugin, Evolution of structure of fcc single crystals during strong plastic deformation, *Phys. Met. Metallogr.* 61 (1986) 127-134.

- [63] A.P. Zhilyaev, G.V. Nurislamova, B.K. Kim, M.D. Baro, J.A. Szpunar, T.G. Langdon, Experimental parameters influencing grain refinement and microstructural evolution during high-pressure torsion, *Acta Mater.* 51 (2003) 753-765.
- [64] I.F. Mohamed, Y. Yonenaga, S. Lee, K. Edalati, Z. Horita, Age hardening and thermal stability of Al–Cu alloy processed by high-pressure torsion, *Mater. Sci. Eng. A* 627 (2015) 111-118.
- [65] K. Edalati, D. Akama, A. Nishio, S. Lee, Y. Yonenaga, J.M. Cubero-Sesin, Z. Horita, Influence of dislocation–solute atom interactions and stacking fault energy on grain size of single-phase alloys after severe plastic deformation using high-pressure torsion, *Acta Mater.* 69 (2014) 68-77.

CHAPTER 3. COUPLED STRAIN-INDUCED ALPHA TO OMEGA PHASE TRANSFORMATION AND PLASTIC FLOW IN ZIRCONIUM UNDER HIGH PRESSURE TORSION IN A ROTATIONAL DIAMOND ANVIL CELL

This Section reproduces paper Feng B., Levitas V.I., and Kamrani M. Coupled strain-induced alpha to omega phase transformation and plastic flow in zirconium under high pressure torsion in a rotational diamond anvil cell. Materials Science and Engineering A, 2018, Vol. 731, 623-633.

Abstract

Strain-induced $\alpha \rightarrow \omega$ phase transformation (PT) in the zirconium (Zr) sample under compression and plastic shear in a rotational diamond anvil cell (RDAC) is investigated using the finite element method (FEM). The fields of the volume fraction of the ω phase, all components of the stress tensor, and plastic strain are presented. Before torsion, PT barely occurs. During torsion under a fixed applied force, PT initiates at the center of the sample, where the pressure first reaches the minimum pressure for strain-induced $\alpha \rightarrow \omega$ PT, p_{ε}^d , and propagates from the center to the periphery and from the symmetry plane to the contact surface. Salient increase of the shear friction stress and pressure at the center of a sample, so-called pressure self-multiplication effect observed experimentally for some other materials, is predicted here for Zr. It is caused by much higher yield strength of the ω phase in comparison with the α phase. Except at the very center of a sample, the total contact friction stress is equal to the yield strength in shear of the mixture of phases and the plastic sliding occurs there. Due to the reduction in sample thickness and radial material flow during torsion, the ω phase can be observed in the region where pressure is lower than p_{ε}^d , which may lead to misinterpretation of

the experimental data for p_{ε}^d . For the same applied force, torsion drastically promotes PT in comparison with the compression without torsion. However, the PT process in RDAC is far from optimal: (a) due to the pressure self-multiplication effect, the pressure in the transformed region is much higher than that required for PT; (b) the region in which PT occurs is limited by the pressure p_{ε}^d and cannot be expanded by increasing a shear under a fixed force; and (c) the significant reduction in thickness during torsion reduces the total mass of the high-pressure phase. These drawbacks can be overcome by placing a sample within a strong gasket with an optimized geometry. It is shown that, due to strong pressure heterogeneity, characterization of $\alpha \rightarrow \omega$ and $\alpha \rightarrow \beta$ PTs based on the averaged pressure contains large errors. The obtained results, in addition to providing an improved understanding of the strain-induced PTs, may be beneficial for the optimum design of experiments and the extraction of material parameters, as well as optimization and control of PTs by varying the geometry and loading conditions.

Keywords: Strain-induced phase transformations, Zirconium, High pressure, Rotational diamond anvil cell, Plasticity.

Introduction

Phase transformations (PTs) under high pressure and plastic shear are widespread in nature (e.g. as a mechanism of deep earthquakes [1-3]), physical experiments, and modern technologies. A rotational diamond anvil cell (RDAC), in which a large plastic shear in the sample without a hydrostatic medium is imposed by the rotation of anvils under a fixed axial compressive load [4-8], is utilized to study the effect of the plastic shear on PTs under high pressure. The introduction of plastic shear into the diamond anvil cell (DAC) leads to numerous exciting phenomena: (1) a significant reduction of transformation pressure by a factor of 2-5 in

Refs. [8-11] and even by a factor of nearly 10 (Refs. [5,12]), in comparison with those under a hydrostatic or nearly-hydrostatic condition; (2) the substitution of reversible PTs by irreversible ones [7,8,13], which allows one to retain high-pressure phases for possible practical applications; (3) the appearance of new high-pressure phases [4,8,11,13,14], which could not be obtained without plastic shear; (4) a reduction in a transformation pressure hysteresis sometimes to zero [8,9]; (5) fast, strain-controlled rather than time-controlled kinetics, in which plastic strain plays the role of a time-like parameter [7,8,10,13].

An important point in understanding PTs under high pressure is their classification, which is introduced in [10] and [13]. When surrounded by a liquid or gaseous medium, the sample in a diamond anvil cell is under the hydrostatic condition and PTs are considered to be pressure-induced. Without hydrostatic media or above the solidification pressure of the transmitting medium, the sample is under non-hydrostatic stresses or stress tensor; PTs under nonhydrostatic conditions but below the yield strength are considered as stress-induced PTs. If PTs occur while the sample is subjected to plastic deformation, e.g. during a thickness reduction under compression in DAC or torsion in RDAC, the PTs are classified as strain-induced ones [10,13]. While pressure-induced and stress-induced PTs start at pre-existing defects, which serve as pressure and stress tensor concentrators, strain-induced PTs occur at new defects continuously created during plastic flow [10,13]. For example, dislocations as the main type of defects are generated and densely pile up at the grain boundaries or other obstacles during plastic flow, which provides a strong stress concentration. Resultant local stresses at the stress concentrators may be much higher than the applied pressure and may reach the level required for PTs, which causes a significant reduction of transformation pressure (see analytical treatment in [10,13] and phase field simulations in [15,16]) in comparison with the PT pressure under the hydrostatic

condition. Our focus here is on the plastic strain-induced PTs under pressure. Multiscale continuum thermodynamic and kinetic theories to characterize strain-induced PTs were initially proposed in [10,13]; the current state is presented in a short review in [17]. In particular, at the microscale, a plastic strain-controlled pressure-dependent kinetics (see Eq. (7)) is obtained by a coarse graining of the nanoscale theory. This kinetic equation is included in macroscale theory and used to study the coupled plastic flow and strained-induced PTs in DAC [18-21] and RDAC [22-25], using FEM.

In this paper, we will study the strain-induced PT in zirconium (Zr) from the α phase to the ω phase under compression and torsion in RDAC. Zr has widespread applications in various areas such as the space and aeronautic industry (e.g. in space vehicle parts due to its excellent resistance to heat), nuclear industry (e.g. for cladding of nuclear reactor fuels due to its low neutron-capture), and biomedical industry (e.g. dental implants and other restorative practices, knee and hip replacements, and surgical appliances, due to its high wear resistance). At normal pressure and temperature, Zr has a hexagonal closed-packed (hcp) structure (α phase). When the pressure is increased at room temperature, in the pressure range of 0.25-7 GPa [27-37], the martensitic PT from the α to ω phase occurs. With a liquid medium (4:1 ethanol:methanol), $\alpha \rightarrow \omega$ PT is observed at around 7 GPa [31], which is considered as a pressure-induced PT. With large plastic shear, plastic strain-induced $\alpha \rightarrow \omega$ PT occurs at 2 GPa [29]. While subjected to high pressure torsion (HPT) treatment under unconstrained conditions, $\alpha \rightarrow \omega$ PT is detected at 1 GPa [32] during compression before torsion; during torsion, this PT occurs at a pressure as low as 0.25 GPa [33]. The main problem in [32] and [33] is that the pressures reported are defined as the total force over the contact area, while the pressure distribution is strongly heterogeneous; see [26] and below. The initiation of $\alpha \rightarrow \omega$ PT was observed at

intermediate pressures between these extremes in [29,31-33]. For instance, it occurs around 6 GPa under nonhydrostatic compression in a multi-anvil system [35]; Olinger and Jamieson obtained PT transition pressure at 3.9 GPa and suggested that the differences in PT pressure for Zr in a broad range is due to either shear stresses or oxygen content [34].

At ambient pressure as the temperature is increased from room temperature to 1135 K, the α to the bcc β PT takes place. At ambient temperature and under a hydrostatic loading, the ω phase transforms to the bcc β at 30 GPa, but the β phase is unstable and disappears after unloading. The addition of 2.5wt.% Nb to Zr causes significant decrease (at least 30 times) of the transition pressure from the α to β phase [33]. Recently, the β phase has been experimentally stabilized at normal pressure after 5 turns of the plunger at 3 GPa [38]. This pressure [38] is averaged over the contact surface as the ones in [32,33]. The stabilized β phase was later obtained by unconstrained HPT along with the ω phase at 1 GPa [32] and even 0.25 GPa [33]. While there has been significant developments in HPT (see a review [39]), and HPT is broadly used to study the PTs in Zr, the only available information is an averaged pressure (force per total initial area) and number of turns for initiation of $\alpha \rightarrow \omega$ and $\alpha \rightarrow \beta$ PTs. Thus, the system is considered as a black box. Any information on the fields of pressure, plastic strain, and volume fraction of phases in the Zr sample during HPT, which is necessary for understanding actual physical, thermodynamic, and kinetic processes of interaction between PT and plasticity, is absent.

In our preceding paper [26], the $\alpha \rightarrow \omega$ strain-induced PT is in Zr under compression in DAC was studied. The obtained results have been utilized for the qualitative analysis interpretation of known experimental data on pressure-, stress-, and strain-induced $\alpha \rightarrow \omega$,

$\alpha \rightarrow \beta$, and $\omega \rightarrow \beta$ PTs in Zr under compression and HPT, but without having a solution for HPT for Zr. In the current paper, the strain-induced $\alpha \rightarrow \omega$ PT in Zr under compression and torsion in RDAC will be studied with the same material parameters as in [26]. While there are FEM studies in RDAC [22-25], these all focus on the generic material parameters, and none are based on the real materials. Here, we performed the first study of PT in the real material (i.e. Zr) in RDAC. The results obtained will be used in comparison with those for DAC [26], to interpret the experimental phenomena, and to suggest how to improve PT conditions in RDAC.

Problem Formulation

Geometry and Boundary Conditions

As in [26], the geometric parameters of RDAC that are generally accepted in experiments (e.g. in [5-7]) will be used in our FEM simulation. Typically, the flat [5-7] contact surface of an anvil is used for pressures under 50 GPa, while a bevel angle of 8.5° for the anvil contact surface is used for multi-megabar pressures [41]. A flat diamond anvil is utilized (see Figure 1c) in our model because the maximum pressure is below 5 GPa (see Figure 2). The sample is initially pre-indented to a thickness of $50 \mu\text{m}$ at $r \leq 150 \mu\text{m}$. Due to the symmetry, a quarter of the sample and anvil structure is considered (see Figure 1a). To avoid divergence of the computations due to the penetration of finite elements between diamond and sample if the sharp angle at point C is used, a smooth corner is included in the geometric schematic (see Figure 1b).

The boundary conditions for a quarter of a structure in Figure 1a are as follows:

The normal stress σ_n is applied at the top surface of the anvil. In the course of torsion, the rotation is applied to the top surface of the anvil with a constant normal stress σ_n .

The radial displacement u_r and shear stresses τ_{rz} and $\tau_{z\varphi}$ are zero at the symmetry axis $r = 0$ (the lines AB and BG for the anvil and the sample, respectively).

At the contact surface between the anvil and sample (the line BCD), the combined Coulomb and plastic friction model, which will be introduced below in this section, is used.

At the symmetry plane $z = 0$ (the plane GH), the radial shear stress $\tau_{rz} = 0$, and the circumferential displacement and the axial displacement are both zero $u_\varphi = u_z = 0$.

Other surfaces in Figure 1a not mentioned above are stress-free.

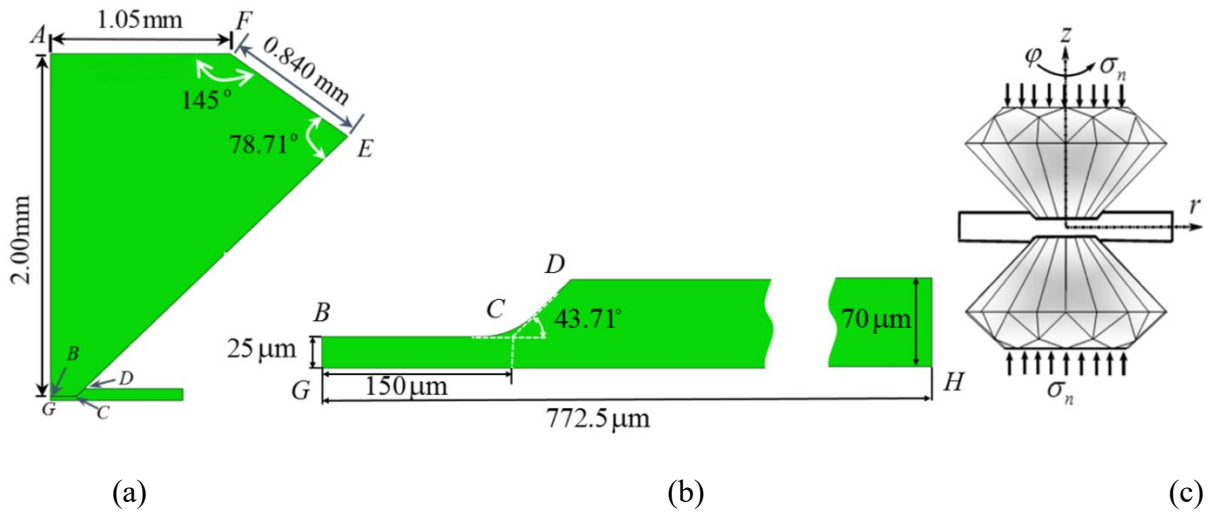


Figure 1. (a) A quarter of the sample and the anvil in the initial undeformed state with the geometric parameters, (b) the geometry of a quarter of the sample, (c) a RDAC schematic.

Material Model

It was found in [42] for a wide range of materials (metals, rocks, pressed powders, etc.) that above some level of plastic strain, initially isotropic polycrystalline materials deform as perfectly plastic and isotropic; their yield surface is independent of accumulated plastic strain and plastic strain history. Because the maximum pressure is around 5 GPa, we can also neglect the pressure dependence of the elastoplastic properties (similar to [22-26,37]). Thus, isotropic

and perfectly plastic behavior with the von Mises yield condition is assumed for the Zr sample. The elastic properties and yield strength are considered to be phase-volume-fraction-dependent. The model for Zr here is basically identical to the 2D model in [26] but will be used for more general 3D loading. A system of equations considering coupled elasto-plasticity and strain-induced PT is summarized as follows.

Kinematic decomposition of the symmetric part of the velocity gradient \mathbf{d} :

$$\mathbf{d} = \left(\dot{\mathbf{F}} \cdot \mathbf{F}^{-1} \right)_s = \overset{\nabla}{\boldsymbol{\varepsilon}}_e + \frac{1}{3} \dot{\bar{\varepsilon}}_t \mathbf{I} + \mathbf{d}_p, \quad \varepsilon_t = \bar{\varepsilon}_t c \quad (1)$$

Where $\overset{\nabla}{\boldsymbol{\varepsilon}}_e$ is the objective Jaumann time derivative of the elastic strain; \mathbf{I} is the second-rank unit tensor; $\bar{\varepsilon}_t$ is the transformation volumetric strain for a complete PT; and c is the volumetric fraction of the high-pressure (ω) phase.

Hooke's elasticity law:

$$\boldsymbol{\varepsilon}_e = \frac{1}{E} \left[\boldsymbol{\sigma} - \nu \left(\text{tr}(\boldsymbol{\sigma}) \mathbf{I} - \boldsymbol{\sigma} \right) \right], \quad \text{tr}(\boldsymbol{\sigma}) = \sigma_{rr} + \sigma_{zz} + \sigma_{\varphi\varphi} \quad (2)$$

Where Young's modulus $E = (1-c)E_1 + cE_2$ and Poisson's ratio $\nu = (1-c)\nu_1 + c\nu_2$; in this paper, subscripts 1 and 2 represent the low- and high-pressure phases, respectively.

Von Mises yield condition for a two-phase mixture:

$$\sigma_i = \left(\frac{3}{2} \mathbf{s} : \mathbf{s} \right)^{0.5} \leq \sigma_y(c) = (1-c)\sigma_{y1} + c\sigma_{y2}, \quad (3)$$

Where \mathbf{s} is the deviator of the Cauchy stress $\boldsymbol{\sigma}$.

J_2 flow rule in the plastic region:

$$\sigma_i = \sigma_y(c), \quad \mathbf{d}_p = \lambda \mathbf{s}, \quad \lambda \geq 0 \quad (4)$$

in the elastic region:

$$\sigma_i \leq \sigma_y(c), \quad \mathbf{d}_p = 0 \quad (5)$$

Where σ_i is the effective stress and λ is a parameter that is determined by iterative satisfaction of the yield condition.

Equilibrium equation:

$$\nabla \cdot \boldsymbol{\sigma} = 0, \quad (6)$$

In the micro-scale theory [10,13], the strain-controlled kinetic of strain-induced PTs can be characterized as:

$$\frac{dc}{dq} = 10k \frac{(1-c)\bar{p}_d H(\bar{p}_d) \frac{\sigma_{y2}}{\sigma_{y1}} - c\bar{p}_r H(\bar{p}_r)}{c + (1-c) \frac{\sigma_{y2}}{\sigma_{y1}}}, \quad (7)$$

where k is the kinetic parameter; $\bar{p}_d = \frac{p - p_\varepsilon^d}{p_h^d - p_\varepsilon^d}$ and $\bar{p}_r = \frac{p - p_\varepsilon^r}{p_h^r - p_\varepsilon^r}$ are the dimensionless characteristic pressures for direct and reverse PTs; p_ε^d is the minimum pressure below which direct strain-induced PT (direct indicates the PT from low-pressure to high-pressure phase) is impossible; p_ε^r is the maximum pressure above which reverse strain-induced PT (reverse indicates the PT from high-pressure to low-pressure phase) cannot occur; p_h^d and p_h^r are the pressures for direct and reverse PTs under the hydrostatic condition, respectively; H is the Heaviside step function; and q is the accumulated plastic strain, defined as $\dot{q} = (2/3 \mathbf{d}_p : \mathbf{d}_p)^{1/2}$.

Friction Model

In the Coulomb friction model, no relative displacement will occur between surfaces in contact as long as the friction stress τ is smaller than the critical friction stress defined as

$\tau_{crit} = \mu \sigma_c$, where μ is the friction coefficient and σ_c is the normal contact stress. This critical

friction stress should be redefined for the elastoplastic materials because, when the magnitude of the friction stress τ reaches the yield strength in shear, τ_y (e.g. $\tau_y = \sigma_y / \sqrt{3}$ in the von Mises yield criterion), relative slipping can occur even if $\tau < \mu\sigma_c$. In this paper, the critical friction stress is defined as $\tau_{crit} = \min(\mu\sigma_c, \tau_y(c))$ and μ is considered to be constant for the simplest case. Yield strength in shear is considered to be dependent on PT evolution as $\tau_y(c) = (1-c)\tau_{y1} + c\tau_{y2}$, where τ_{y1} and τ_{y2} are the yield strengths in shear of the low- and high-pressure phases, respectively. In the generalized axisymmetric models, the three-dimensional friction stress $\boldsymbol{\tau}$ along the contact surface is composed of τ_{rz} along the radial direction and $\tau_{\phi z}$ along the circumferential twist direction as $\tau = |\boldsymbol{\tau}| = (\tau_{rz}^2 + \tau_{\phi z}^2)^{0.5}$.

Redefinition of the critical friction stress as $\tau_{crit} = \min(\mu\sigma_c, \tau_y(c))$ results in a sudden change of contact conditions between cohesion and sliding. This may cause convergence issues in the FEM methods in the iterative process, especially for our model, where a large slipping can happen. Hence, to mitigate this problem, a small elastic reversible tangential slip u_e is substituted for the cohesion condition [43]. In other words, the contact relative displacement is decomposed into elastic (reversible) sliding u_e and plastic (irreversible) slipping u_s as $u_c = u_e + u_s$. The elastic sliding can be physically interpreted as the elastic deformation of the thin contact layer, while slipping corresponds to the plastic flow in this layer. In this paper, u_{crit} is considered to be equal to 0.5% of the average element length for the fine-mesh discretization.

In this paper, a linear relation $\tau = k_s u_e$, where k_s is the contact stiffness, is considered.

The contact stiffness can be determined from $\tau_{crit} = k_s u_{crit}$ to be $k_s = \tau_{crit} / u_{crit}$. Therefore, k_s

depends on the normal stress σ_n and the yield strength in shear τ_y . The complete system of equations for the combined Coulomb and plastic friction is as follows:

Decomposition of contact relative displacement into elastic sliding and irreversible slipping:

$$\mathbf{u}_c = \mathbf{u}_e + \mathbf{u}_s, \quad (8)$$

Critical shear stress:

$$\tau_{crit} = \min(\mu\sigma_c, \tau_y(c)), \quad (9)$$

Yield strength in shear:

$$\tau_y(c) = (1-c)\tau_{y1} + c\tau_{y2}, \quad (10)$$

Elastic sliding vector:

$$\begin{cases} \mathbf{u}_e = \frac{u_{crit}}{\mu\sigma_c} \boldsymbol{\tau}, & \text{if } \mu\sigma_c < \tau_y(c) \\ \mathbf{u}_e = \frac{u_{crit}}{\tau_y(c)} \boldsymbol{\tau}, & \text{if } \mu\sigma_c \geq \tau_y(c) \end{cases} \quad (11)$$

Sliding rule:

below the critical shear stress:

$$|\dot{\mathbf{u}}_s| = 0, \quad \text{if } \tau = |\boldsymbol{\tau}| = (\tau_{rz}^2 + \tau_{\varphi z}^2)^{0.5} < \tau_{crit} \quad (12)$$

at the critical shear stress:

$$\begin{cases} \dot{\mathbf{u}}_s = \frac{|\dot{\mathbf{u}}_s|}{\mu\sigma_c} \boldsymbol{\tau}, & \text{if } \mu\sigma_c \leq \tau_y(c) \\ \dot{\mathbf{u}}_s = \frac{|\dot{\mathbf{u}}_s|}{\tau_y(c)} \boldsymbol{\tau}, & \text{if } \mu\sigma_c > \tau_y(c) \end{cases} \quad (13)$$

Material Parameters and Numerical Procedure

The material parameters used for diamond and Zr in this paper are the same as those used in [26]. The diamond is considered as an isotropic elastic material with the bulk modulus B and Young's modulus E of 443 GPa [44] and 1048.5 GPa [45], respectively. Therefore, based on Hooke's law, Poisson's ratio ν is 0.1055. The Young's modulus, Poisson's ratio, [46] and yield strength [47] for Zr phases are as follows:

For the α phase: $E_1 = 90.9$ GPa, $\nu_1 = 0.344$ and $\sigma_{y1} = 180$ MPa

For the ω phase: $E_2 = 113.8$ GPa, $\nu_2 = 0.305$ and $\sigma_{y2} = 1180$ MPa

The transformation pressures for pressure- and strain-induced PTs strongly depend on impurities such as elements of oxygen and nitrogen [30], the initial mechanical state of the material, and the measurement conditions. As discussed in the Introduction, there is an essential scatter of transformation pressures in literature. Significant corrections to the PT pressures in [33] were suggested in [26] due to operating by the averaged pressure (force per unit initial area) while the pressure distribution is strongly heterogeneous. We use $p_\varepsilon^d = 1.7$ GPa and $p_\varepsilon^r = -2$ GPa for direct and reverse strain-induced PTs, respectively. For pressure-induced PTs, we accept $p_h^d = 7$ GPa and $p_h^r = -3.7$ GPa for direct and reverse strain-induced PTs, respectively. The kinetic parameter is considered $k=10$. Based on the experimental data given in [48], the transformational volumetric strain is $\bar{\varepsilon}_t = -0.014$.

ABAQUS FEM code [43] was used in our simulations. To solve the strain-controlled kinetics Eq. (7), the ABAQUS user subroutines [43] USDFLD and HETVAL are used. In these subroutines, the thermal strain and temperature are treated as transformation strain and the

volume fraction of high-pressure phase c , respectively. To implement the friction model defined in next section, the user subroutine FRIC [43] in ABAQUS is used.

Study of Coupled Plastic Flow and Phase Transformations

Distribution of the Pressure and Volume Fraction of the ω Phase

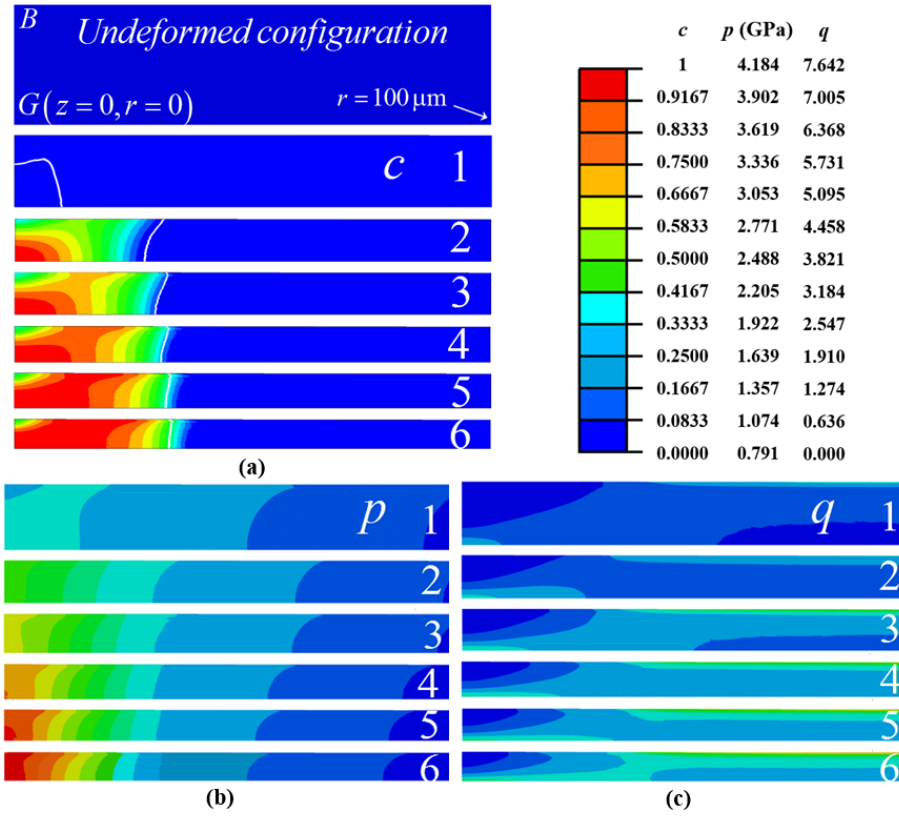


Figure 2. Distributions of the volume fraction c of the high-pressure ω phase of Zr (a), pressure p (b), and accumulated plastic strain q (c), for $0 \leq r \leq 100 \mu\text{m}$, before and during torsion under the applied constant stress $\sigma_n = 27.6 \text{ MPa}$. Designations of the rotation angles: 1: $\varphi = 0.0$; 2: $\varphi = 0.16$; 3: $\varphi = 0.32$; 4: $\varphi = 0.48$; 5: $\varphi = 0.64$; and 6: $\varphi = 0.8$ radians. The white line in (a) corresponds to the pressure equal to p_ε^d .

In this section, we will discuss the plastic flow and strain-induced $\alpha \rightarrow \omega$ PT in Zr during torsion under a fixed axial compressive load. Figure 2 presents the evolutions of the volume fraction c of the ω phase of Zr, pressure p , and accumulated plastic strain q in the part of the Zr sample for $0 \leq r \leq 100 \mu\text{m}$ with a rising rotation angle.

The applied compressive stress on the top surface of the upper anvil is $\sigma_n = 27.6 \text{ MPa}$, as shown in Figure 1c. If the resultant force is divided by the area of the flat surface of an anvil, an averaged pressure on the sample surface is $0.0276 * (1.05/0.15)^2 = 1.35 \text{ GPa}$. Because there is an additional inclined contact surface between the diamond and the sample, it should be even smaller. If we consider the horizontal area with radius corresponding to point D, the mean pressure is $0.0276 * (1.05/(0.15 + .047))^2 = 0.784 \text{ GPa}$.

The white lines in Figure 2a correspond to pressure $p = p_\varepsilon^d$, which is the minimum pressure for strain-induced PTs to the high-pressure phase, and on the left and right sides of these lines, pressures are higher and lower than p_ε^d , respectively. Figure 2a shows that the sample thickness reduces significantly when the sample is compressed under $\sigma_n = 27.6 \text{ MPa}$ without rotation, leading to a plastic deformation in the entire sample. Although the pressure at the center is higher than the minimum pressure for $\alpha \rightarrow \omega$ PT, p_ε^d , the volume fraction of the ω phase there is lower than 0.0883; therefore, the PT is not visible and the color of the volume fraction in the entire sample is dark blue. With such a small volume fraction, the ω phase should not be detected in an experiment under compression either. This is consistent with experiments in [33] because an averaged pressure here, 0.784 GPa, is smaller than 1 GPa, at which the ω phase was not detected under compression. The phase transformation starts at the center of the sample,

where the pressure reaches the p_ε^d first, and it propagates from the center to the periphery with an increase in rotation angle as the white line with a pressure of p_ε^d moves to the periphery. During rotation, the thickness of the sample significantly reduces, causing an increase of the pressure gradient due to the simplified equilibrium equation

$$\frac{\partial p}{\partial r} = 2 \frac{\tau_{rz}^c}{h} \quad (14)$$

where h is the sample thickness and τ_{rz}^c is the friction shear stress on the contact surface in the radial direction. Another reason for a rising pressure gradient in the transforming region is the increase in shear stress τ_{rz} (see τ_{rz} in Figure 6a or 7a) due to material hardening during PT. Figure 2c presents the evolution of the plastic strain q . Because the plastic shear strain is large near the contact surface at the periphery of a sample, the maximum plastic strain is localized there as well (see Figure 2c). At $r=0$, the shear stress and strain are zero, and thickness reduction in this region is mostly caused by the radial flow of material near the symmetry plane. Small plastic straining near the contact surface at the sample center leads to a slow PT rate there (Eq. (7)). According to Figures 2a and 3, for compression before torsion under the applied normal stress of $\sigma_n=27.6$ MPa, there is no detectable PT near the contact surface, and there is only a small region of a slightly transformed phase at the center of the sample. However, during torsion under the same normal stress, PT evolves and completes in a large region of the sample which includes the contact surface.

Figure 3 plots the pressure and the volume fraction of the high-pressure phase along the contact surface. Due to the symmetry, the pressure gradient is zero at the center-line z axis. In the untransformed region at the periphery, the pressure gradient is almost constant because the friction shear stress τ_{rz} (see in Figure 7c) in Eq. (14) is constant. The pressure gradient in the

two-phase region increases because the yield strength increases with the volume fraction c , which, in turn, varies along the contact surface. The increase in pressure and the pressure gradient during the rotation shown under constant applied force in Figure 3 is caused by friction stress growth during phase transformation and thickness reduction during material radial flow. This was observed in experiments on different materials [8, 9, 11] and referred to as the pressure self-multiplication effect. Thus, our prediction of the pressure self-multiplication effect in Zr has conceptual confirmation for PTs in KCl and fullerene [8, 9, 11]. In return, this increase in pressure intensifies the PT rate in this region; see Eq. (7). While the pressure reaches its maximum in the central region of the contact surface, the volume fraction of the ω phase in this region is relatively small due to the relatively small plastic deformation in this region. With an increasing rotation angle, there is a significant material flow from the center to the periphery and, consequently, a significant thickness reduction. During this radial material flow, the two-phase zone flows into the region with pressure lower than p_ε^d . According to Figures 2a and 3, the ω phase can be found in the region where pressure is lower than p_ε^d ; there, the PT cannot occur. If p_ε^d is defined as the minimum pressure in the transformed region, this may lead to significant misinterpretation of experiments.

As in traditional in HPT, the averaged pressure is used to describe the pressure for PT and it is from the total applied compressive force divided by the contact surface. At room temperature, the martensitic PT from the α to ω phase occurs and is reported in the pressure range of 0.25-7 GPa [27-37], among which HPT is mostly used.

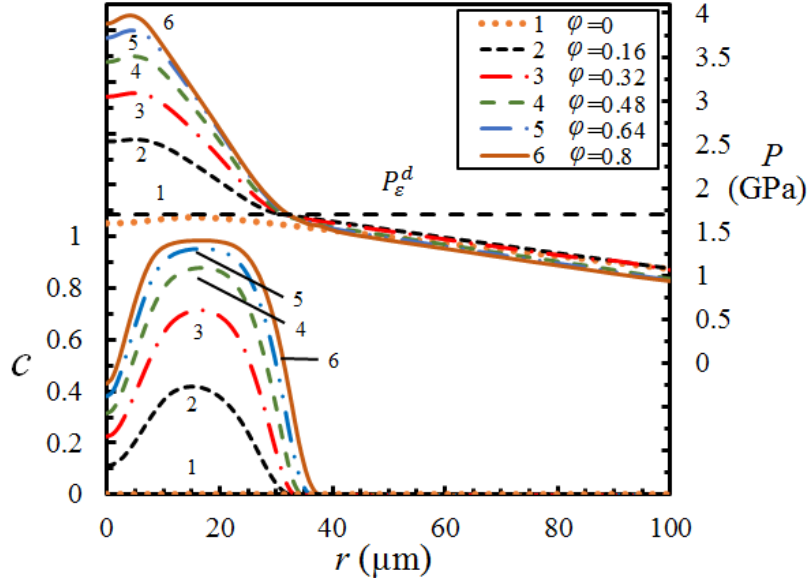


Figure 3. Distributions of volume fraction c of the high-pressure phase and pressure p at the contact surface between diamond and sample for $0 \leq r \leq 100 \mu\text{m}$ before and during torsion under the applied constant normal stress $\sigma_n = 27.6 \text{ MPa}$. 1: $\varphi = 0.0$, 2: $\varphi = 0.16$, 3: $\varphi = 0.32$, 4: $\varphi = 0.48$, 5: $\varphi = 0.64$, 6: $\varphi = 0.8$ radians.

Similar to the PT under compression in DAC [26], in RDAC Figure 3 demonstrates that PT cannot be characterized by the averaged pressure, as this was done in all previous experimental papers (e.g., [32,33,36]). During torsion at a constant averaged pressure, the maximum pressure grows from 1.8 GPa to 4.0 GPa in Figure 10 while average pressure (0.784 GPa) does not change, i.e. by a factor of 2.2. It is slightly larger than a factor of 2, which was estimated for DAC in [26]. While the geometry of a sample in RDAC differs from that in HPT, some qualitative conclusions should be the same. During compression, the minimum pressure for the strain-induced PT $p_\varepsilon^d = 1.7 \text{ GPa}$ is reached at the averaged pressure of 0.784 GPa, which is 2.2 times lower. It is lower than the upper bound of 3, estimated in [26], due to the effect of the

inclined part of the sample, which is absent in HPT. This multiplier 3 was used in [26] to correct the magnitude of p_ε^d for $\alpha \rightarrow \omega$ PT based on the averaged pressure in [32,33]. The maximum pressure after torsion exceeds an averaged pressure of 0.784 GPa by a factor of 5. This factor should be used to correct the minimum pressure for strain-induced PT p_ε^d for $\alpha \rightarrow \beta$ transformation based on the averaged pressure in [32,33]. Strong heterogeneity in all fields and difference in geometric conditions (which are very seldom specified), is one of the important sources of explanation of the strong scatter in transformation pressures for $\alpha \rightarrow \omega$ PT in Zr in [27-37].

Rotation above some critical angle is not effective. The amount of high-pressure phase cannot grow anymore because the region with pressure larger than p_ε^d is limited and PT is almost completed in it. Also, the thickness of a sample reduces with rotation, the high-pressure phase flows to the region where $p < p_\varepsilon^d$, and reverse PT occurs. Increasing the applied normal stress σ_n is a way to increase the span of the transformed region. Figure 4 shows the distributions of the volume fraction of the high-pressure phase and pressure in the sample for three different applied normal stresses for the rotation angle $\varphi=0.8$. The span of the transformed region increases and PT advances further at the center of the contact surface when the applied normal stress increases from 27.6 MPa to 28.1 MPa and to 28.6 MPa, which correspond to the final thicknesses of 12.6 μm , 12.18 μm , and 11.94 μm , respectively.

If the same stresses σ_n were applied to the DAC without torsion, PT would not even reach the contact surface. Therefore, superposing torsion in the RDAC significantly reduces the normal force, i.e. the averaged pressure, for having a large transformed region. Reduction in

force also reduces normal stresses and deformations in the anvils. Therefore, the RDAC is preferable over the DAC in high-pressure experiments.

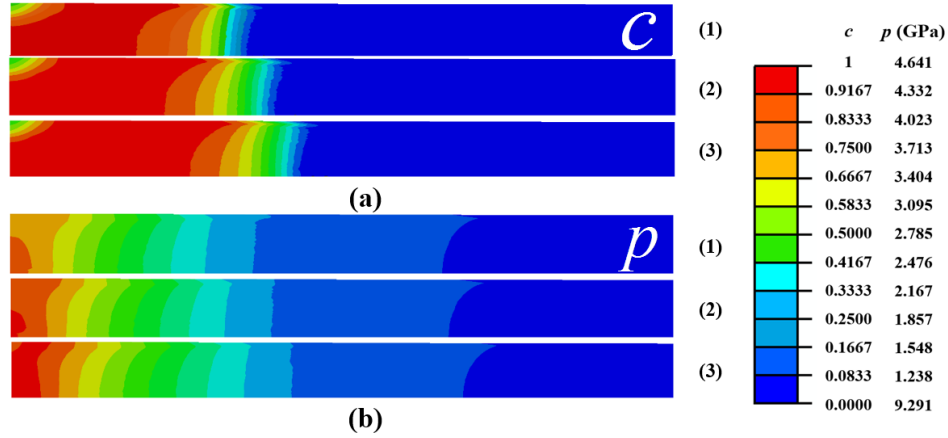


Figure 4. (a) Distributions of the volume fraction c of the ω phase and (b) pressure p for $0 \leq r \leq 100 \mu\text{m}$, under applied constant normal stress $\sigma_n = 27.6 \text{ MPa}$ (1), $\sigma_n = 28.1 \text{ MPa}$ (2), and $\sigma_n = 28.6 \text{ MPa}$ (3) after a rotation of $\varphi = 0.8$ radian.

Despite the advantages in the PT process in RDAC compared to those in DAC, there are clear drawbacks. Thus, pressure in the transformed region is much higher than the minimum PT pressure p_ε^d . Such a pressure is not required for PT but could not be avoided for the geometry under consideration. Second, the region in which PT occurs is limited by the condition $p > p_\varepsilon^d$ and cannot be increased by increasing shear under fixed force. Third, significant reduction in thickness during torsion reduces the total mass of the high-pressure phase. Fourth, the transformed material can flow to the region with $p < p_\varepsilon^d$ during rotation; then the reversed PT may, in principle, occur. The way to overcome these drawbacks is to use the sample within a strong gasket, optimize the geometric parameters of the gasket, and achieve nearly-homogeneous pressure distribution within the sample, which does not change obviously during torsion and PT.

After a simplified analytical optimization, this was demonstrated in experiments for PT from hexagonal to superhard wurtzitic boron nitride [7]. This was later achieved in FEM simulations in RDAC [23].

Distribution of the Normal and Shear Stresses

Figure 5 presents the evolution of the distribution of the normal stresses σ_{rr} , σ_{zz} , and $\sigma_{\varphi\varphi}$ in the sample before and during rotation. The distributions of σ_{rr} and $\sigma_{\varphi\varphi}$ are almost identical. Because the deviation of σ_{zz} from σ_{rr} and $\sigma_{\varphi\varphi}$ is limited by the yield strength, the general tendency in the evolution of normal stresses in Figure 5 is close to that for pressure evolution in Figure 2c. At the center, all normal stresses and their radial gradients significantly increase with a rising rotation angle due to material hardening during PT and the thickness reduction during material radial flow. Stress σ_{zz} is nearly unchanged along the thickness, excluding the very central part of the sample. In contrast, σ_{rr} and $\sigma_{\varphi\varphi}$ reduce along the sample thickness due to the reduction of the shear stress τ_{rz} from the maximum at the contact surface to zero at the symmetry plane (See Figure 6). Thus, the magnitude of the difference $\sigma_{zz} - \sigma_{rr}$ (and $\sigma_{zz} - \sigma_{\varphi\varphi}$) should increase from the contact surface to the symmetry plane to satisfy the yield condition.

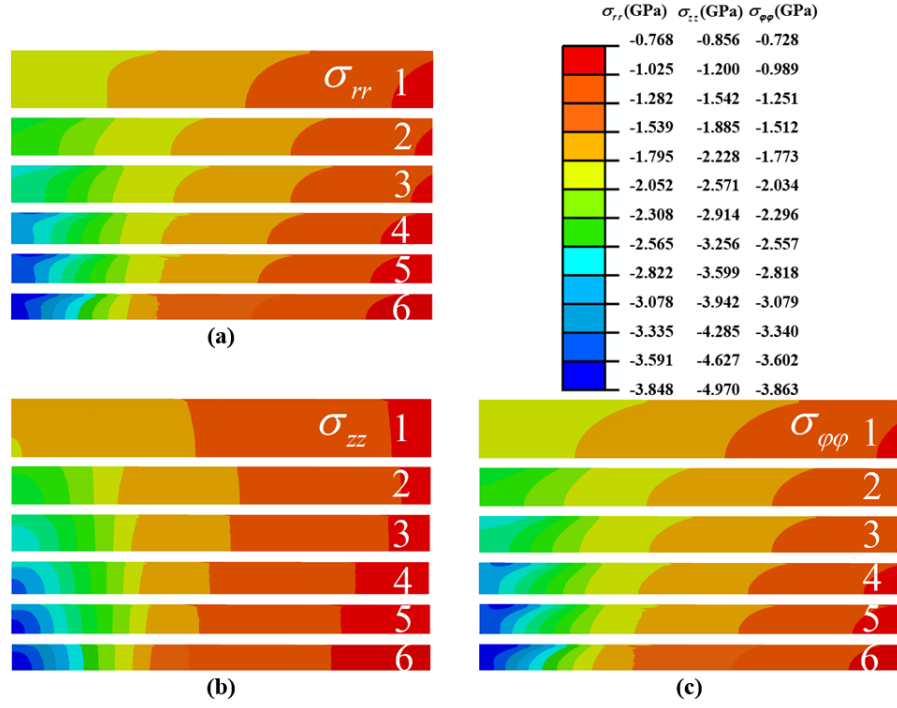


Figure 5. Distributions of normal stresses σ_{rr} (a), σ_{zz} (b), and $\sigma_{\phi\phi}$ (c) in the sample for

$0 \leq r \leq 100 \mu\text{m}$ before and during torsion under the applied constant normal stress $\sigma_n = 27.6$

MPa. 1: $\phi=0.0$, 2: $\phi=0.16$, 3: $\phi=0.32$, 4: $\phi=0.48$, 5: $\phi=0.64$, 6: $\phi=0.8$.

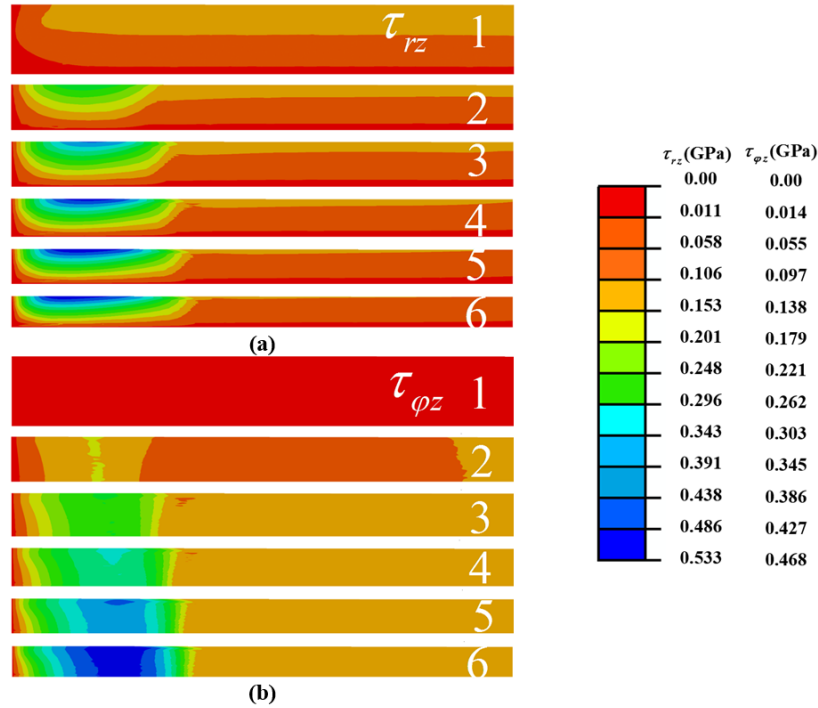


Figure 6. Distribution of shear stresses τ_{rz} (a) and $\tau_{\phi z}$ (b) in the sample for $0 \leq r \leq 100 \mu\text{m}$ before and during torsion under the applied constant normal stress $\sigma_n = 27.6 \text{ MPa}$. 1: $\phi = 0.0$, 2: $\phi = 0.16$, 3: $\phi = 0.32$, 4: $\phi = 0.48$, 5: $\phi = 0.64$, 6: $\phi = 0.8$.

The evolution of shear stresses τ_{rz} and $\tau_{\phi z}$ in the sample during torsion is presented in Figure 6. Due to symmetries, the radial shear stress τ_{rz} at the symmetry plane ($z=0$) and at the symmetry axis ($r=0$) is zero. It increases from the symmetry plane to the contact surface, where it reaches its maximum. Distinct from τ_{rz} with a large gradient along the thickness, the circumferential shear stress $\tau_{\phi z}$ is almost unchanged along the thickness. During PTs, material hardening, which increases with an increasing volume fraction c , induces an increase in the shear stresses and their gradient in the transformed region. During compression before torsion, τ_{rz} reaches the yield stress in shear of the α phase in the major part of the contact surface (Figure 7), which causes a constant pressure gradient in Figure 2. During torsion, $\tau_{\phi z}$ increases, causing the reduction of τ_{rz} to maintain the total shear stress at the contact surface $\tau = (\tau_{rz}^2 + \tau_{\phi z}^2)^{0.5}$ equal to the yield strength in shear. The total shear stress reaches about 6.5 times the yield strength in shear of the α phase in the nearly fully-transformed region in Figure 7, which is close to the ratio of the yield strengths of the ω and α phases. In the major region, except at the center of a sample, the τ is equal to the yield strength in shear, indicating that the plastic sliding is allowed there (see Figure 7).

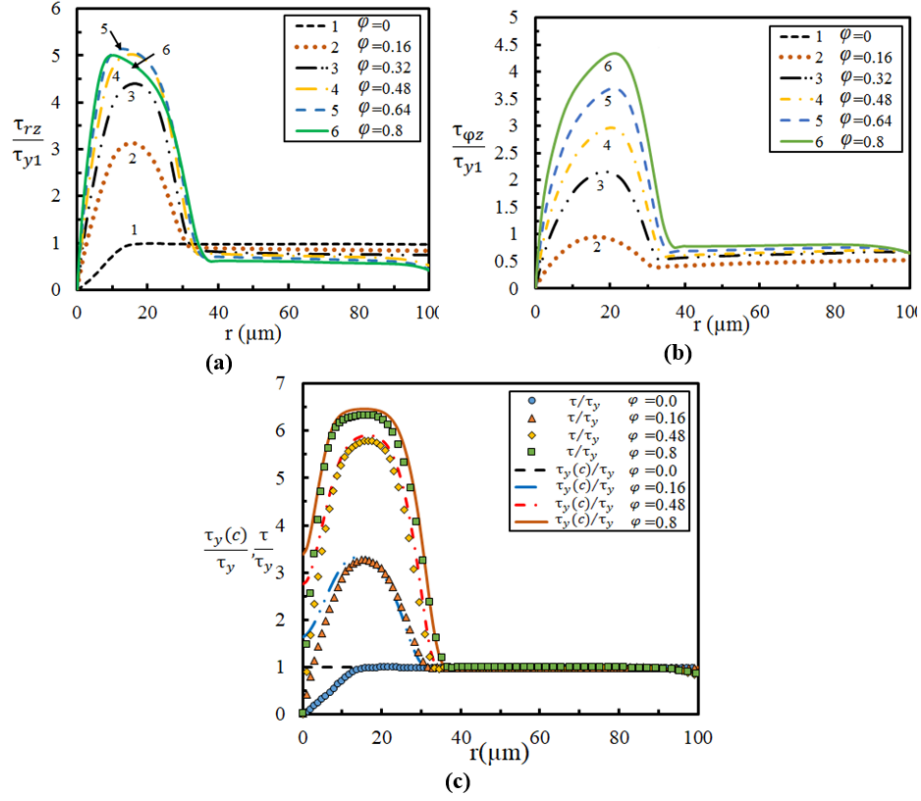


Figure 7. Distributions of dimensionless friction shear stresses τ_{rz}/τ_{y1} (a) and $\tau_{\varphi z}/\tau_{y1}$ (b), yield stress in shear $\tau_y(c)/\tau_{y1}$, and total shear stress τ/τ_{y1} (c) at the contact surface of the sample for $0 \leq r \leq 100 \mu\text{m}$, before and during torsion under the applied constant normal stress $\sigma_n = 27.6$ MPa. In (a) and (b), 1: $\varphi = 0.0$, 2: $\varphi = 0.16$, 3: $\varphi = 0.32$, 4: $\varphi = 0.48$, 5: $\varphi = 0.64$, 6: $\varphi = 0.8$.

Contact Sliding, Deformation of an Anvil, and Reduction in Sample Thickness

The relative radial displacement d and relative circumferential rotation angle β between the sample and the diamond anvil at the contact surface is shown in Figures 8a and 8b, respectively. Figure 8 shows that the radial and circumference slip exists everywhere except the central region of the contact surface, where the cohesion condition holds. Material flows from the center to the periphery, and the slope of radial slip displacement d increases with an increase in the radial coordinate. The tendencies of the relative radial displacement d and relative

circumferential rotation angle β are very similar. The relative circumferential rotation angle β is defined as $\beta = \beta_{diamond} - \beta_{sample}$, in which $\beta_{diamond}$ (or β_{sample}) is the rotation angle of diamond (or sample) with respect to the symmetric plane ($z=0$). Initially, before the rotation starts, β is zero everywhere at the contact surface. With the rotation angle $\varphi=0.16$ radians, Figure 8b shows that the cohesion zone between the diamond and sample surface is localized in the region of $r \leq 20 \mu\text{m}$, and beyond this region, the relative circumferential rotation β increases with a rising radial coordinate. At the periphery, the circumferential sliding is larger than that at the center, which is caused by a lower contact stress σ_c at the periphery and a larger circumferential displacement of the anvil at the periphery. In addition, with the increase of the rotation angle φ , the cohesion region decreases and β increases at the non-cohesion zone. Figure 7 shows that the friction stress is equal to the yield strength in shear in most of the contact region, which means that the plastic sliding occurs almost everywhere at the contact surface. This result shows the importance of taking plastic sliding along the contact surface into account. Without this plastic friction condition, radial and circumferential sliding would be suppressed, the sample thickness would be artificially increased, and the pressure distribution would be changed as well.

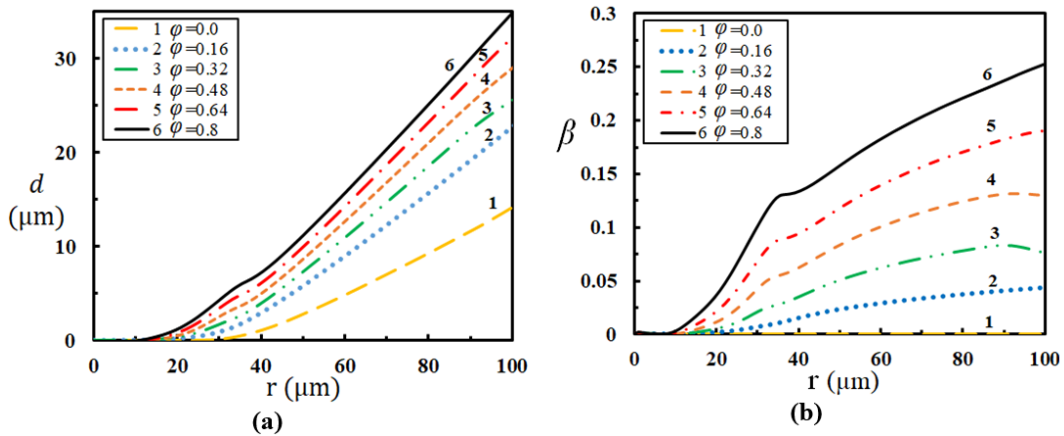


Figure 8. Distributions of radial d (a) and relative circumferential rotational angle β (b)

between the sample and the diamond anvil at the contact surface for $0 \leq r \leq 100 \mu\text{m}$ before and during torsion under applied constant normal stress $\sigma_n = 27.6 \text{ MPa}$, 1: $\varphi = 0.0$, 2: $\varphi = 0.16$, 3: $\varphi = 0.32$, 4: $\varphi = 0.48$, 5: $\varphi = 0.64$, 6: $\varphi = 0.8$.

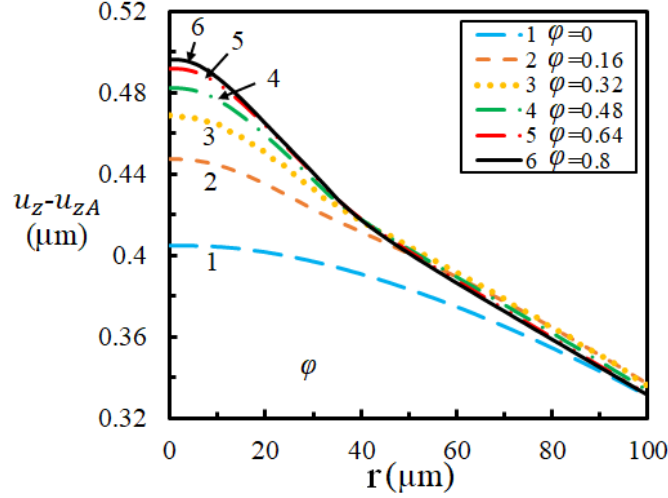


Figure 9. Relative z -displacement of the points of the contact surface with respect to the point C in Figure 1a with increasing anvil rotation, i.e. evolution of the deformed profile of the diamond-sample contact surface.

As mentioned, although diamond is very rigid (the Young's modulus of diamond is 1045.5 GPa, which is 11.5 and 9.2 times larger than those of the α and ω phases, respectively) and the maximum normal stress is below 4 GPa, because the contact surface of the diamond with the sample is long compared to the final thickness of the sample, the bending of a diamond anvil cannot be neglected. Figure 9 shows the evolution of the deformed profile of the diamond-sample contact surface.

The maximum deformation of an anvil along the symmetry axis reaches $0.4 \mu\text{m}$ after compression before torsion and increases from 0.4 to $0.5 \mu\text{m}$ during torsion due to redistribution of the contact stresses. As the contact normal stress becomes larger at the center of the sample (see Figure 2) and slightly smaller at the periphery, the evolution of the deformation of the anvil repeats this trend. Moreover, there is a change in the pressure gradient at the broad interface between transformed and non-transformed regions (see Figure 3), which coincides with a slight change in the slope of the diamond contact surface profile at this point. The final thickness of the sample at the center-line for a rotation angle of 0.8 and applied $\sigma_n = 27.6 \text{ MPa}$ is around $12.6 \mu\text{m}$, and Figure 9a gives the thickness of the sample at the periphery ($r=100$) $0.32 \mu\text{m}$ ($2 \times 0.16 \mu\text{m}$), or 2.5% smaller.

The variation of the sample thickness h at the symmetry axis ($r=0$) and the maximum dimensionless pressure p_{\max}/σ_{y1} in the sample during rotation is shown in Figure 10. Under compression, the sample thickness reduces to $28.61 \mu\text{m}$. The slope of the thickness reduction is large at the initial stage of rotation and decreases as the rotation angle increases. This is qualitatively consistent with the analytical solution for torsion under a fixed load without PT [10,13]. In addition, because the yield strength increases during PT, this also suppresses thickness reduction. Figure 10 also shows that, during torsion, the maximum pressure increases due to the increase in the yield strength and friction stress during PTs. Note that without PT, the pressure distribution does not change during torsion, which has been obtained analytically [10,13], numerically, [49] and experimentally [8,11].

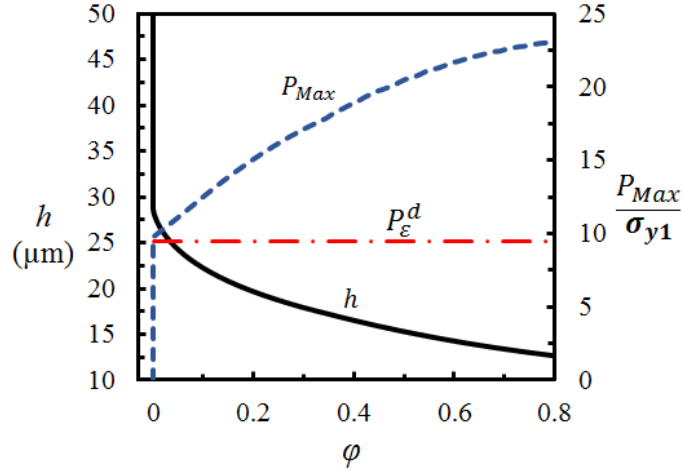


Figure 10. The variations of the sample thickness h and the dimensionless maximum pressure p_{\max}/σ_{y1} in the sample during torsion under applied constant normal stress $\sigma_n = 27.6$ MPa.

Concluding Remarks

The main problem in studying the PTs during HPT with metallic anvils for all materials with RDAC for most materials including Zr is that the only available information is the averaged pressure (force per total initial area) and number of turns for initiation of $\alpha \rightarrow \omega$ and $\alpha \rightarrow \beta$ PTs. That means that the system is considered as a black box. At the same time, the fields of pressure, plastic strain, and volume fraction of phases in the Zr sample during HPT, which are required for understanding actual physical, thermodynamic, and kinetic processes of interaction between PT and plasticity, are unknown.

In this paper, $\alpha \rightarrow \omega$ PT in Zr coupled to plastic flow under a fixed applied compressive force and torsion-induced large plastic shear strains in the RDAC are investigated by using FEM. Under the compression with the normal applied stress $\sigma_n = 27.6$ MPa (corresponding to the averaged pressure in a sample of 0.784 GPa), the sample thickness reduces by 44%. PT starts in

the region near the symmetry plane in the center of the sample, where the maximum pressure exists. The maximum plastic strain is localized at the contact surface at the periphery due to a large shear deformation, but PT cannot occur there because the pressure is lower than the minimum pressure for strain-induced PT, p_{ε}^d . During the rotation of an anvil at fixed force, the radial shear (and twisting) stress increases at the center of a sample due to a stronger ω phase and corresponding to material hardening of the $\alpha + \omega$ phase mixture during PT, and the sample thickness reduces due to the material radial flow. This leads to a drastic increase in the pressure gradient and pressure at the center of sample. In this manner, we reproduced the pressure self-multiplication effect observed experimentally for other materials [8,9,11] with the stronger high-pressure phase. Thus, our prediction of this effect for $\alpha \rightarrow \omega$ PT in Zr is conceptually justified. With an increasing rotation angle, PT propagates from the center toward the periphery. In the major region, except at the center of a sample, the total contact friction stress τ is equal to the yield strength in shear, which means that the plastic sliding is allowed. Relative slip between the sample and the diamond increases, and the pace of thickness reduction decreases during rotation. Due to the radial material flow, the ω phase can be observed in the region where pressure is lower than the minimum pressure for strain-induced PT, p_{ε}^d , which may lead to misinterpretation of the experimental data for determination of the minimum PT pressure. Because the axial load is fixed, the region at the center of a sample with $p > p_{\varepsilon}^d$ does not essentially grow, imposing a limitation on the maximum mass of transformed material. Further increase in rotation is not effective because while there is some small increase in the amount of transformed material in the region with $p > p_{\varepsilon}^d$, thickness of this region reduces and reverse PT in the region with $p < p_{\varepsilon}^d$ is

possible. To obtain a larger transformed region, a larger normal stress must be applied to increase the region with $p > p_{\varepsilon}^d$.

Although diamond is a very rigid material and the pressure is low, deformation of the diamond is not fully negligible due to its relatively large radial dimension. Thus, for a rotation angle of 0.8 and applied $\sigma_n = 27.6$ MPa, the thickness of the sample at the center is 12.6 μm , and at the periphery (for $r=100$) it is 0.32 μm , or 2.5% smaller. This, in turn, affects the pressure distribution.

By comparison between the process with rotation and without rotation of an anvil, we find that the volume fraction of the ω phase is very small at the small normal applied load, but after torsion at the same load (i.e. the averaged pressure), a large transformed zone and volume fraction of the ω phase can be obtained. If an increase in the volume fraction of the ω phase in DAC is desired, the only way to produce plastic straining is to increase the applied load σ_n , which leads to higher pressure in both diamond and sample, in comparison to PT in the RDAC. This is the main reason for reporting the experimental PT pressure difference with and without torsion, e.g. in [32,33]. We would like to stress that the physics, mechanics, and kinetics of PT in DAC and RDAC are identical because we use the same equations and the same minimum PT pressure p_{ε}^d . The difference is in the behavior of the system sample-loading device, which results in different pressure-accumulated plastic strain trajectories.

It is evident (e.g. from Figure 3) that the PT process in RDAC, despite the potential advantage in comparison with DAC, is far from optimal. Thus, due to the much stronger high-pressure phase and pressure self-multiplication effect, the pressure in the transformed region is much higher than the minimum PT pressure p_{ε}^d . Such a high pressure is not required for PT but

could not be avoided. The region in which PT occurs is limited by the condition $p > p_{\varepsilon}^d$ and cannot be increased by increasing the shear under a fixed force. A significant reduction in thickness during torsion also reduces the total mass of the high-pressure phase. A way to overcome these drawbacks is to place the sample within a strong gasket, optimize the geometric parameters of the gasket, and achieve nearly-homogeneous pressure distribution within the sample, which does not vary essentially during torsion and PT. This was achieved in experiments for PT from hexagonal to superhard wurtzitic boron nitride (based on a simplified analytical optimization) [7] and in FEM simulations in [23].

Similar to the PT under compression in DAC [26], obtained results for torsion in RDAC demonstrate that PT cannot be characterized by the averaged pressure, which is traditional in HPT. During torsion at the fixed averaged pressure, the maximum pressure grows from 1.8 GPa to 4.0 GPa (Figure 10), i.e. by a factor of 2.2. This is slightly larger than a factor of 2, which was estimated in [26]. Further torsion leading to completion of PT at the center of a sample should lead to further increase in the maximum pressure. While the geometry of a sample in RDAC differs from that in the high-pressure torsion, some qualitative conclusions should be the same. Thus, under compression, the minimum pressure for the strain-induced PT $p_{\varepsilon}^d = 1.7$ GPa is reached at the averaged pressure of 0.784 GPa, which is 2.2 times lower. It is lower than the upper bound of 3, estimated in [26], due to the effect of the part of the sample outside of the flat anvil surface, which is absent in the high-pressure torsion. This multiplier was used in [26] to correct the magnitude of p_{ε}^d pressure for $\alpha \rightarrow \omega$ PT based on the averaged pressure in [32,33]. The maximum pressure after torsion exceeds an averaged pressure of 0.784 GPa by a factor of 5. This factor should be used to correct the minimum pressure p_{ε}^d for $\alpha \rightarrow \beta$ PT based on the averaged pressure in [32,33]. Also, strong heterogeneity in all fields and difference in geometric

conditions (which are very seldom specified), is one of the important sources of explanation of the strong scatter in transformation pressures for $\alpha \rightarrow \omega$ PT in Zr in [27-37].

The results obtained in this paper enhance understanding of the complex conditions under which strain-induced PT in the Zr sample occurs in the RDAC. They will be beneficial for the design of experiments and extraction of material parameters, as well as optimization and control of PTs by varying the geometry and loading conditions.

Acknowledgements

The support of ARO (W911NF-17-1-0225), NSF (DMR-1434613), ONR (N00014-16-1-2079), and Iowa State University (Vance Coffman Faculty Chair Professorship) is gratefully acknowledged.

Data Availability

The raw/processed data required to reproduce these findings cannot be shared at this time as the data also forms part of an ongoing study.

References

- [1] P.C. Burnley, H.W. Green, Stress Dependence of the Mechanism of the Olivine–Spinel Transformation, *Nature*, 338 (1989) 753–756.
- [2] S.H. Kirby, Localized Polymorphic Phase Transformations in High-Pressure Faults and Applications to the Physical Mechanism of Deep Earthquakes, *Journal of Geophysics Research*, 92 (B13) (1978) 13789.
- [3] T.C. Wu, W.A. Basset, P.C. Burnley, M.S. Weathers, Shear-promoted phase transitions in Fe_2SiO_4 and Mg_2SiO_4 and the mechanism of deep earthquakes. *Journal of Geophysics Research*, 98 (1993) 19767-19776.
- [4] V.I. Levitas, Y. Ma, E. Selvi, J. Wu, J.A. Patten, High-density amorphous phase of silicon carbide obtained under large plastic shear and high pressure, *Physical Review B*, 85 (2012) 054114.

- [5] C. Ji, V.I. Levitas, H. Zhu, J. Chaudhuri, A. Marathe, Y. Ma, Shear-Induced Phase Transition of Nanocrystalline Hexagonal Boron Nitride to Wurtzitic Structure at Room Temperature and Lower Pressure, *Proceedings of the National Academy of Sciences*, 109 (2012) 19108-19112.
- [6] Y. Ma, E. Selvi, V.I. Levitas, J. Hashemi, Effect of Shear Strain on the α - ϵ Phase Transition of Iron: A New Approach in the Rotational Diamond Anvil Cell, *Journal of Physics: Condensed Matter*, 18 (2006) S1075.
- [7] V.I. Levitas, Y. Ma, J. Hashemi, M. Holtz, N. Guven, Strain-Induced Disorder, Phase Transformations, and Transformation-Induced Plasticity in Hexagonal Boron Nitride Under Compression and Shear in a Rotational Diamond Anvil Cell: In Situ X-Ray Diffraction Study and Modeling, *Journal of Chemical Physics*, 125 (2006) 044507.
- [8] V.D. Blank, E.I. Estrin, *Phase Transitions in Solids under High Pressure*, New York : CRC Press, 2014.
- [9] V.D. Blank, Y.Y. Boguslavsky, M.I. Eremets, E.S. Itskevich, Y.S. Konyaev, A.M. Shirokov, E.I. Estrin, Pressure Self-Multiplication Effect on Phase-Transition under Quasi-Hydrostatic Conditions, *Zhurnal Eksperimental'noi i Teoreticheskoi Fiziki* (ISSN 0044-4510), In Russian, 87 (1984) 922-926.
- [10] V.I. Levitas, High-pressure Mechanochemistry: Conceptual Multiscale Theory and Interpretation of Experiments, *Physical Review B*, 70 (2004) 184118.
- [11] N.V. Novikov, S.B. Polotnyak, L.K. Shvedov, V.I. Levitas, Regularities of Phase Transformations and Plastic Straining of Materials in Compression and Shear on Diamond Anvils: Experiments and Theory, *Journal of Superhard Materials*, 21 (1999) 39-51.
- [12] V.I. Levitas, L.K. Shvedov, Low-Pressure Phase Transformation from Rhombohedral to Cubic Bn: Experiment and Theory, *Physical Review B*, 65 (2002) 104109.
- [13] V.I. Levitas, Continuum mechanical fundamentals of mechanochemistry in High-pressure surface science and engineering, Edited by Y. Gogotsi and V. Domnich, Institute of Physics Publishing, 2004.
- [14] V. Blank, M. Popov, S. Buga, V. Davydov, A.N. Ivlev, B.N. Mavrin, R. Ceolin, H. Szwarc, A. Rassat, Is C60 Fullerite Harder than Diamond?, *Physics Letters A*, 188 (1994) 281-286.
- [15] V.I. Levitas, M. Javanbakht, Phase Transformations in Nanograin Materials under High Pressure and Plastic Shear: Nanoscale Mechanisms, *Nanoscale*, 6 (2014) 162-166.
- [16] M. Javanbakht, V.I. Levitas, Nanoscale Mechanisms for High-Pressure Mechanochemistry: A Phase Field Study, *Journal of Materials Science*, (2018) <https://doi.org/10.1007/s10853-018-2175-x>.

- [17] V.I. Levitas, Phase Transformations under High Pressure and Large Plastic Deformations: Multiscale Theory and Interpretation of Experiments, Proceedings of the International Conference on Martensitic Transformations: Chicago (ICOMAT) 2017.
- [18] B. Feng, V.I. Levitas, Y. Ma, Strain-Induced Phase Transformation under Compression in a Diamond Anvil Cell: Simulations of a Sample and Gasket, *Journal of Applied Physics*, 115 (2014) 163509.
- [19] B. Feng, V.I. Levitas, O.M. Zarechnyy, Plastic Flows and Phase Transformations in Materials under Compression in Diamond Anvil Cell: Effect of Contact Sliding, *Journal of Applied Physics*, 114 (2013) 043506.
- [20] B. Feng, O.M. Zarechnyy, V.I. Levitas, Strain-Induced Phase Transformations under Compression, Unloading, and Reloading in a Diamond Anvil Cell, *Journal of Applied Physics*, 113 (2013) 173514.
- [21] V.I. Levitas, O.M. Zarechnyy, Modeling and Simulation of Strain-Induced Phase Transformations under Compression in a Diamond Anvil Cell, *Physical Review B*, 82 (2010) 174123.
- [22] B. Feng, V.I. Levitas, Coupled Phase Transformations and Plastic Flows under Torsion at High Pressure in Rotational Diamond Anvil Cell: Effect of Contact Sliding, *Journal of Applied Physics*, 114 (2013) 213514.
- [23] B. Feng, V.I. Levitas, Effects of Gasket on Coupled Plastic Flow and Strain-Induced Phase Transformations under High Pressure and Large Torsion in a Rotational Diamond Anvil Cell, *Journal of Applied Physics*, 119 (2016) 015902.
- [24] B. Feng, V.I. Levitas, O.M. Zarechnyy, Strain-Induced Phase Transformations under High Pressure and Large Shear in a Rotational Diamond Anvil Cell: Simulation of Loading, Unloading, and Reloading, *Computational Materials Science*, 84 (2014) 404-416.
- [25] V.I. Levitas, O.M. Zarechnyy, Modeling and Simulation of Strain-Induced Phase Transformations under Compression and Torsion in a Rotational Diamond Anvil Cell, *Physical Review B*, 82 (2010) 174124.
- [26] B. Feng, V.I. Levitas, Plastic Flows and Strain-Induced Alpha to Omega Phase Transformation in Zirconium during Compression in a Diamond Anvil Cell: Finite Element Simulations, *Materials Science and Engineering: A*, 680 (2017) 130-140.
- [27] A. Jayaraman, W. Klement, and G.C. Kennedy, Melting and Polymorphism at High Pressures in Some Group IV Elements and III-V Compounds with the Diamond/Zincblende Structure, *Physical Review*, 130 (1962) 540.
- [28] V. A. Zilbershtein, G. I. Nosova, E. I. Estrin, Alpha--omega transformation in titanium and zirconium, *Fizika Metallov I Metallovedenie* 35 (1973) 584-589.

- [29] V. A. Zilbershtein, N. P. Chistotina, A. A. Zharov, N. S. Grishina, E. I. Estrin, Alpha-omega transformation in titanium and zirconium during shear deformation under pressure, *Fizika Metallov I Metallovedenie* 39 (1975) 445-447.
- [30] S.K. Sikka, Y.K. Vohra, R., Chidambaram, Omega Phase in Materials, *Progress in Materials Science*, 27 (1982) 245-310.
- [31] H. Xia, S.J. Duclos, A.L. Ruoff, Y.K. Vohra, New High-Pressure Phase Transition in Zirconium Metal, *Physical Review Letters*, 64 (1991) 204-207.
- [32] B. Srinivasarao, A.P. Zhilyaev, M.T. Perez-Prado, Orientation Dependency of the Alpha to Omega Plus Beta Transformation in Commercially Pure Zirconium by High-Pressure Torsion, *Scripta Materialia*, 65 (2011) 241-244.
- [33] A.P. Zhilyaev, I. Sabirov, G. Gonzalez-Doncel, J. Molina-Aldareguia, B. Srinivasarao, M.T. Perez-Prado, Effect of Nb Additions on the Microstructure, Thermal Stability and Mechanical Behavior of High Pressure Zr Phases under Ambient Conditions, *Materials Science and Engineering: A*, 528 (2011) 3496-3505.
- [34] B. Olinger, J. C. Jamieson, Zirconium: Phases and Compressibility to 120 Kilobars, *High Temperatures High pressures*, 5 (1973) 123-131.
- [35] J.C. Jamieson, Crystal Structures of Titanium, Zirconium, and Hafnium at High Pressures, *Science*, 140 (1963) 72-3.
- [36] K. Edalati, Z. Horita, S. Yagi, E. Matsubara, Allotropic phase transformation of pure zirconium by high-pressure torsion, *Materials Science and Engineering: A*, 523 (2009) 277–281.
- [37] A.P. Zhilyaev, F. Gálvez, A. Sharafutdinov, M.T. Pérez-Prado, Influence of the high pressure torsion die geometry on the allotropic phase transformations in pure Zr, *Materials Science and Engineering: A*, 527 (2010) 3918–3928.
- [38] M.T. Pérez-Prado, A.P. Zhilyaev, First Experimental Observation of Shear Induced hcp to bcc Transformation in Pure Zr, *Physical Review Letters*, 102 (2009) 175504.
- [39] K. Edalati, Z. Horita, A review on high-pressure torsion (HPT) from 1935 to 1988, *Materials Science and Engineering: A*, 652 (2016) 325–352.
- [40] M. Kamrani, V.I. Levitas, B. Feng, FEM simulation of large deformation of copper in the quasi-constrain high-pressure-torsion setup, *Mater. Sci. Eng. A* 705 (2017) 219–230.
- [41] R.J. Hemley, H.K. Mao, G.Y. Shen, J. Badro, P. Gillet, M. Hanfland, D. Hausermann, X-ray Imaging of Stress and Strain of Diamond, Iron, and Tungsten at Megabar Pressures, *Science*, 276 (1997) 1242-1245.

- [42] V.I. Levitas, Large Deformation of Materials with Complex Rheological Properties at Normal and High Pressure. New York: Nova Science, 1996.
- [43] ABAQUS V6.11. Providence RI, USA: ABAQUS INC, 2011.
- [44] S.Q. Wang, H.Q. Ye, First-Principles Study on the Lonsdaleite Phases Of C, Si and Ge, Journal of Physics Condensed Matter, 15 (2003) L197-L202.
- [45] E. Guler, M. Guler, Elastic and Mechanical Properties of Cubic Diamond under Pressure, Chinese Journal of Physics, 53 (2015) 040807-1-11.
- [46] B.T. Wang, P. Zhang, H.Y. Liu, W.D. Li, P. Zhang, First-Principles Calculations of Phase Transition, Elastic Modulus, and Superconductivity under Pressure for Zirconium, Journal of Applied Physics, 109 (2011) 063514.
- [47] Y.S. Zhao, J.Z. Zhang, Enhancement of Yield Strength in Zirconium Metal through High-Pressure Induced Structural Phase Transition, Applied Physics Letters, 91 (2007) 201907.
- [48] C.W. Greeff, Phase Changes and the Equation of State of Zr, Modelling and Simulation in Materials Science and Engineering, 13 (2005) 1015-1027.
- [49] V.I. Levitas, O.M. Zarechnyy, Numerical Study of Stress and Plastic Strain Evolution under Compression and Shear of a Sample in a Rotational Anvil Cell, High Pressure Research, 30 (2010) 653-669.

CHAPTER 4. TENSORIAL STRESS-STRAIN FIELDS, LARGE ELASTOPLASTICITY, AND FRICTION IN DIAMOND ANVIL CELL UP TO 400 GPA

This Section reproduces paper Levitas V.I., Kamrani M., and Feng B., Tensorial stress-strain fields and large elastoplasticity as well as friction in diamond anvil cell up to 400 GPa., npj Computational Materials 5, 94 (2019).

Abstract

Various phenomena (fracture, phase transformations, and chemical reactions) studied under extreme pressures in diamond anvil cell (DAC) are strongly affected by fields of all components of stress and plastic strain tensors. However, they could not be measured. We suggest a coupled experimental-theoretical-computational approach that allowed us to refine, calibrate, and verify models for elastoplastic behavior and contact friction for tungsten (W) and diamond up to 400 GPa and reconstruct fields of all components of stress and large plastic strain tensors in W and diamond. Despite the generally accepted strain-induced anisotropy, strain hardening, and path-dependent plasticity, W after large plastic strains behaves as isotropic and perfectly plastic with path-independent surface of perfect plasticity. Scale-independence of elastoplastic properties is found even for such large field gradients. Obtained results open opportunities for quantitative extreme stress science and reaching record high pressures.

Introduction

In static high pressure research, megabar pressures are generated by compression of a thin sample by two diamonds in diamond anvil cells (DAC) [1-4]; see Figure 1. This process is accompanied by large plastic deformation of a sample and large elastic deformation of the diamond [5,6]. Various problems, such as the study of physical, chemical, geological, and mechanical phenomena and synthesis of new phases in a sample, as well as the increasing range of achievable pressures [1-23], are related to knowledge of the fields of all components of the stress, elastic, and plastic strain tensors in DAC. While most measurements and discussions are related to pressure only, it is evident that elastic deformation and fracture of diamond and plastic flow of a sample and gasket depend on all components of the stress tensor. Contact friction between diamond and sample/gasket plays a key role in generating high pressure without fracture of the diamond; friction is a shear stress that depends on the stress normal to the contact surface. It is also well-known that phase transformations and chemical reactions in solids depend not only on pressure, but also on the deviatoric stresses and plastic strains [12, 14-16, 20-23]. All of these fields are extremely complex and heterogeneous, e.g. with normal stresses varying by megabar over 20 μm [6,7].

Measurement of the radial pressure distribution at the sample-diamond boundary was based on the ruby fluorescence method, which worked up to 185 GPa [4]. For higher pressure, radial pressure distribution averaged over the sample thickness is determined using X-ray diffraction in a sample [6,7]. The radial thickness profile, which characterizes both elastic deformation of an anvil and elastoplastic deformation of a sample/gasket, was measured utilizing *in-situ* high-pressure X-ray absorption [6,7]. Measurement of the deviatoric stress was limited to the difference between axial stresses σ_{zz} and radial stresses σ_{rr} averaged over the entire sample

[8,9,17-19]. Plastic deformation fields in the sample compressed in DAC and contact friction stresses were not measured at all. Thus, despite significant progress, it is unlikely that all tensorial fields in DAC will be measured. Theoretical approaches and finite element method (FEM) simulations [23-29] of the DAC are based on relatively simple models with linear pressure dependence of the yield strength and simplified contact friction conditions. The most sophisticated model and the best numerical reproduction of the experimental pressure distribution in ref. [5] was obtained in ref. [27] for compression of rhenium up to 285 GPa. To obtain such a description of the experiment, the third-order elastic constants of diamond were modified. Also, good correspondence was obtained for one pressure distribution only; for two smaller pressure levels, significant deviation from the experiment existed, i.e. the model is not adequate.

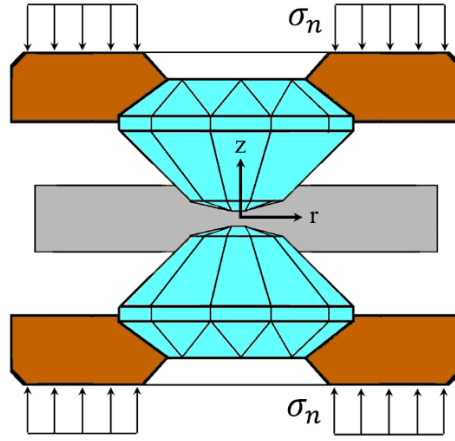


Figure 1. DAC scheme: Two diamond anvils compress a sample.

We suggest the following coupled experimental-theoretical-computational approach for determination of all stress and plastic strain tensorial fields, elastoplastic properties, and contact friction rules. All fields which can be measured should be measured. Physics-based models for elastoplastic behavior and contact friction should be iteratively developed and refined, and all

material properties should be calibrated by fitting to some experimental fields and verified by comparison with other experimental fields. With these properties, simulations provide all fields, including components of the stress and plastic strain tensors, friction stress, etc., i.e. those which cannot be directly measured. To obtain the first results from this method, we will use the most advanced experimental data on compression of W in DAC up to 400 GPa [6] and generalize our models for large elastoplastic deformations and contact friction from [24-27].

Model

A complete system of equations for fourth-order elasticity of diamond, large elastoplastic deformation of W, combined Coulomb and plastic friction, geometry of DAC, formulation of axisymmetric problem in cylindrical coordinates $rz\theta$, and nonlinear elastic properties are presented in Supplementary material. It is known that the yield surface in the six-dimensional space of components of the stress tensor evolves during plastic deformation (Supplementary Figure 3), exhibiting strain hardening; this evolution depends on the entire history of plastic strain, and material acquired deformation-induced anisotropy [24,30]. It was suggested in [24] as the postulate of the perfect plasticity that, above some level of accumulated plastic strain $q > m$ and for a deformation path without sharp changes in directions (monotonous deformation), the initially-isotropic polycrystalline materials are deformed as perfectly plastic and isotropic with a strain-history-independent surface of the perfect plasticity (Figure 13). This statement means that (1) the strain hardening is saturated, and that (2) strain-induced anisotropy and path dependence do not exhibit themselves at monotonous loading. Some qualitative arguments in favor of the postulate of the perfect plasticity have been analyzed [24], but quantitative proof was not given for any material. Here, we incorporated this postulate into our model and will prove that such a model describes well experimental data. Our model is based on the linear pressure-dependence

of the yield strength in compression $\sigma_y = \sigma_{0y} + ap$ with two material parameters, with no plastic strain or plastic strain path dependence. Another hypothesis which will be proven is that despite the μm -sized sample thickness and huge stress and plastic strain gradients, i.e. conditions that require utilization of scale-dependence and the gradient plasticity [31-33], much simpler local plasticity provides adequate description of experiments.

Contact friction stress is determined either by the Coulomb law $\tau_f = \mu(\sigma_c)\sigma_c$, where σ_c is the normal contact stress and μ is the friction coefficient, or by the yield strength in shear $\tau_f = \tau_y(p) = \sigma_y(p)/\sqrt{3}$ (plastic friction), whichever is smaller. Sticking occurs if the contact shear stress is smaller than these critical values τ_f . All of our assumptions for the yield strength (independence of plastic strain and its path) are also involved in the assumption for plastic friction. The friction coefficient is usually taken as a constant because no experimental data under high pressure is available. We assume $\mu = \mu_0 + c\sigma_c$ with two material parameters.

In addition, some of the third-order elastic constants of W and forth-order elastic constants of diamond, which are not well defined from the literature, are refined by comparison with DAC pressure and sample thickness distributions.

To summarize, in comparison with ref. [27], current model includes fourth-order elasticity of diamond, combined Coulomb and plastic contact sliding, and linear pressure-dependence of the Coulomb friction coefficient. Moreover, all unknown material parameters are calibrated using one set of experimental data and verified using another experimental set.

Results

All four material parameters in the pressure dependence of the yield strength and friction coefficient were calibrated by minimizing the error between experimental and FEM results for

pressure distributions for *two curves* with maximum pressures $p_{\max} = 170$ and 240 GPa (Figure 2a). This led to

$$\sigma_y = 1.8 + 0.1p; \quad p \leq 225 \text{ GPa}; \quad \mu = 0.05 + 0.001\sigma_c; \quad \sigma_c \leq 37 \text{ GPa}. \quad (1)$$

Unexpected strong limitations on pressure and contact stress appear because we found in FEM solutions that Coulomb sliding and plastic flow do not occur for $\sigma_c > 37$ GPa and $p > 225$ GPa, respectively. With properties in Eq. 1, good correspondence is obtained for *two* other pressure distributions with $p_{\max} = 300$ and 400 GPa, with a maximum difference not exceeding 10% (Figure 2a). In addition, the profile of the sample after very large compression and deformed anvil surface were reproduced for all *four* pressures, with a maximum discrepancy smaller than 1 micron (Figure 2b and c). Both discrepancies are within error for an experiment under such extreme conditions. The curves in Figure 2 are nontrivial, and coincidence demonstrates strong verification of the entire model and the specific material properties from Eq. (1). It also proves the *validity of the postulate of the perfect plasticity* for W, which was directly incorporated in our model, and *sufficiency of the local elastoplastic model* even at micron scale and with huge stress and plastic strain gradients. In summary, *elastoplasticity and, consequently, plastic friction under such large strain and pressure is plastic strain-, plastic strain path-, and scale-independent*, which drastically simplifies theory and measurements.

In addition, the higher-order elastic constants of W and diamond, which have large scatter in literature (see Supplementary material), have been also refined/identified. Thus, we found the third-order constants for W, $m = -1,081$ and $n = -1,164$ GPa, to obtain a slightly better fit to the experimental pressure distribution curves for three lowest pressure. The forth-order elastic constant of diamond, $C_{1112} = 31214$, $C_{1122} = 20044$, and $C_{1266} = 819$ GPa, were

found from the best fit to the sample profile under highest pressure only under constrain that they satisfy the known equation of state of diamond, see Supplementary material.

The suggested method has high throughput features, which allows to determine 10 material parameters using three pressure and one sample thickness distributions.

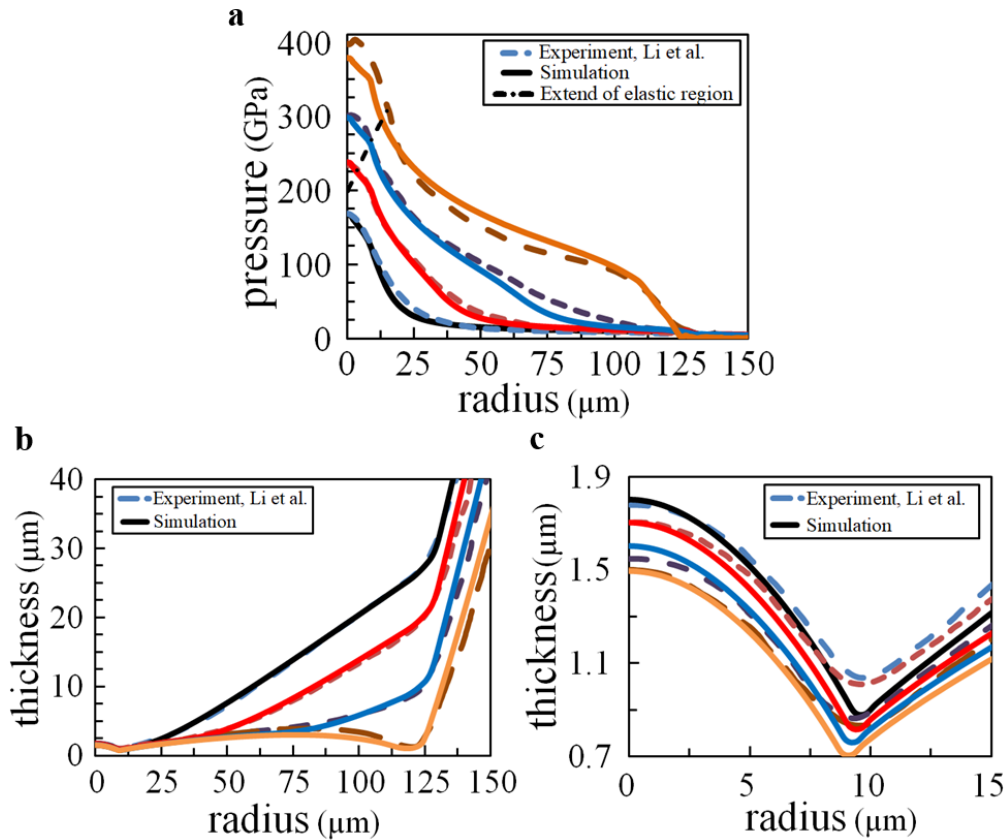


Figure 2. Calibration and verification of the model for DAC. a) Radial distributions of pressure. b) Corresponding sample thickness (anvil profile) in experiment [6] (dash lines) and FEM simulations (solid lines). c) Zoomed sample thickness profile from b at the central region of the sample. Dash-dot line in a shows the radius of the central region where the sample deforms elastically after initial plastic flow. Material functions in equation (1) were determined from the best fit to two low-pressure curves in a. Good correspondence with experiments for two high-pressure curves in a and all four thickness curves after very large compressions in b and c provides strong and nontrivial verification of the model.

Known [5] pressure-dependence of the yield strength for W has huge scatter (Figure 3), which is related to numerous assumptions for the determination of $\sigma_y(p)$ and to attribution of the dependence of σ_y on plastic strain to the pressure dependency. In our curve, the effect of plastic stain is excluded and the correctness of Eq. (1) is confirmed by numerous data in Figure 2.

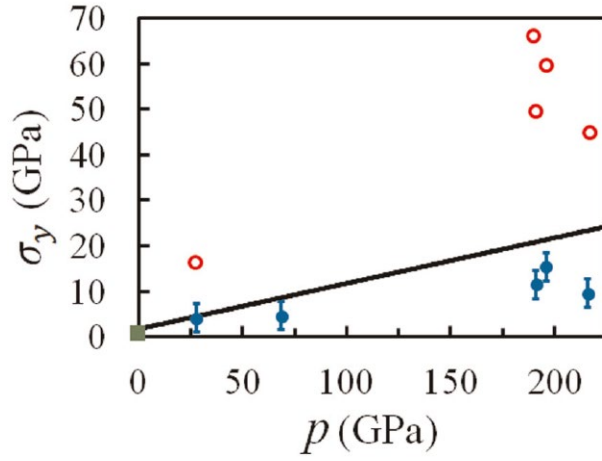


Figure 3. Pressure dependence of the yield strength after large plastic deformation. Solid line is based on equation (1); symbols are from ref. [5].

After proving its validity, the model is used for computational reconstruction of all fields of interest. Distribution of shear friction stress and normalized radial sample velocity along the diamond-sample contact surface at different pressures is shown in Figures 4a and b. Such a complex profile of shear stresses and their evolution are nontrivial and counterintuitive. In particular, shear stress in the sticking zone makes several oscillations in a central cup region, and the sticking zone grows with increasing compression. The plastic friction zone is surprisingly narrow, which does not allow use of the traditional method for determination of $\tau_y(p)$ based on a pressure gradient [7,13,24]. The maximum yield strength in shear and corresponding p in the

plastic sliding zone *reduce* from 5.85 GPa and 77.2 GPa for $p_{\max} = 164$ GPa to 3.7 GPa and 44 GPa for $p_{\max} = 380$ GPa. The maximum shear stress in the Coulomb sliding zone is 3.21 GPa, corresponding to $\sigma_c = 37$ GPa; for $p_{\max} = 380$ GPa, it is 2 GPa, corresponding to $\sigma_c = 26.2$ GPa. An important conclusion is that, due to significant increase in the sticking zone, an increase in p_{\max} does not lead to an increase in the maximum range of σ_c and friction stress, either for Coulomb or plastic friction. The only way to increase these ranges is to use torsion under a fixed force in rotational DAC [12,15,22,34], for which FEM simulations [29,35] show that the sticking zone is localized near the center.

The sample particles' radial velocity along the diamond-sample contact surface (Figure 4b) is directed toward the center in the sticking zone for any pressure, and is equal, by the definition of sticking, to the velocity of the diamond contact particles. Outside the sticking zone, sample particles move away from the center, achieving maximum velocity at the edge of the culet. The maximum velocity increases to $p_{\max} = 231$ GPa, then reduces due to the increasing sticking zone.

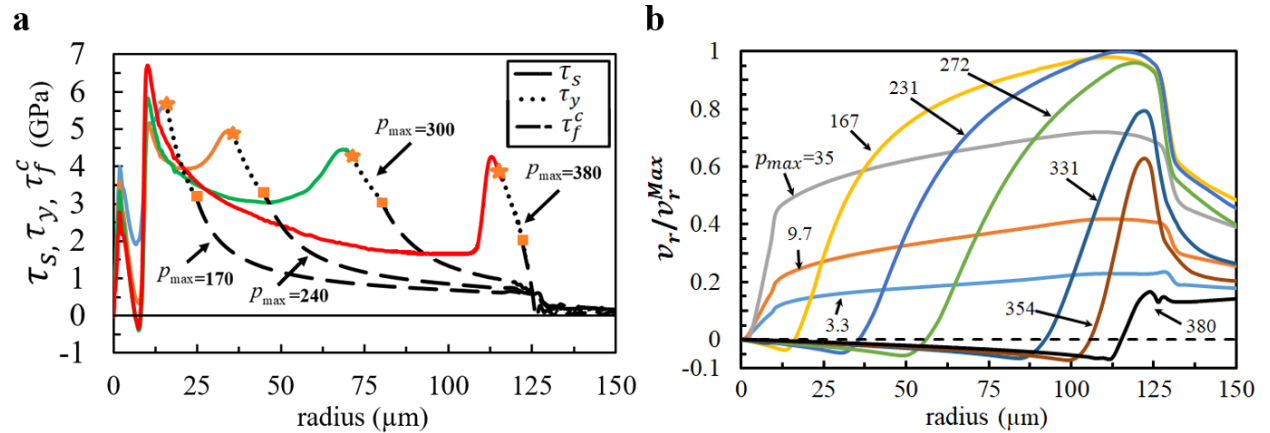


Figure 4. Contact friction and velocities. a) Distribution of shear friction stress and b) normalized sample radial velocity along the diamond-sample contact surface at various pressures. In **a**, along

each given curve, with reducing radius, i.e. from low to high pressure, the dashed portion corresponds to the Coulomb friction until shear stress reaches $\tau_y(p)$ (designated by squares). The dotted line between squares and stars corresponds to the plastic sliding with $\tau_c = \tau_y(p)$. The solid line between stars and center of the sample corresponds to sticking between anvil and sample. Numbers near curves in a and b designate maximum pressure. Velocity is normalized by maximum velocity at $p_{\max} = 231$ GPa.

All relevant fields in the central part of the W sample are presented in Figure 5 on a quarter of the sample, due to the symmetries. While axial stress σ_{zz} is independent of the z coordinate, radial stress σ_{rr} visibly depends on z and pressure p is, by definition, in between.

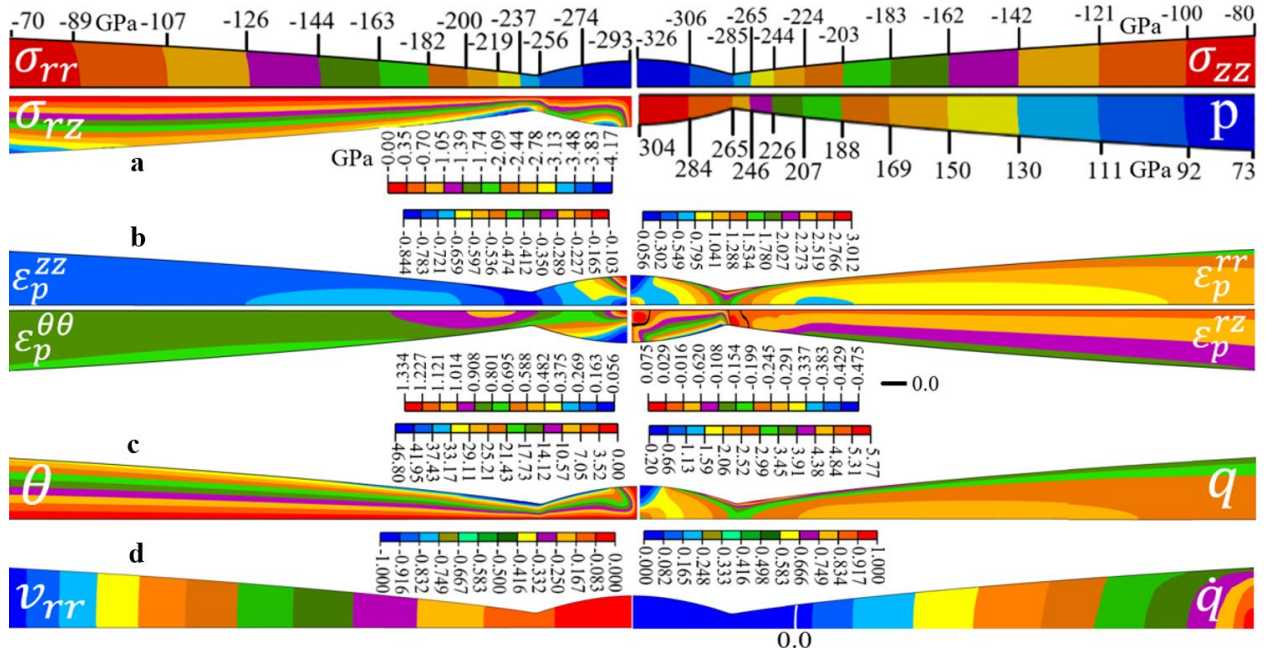


Figure 5. Stress, plastic strain, and rate fields for $p_{\max} = 300$ GPa. a) Fields of components of the stress tensor and pressure p , b) plastic strain tensor ϵ_p , c) accumulated plastic strain q , and

particles' rotation angle θ , and d) normalized radial velocity v_{rr} and \dot{q} in the central part of a sample for $r < 60 \mu\text{m}$. See supplementary material for definition of parameters. Scale of the thickness vs. length is multiplied by four.

All components of plastic strain and q are very heterogeneous and reach very large values. Shear strain ε_p^{rz} changes sign three times in the central zone. Accumulated plastic strain q reaches its maximum value at the contact surface, especially where the thickness is smallest. Note that, for uniaxial compression/tension, q reduces to the logarithmic strain, and maximum $q=5.77$ in Figure 5c corresponds to the ratio of the initial-to-final length of $\exp(5.77)=321$. With increasing radius, q increases further. Material rotation in Figure 5c, which leads to the development of texture, is also very large, with a maximum of 46.8° in this region. Thus, if strain-induced anisotropy would be present, isotropic flow theory would not describe experiments. The rotation angle, similar to shear stress σ_{rz} , is zero at the symmetry axis and plane and increases with increasing r and z . Radial velocity (Figure 5d) at such a pressure is directed toward the center in the entire region. It is independent of z and its magnitude increases with r . The rate of accumulated plastic strain \dot{q} also increases with r , with zero region to the left of the white line in Figure 5d, where plastic flow stops and the material deforms elastically. Evolution of the elastic zone with increasing pressure is shown in Figure 2a. It appears at $p_{\max} = 200 \text{ GPa}$ and increases with increasing pressure due to cupping of diamond.

All stress fields in the central part of the diamond for $p_{\max} = 300 \text{ GPa}$ are presented in Figure 6.

All normal stresses have their maximum at the center of the culet, with $\sigma_{zz}^{\max} = -321 \text{ GPa}$ and

$\sigma_{rr}^{\max} = \sigma_{\theta\theta}^{\max} = -260 \text{ GPa}$, i.e. nonhydrostaticity is very high. Maximum shear stress $\sigma_{rz}^{\max} = 37.5$

GPa is located away from the culet. This value is significantly smaller than the theoretical shear strength of 96.6 GPa at zero pressure, which grows with pressure [36]. It is important that the regions in which maximum normal and shear stresses occur do not overlap.

The obtained fields of all components of the stress tensor are the basis for the development of criteria for fracture of diamond. To illustrate the concept, consider experimentally observed fracture due to compression stress $\sigma^{[110]}$ along the $[110]$ direction. Theoretical strength for compression along the $[110]$ direction obtained in ref. [37] using ab initio simulations can be approximated as $\sigma_{th}^{[110]} = -471 + 1.64\sigma_{bi}$ (GPa), where σ_{bi} is the averaged biaxial normal stress in planes orthogonal to (110) ; in our case $\sigma_{bi} = 0.5[\sigma^{[\bar{1}10]} + \sigma_{\theta\theta}]$, where $\sigma^{[\bar{1}10]}$ is normal stress along the $[\bar{1}10]$. The equivalent normalized stress in direction $[110]$, plotted in Figure 6, is then $\sigma_{eq}^{[110]} = \sigma^{[110]} / \sigma_{th}^{[110]}$, and fracture occurs at $\sigma_{eq}^{[110]} = 1$. Since maximum $\sigma_{eq}^{[110]} = 0.32$, there is still a significant safety factor for ideal diamond along the $[110]$ direction. For complete fracture analysis, similar distributions should be obtained for other possible fracture planes and shear stresses along these planes should be also taken into account. This is the key problem, the solution of which will allow optimization of the design of anvils and loading conditions for a perfect crystal, which will provide the upper bound of achievable pressure (stresses). Introducing defects into simulations will open the possibility of developing the fracture mechanics and plasticity of real diamond crystals under extreme stresses.

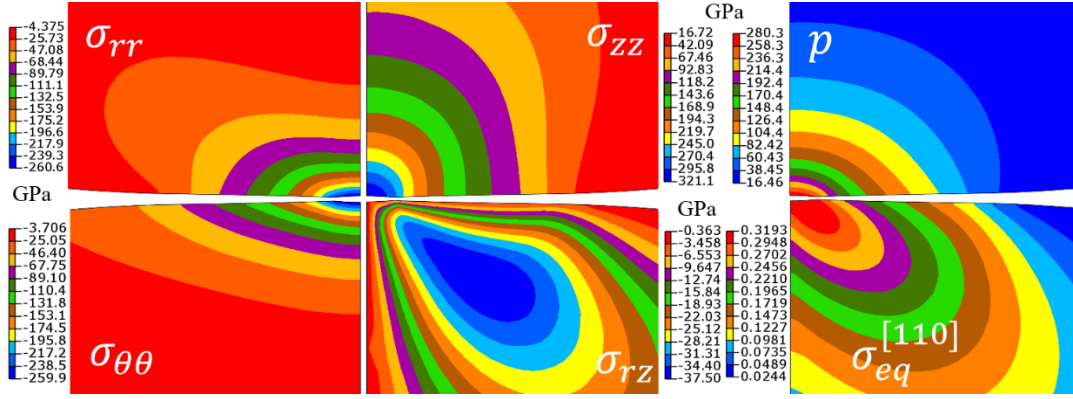


Figure 6. Field of the components of the stress tensor, pressure, and equivalent stress $\sigma_{eq}^{[110]}$ near the tip of a diamond anvil for $r < 100$ and $z < 70$ microns for $p_{\max} = 300$ GPa.

Concluding Remarks

In summary, we suggested a novel coupled experimental-theoretical-computational approach that allowed us to extract complete information about elastoplastic properties and friction rules, as well as all complex tensorial fields for materials compressed in a DAC under extreme pressure. In particular, we refined, calibrated, and verified models for elastoplastic behavior of a sample and contact friction for W up to 400 GPa and reconstruct fields of all components of stress and large plastic strain tensors in W and diamond. In addition to quantitative information on the pressure dependence of the yield strength and friction, as well as higher-order elastic constants, we justify some general unique properties of elastoplastic behavior under very large strains and pressures:

- (a) Despite the generally accepted strain-induced anisotropy, strain hardening, and path-dependent plasticity, W after large plastic strains behaves isotropically and does not exhibit strain hardening and path-independence.
- (b) Despite the μm -sized sample thickness and huge stress ($5 \text{ GPa}/\mu\text{m}$) and plastic strain gradients, scale-independence of elastoplastic properties is found.

Both of these properties drastically simplify plasticity theory and measurements under extreme conditions.

High precision allowed us to find that the pressure dependence of the yield strength is slightly concave, which challenges the well-accepted postulates of the plasticity theory. They should be generalized for extreme pressure.

Our finding for plasticity also implies important properties for plastic friction under such extreme loading: Plastic friction is plastic strain-, plastic strain path-, and scale-independent.

The field of all components of the stress tensor in diamond are the basis for the development of criteria for fracture of diamond. We illustrated the concept by considering fracture due to compression along one of the experimentally observed directions. This is an important step which will allow optimization of the design of anvils and loading conditions for further increase in achievable pressure.

Note that W is used as a gasket material in DAC at megabar pressures, i.e. obtained results have also applied importance for study of various sample materials within W gasket. Knowledge of the distributions of all (generally 12) components of stress and plastic strain tensors in a sample will allow study of their (instead of pressure alone) effect on phase transformations, chemical reactions [12,14-16,20-22,34-35], and various physical properties. In comparison with research under hydrostatic pressure, this will add up to 11 new dimensions to the parametric space for studying these processes, searching for new phases and materials, drastically reducing the required pressure for synthesis of new and known materials with unique properties, and understanding processes in the deep interiors of the Earth and other planets. Obtained results will also enable calibration and verification of known and new methods for measurement of the components of stress tensors in anvils and samples.

Methods

A complete system of equations for fourth-order elasticity of diamond, large elastoplastic deformation of W, and combined Coulomb and plastic friction, as well as problem formulation are presented in Supplementary material. Finite element algorithm presented in ref. 27 was utilized for solution of all boundary-value problems.

Geometry and Boundary Conditions

Axisymmetric problem formulation is considered. Due to symmetry of the Mao-type DACs used in ref. [1], only the upper part of the DAC and sample will be used in simulations. Geometry of the sample and the anvil, as well as the boundary conditions, are shown in Figure 11 and are as follows:

- (1) A uniform vertical displacement is applied at the boundary between the top inclined surface of the anvil and Bohler-type seat (line CD). Distribution of stresses or displacements along this surface does not affect fields close to the diamond culet (line AG).
- (2) At the symmetry axis $r = 0$ (line AB), shear stress σ_{rz} and horizontal displacements are zero. At the symmetry plane $z = 0$, shear stress σ_{rz} and vertical displacement are zero.
- (3) At the contact surface between the gasket and the anvil, a combined Coulomb friction and plastic friction model, which is described below, is utilized.
- (4) Other surfaces not mentioned above are stress-free.

Finite element algorithms for solution of the boundary-value problems are presented in Feng et al. [28].

Friction Model

According to the combined Coulomb friction and plastic friction model, there is complete cohesion between the contact pairs unless the shear (friction) stress reaches the critical value:

$$\tau_{crit} = \min[\mu(\sigma_c)\sigma_c, \tau_y(p)]. \quad (2)$$

When friction stress reaches τ_{crit} , contact sliding occurs in the radial direction. The critical shear stress $\tau_{crit} = \mu(\sigma_c)\sigma_c$ is related to the Coulomb friction, where μ is the friction coefficient and σ_c is the normal contact stress. However, the Coulomb friction stress cannot exceed the yield strength in shear $\tau_y(p)$, which is defined in terms of the yield strength under compression, σ_y , by $\tau_y = \sigma_y/\sqrt{3}$, based on the von Mises yield criterion. Thus, plastic sliding occurs when the Coulomb friction exceeds $\tau_y(p)$. In fact, it represents plastic shear flow within a very thin material layer immediately bellow the contact surface.

In this study the yield strength and the friction coefficient are assumed to be pressure and contact pressure dependent, respectively.

We assume $\mu = \mu_0 + c\sigma_c$ with two material parameters, which after calibration, looks like

$$\mu = 0.05 + 0.001\sigma_c, \quad \sigma_c \leq 37 \text{ GPa}. \quad (3)$$

Limitations on the contact stress exist because in FEM solutions, Coulomb sliding does not occur for $\sigma_c > 37$ GPa, even for the highest maximum pressure of 380 GPa.

Elastoplastic Material Model under Large Strains and High Pressure

We designate single and double contractions of the second-order tensors $\mathbf{A} = \{A_{ij}\}$ and $\mathbf{B} = \{B_{ij}\}$ over one and two indices as $\mathbf{A} \cdot \mathbf{B} = \{A_{ij}B_{jk}\}$ and $\mathbf{A} : \mathbf{B} = \{A_{ij}B_{ji}\}$, respectively. The subscript s denotes symmetrization, and the subscripts e and p denote elastic and plastic part of a tensor, respectively. The superscripts -1 and T designate the inverse and transposition of a tensor. \mathbf{I} is the second-order unit tensor.

The complete system of equations for a large elastoplastic deformation of a sample is as follows [25,28]:

Decomposition of the deformation gradient \mathbf{F} in to elastic \mathbf{F}_e and plastic \mathbf{F}_p parts

$$\mathbf{F} = \partial \mathbf{r} / \partial \mathbf{r}_0 = \mathbf{F}_e \cdot \mathbf{F}_p = \mathbf{V}_e \cdot \mathbf{R}_e \cdot \mathbf{U}_p = \mathbf{V}_e \cdot \mathbf{V}_p \cdot \mathbf{R}_e, \quad (4)$$

where \mathbf{r} and \mathbf{r}_0 are the position vectors of material points in the actual (deformed) configuration and the reference (undeformed) configuration, respectively; \mathbf{V}_e and \mathbf{V}_p are symmetric elastic and plastic left stretch tensors, respectively, \mathbf{U}_p is the plastic right stretch tensor, and \mathbf{R}_e is the proper orthogonal elastic rotation tensor.

Elastic strain \mathbf{B}_e and its Jaumann objective time derivative

$$\mathbf{B}_e = 0.5(\mathbf{F}_e \cdot \mathbf{F}_e^T - \mathbf{I}), \quad \overset{\nabla}{\mathbf{B}}_e = \dot{\mathbf{B}}_e - 2(\mathbf{W} \cdot \mathbf{B}_e)_s. \quad (5)$$

Plastic strain (plotted in Figs. 5-8)

$$\boldsymbol{\varepsilon}_p = \frac{1}{2} \mathbf{R} \cdot (\mathbf{U}_p \cdot \mathbf{U}_p - \mathbf{I}) \cdot \mathbf{R}^T, \quad (6)$$

Decomposition of the velocity gradient \mathbf{l} , into symmetric deformation rate \mathbf{d} and skew symmetric spin \mathbf{w}

$$\mathbf{l} = \mathbf{w} + \mathbf{d}, \quad \mathbf{d} = \overset{\nabla}{\mathbf{B}}_e - 2(\mathbf{d} \cdot \mathbf{B}_e)_s + \mathbf{V}_e \cdot \mathbf{D}_p \cdot \mathbf{V}_e, \quad \mathbf{D}_p = \mathbf{R}_e \cdot (\dot{\mathbf{U}}_p \cdot \mathbf{U}_p^{-1})_s \cdot \mathbf{R}_e^T, \quad (7)$$

where \mathbf{D}_p is the plastic deformation rate.

Isotropic elasticity rule

$$\boldsymbol{\sigma} = J^{-1}(2\mathbf{B}_e + \mathbf{I}) \cdot \frac{\partial \Psi}{\partial \mathbf{B}_e}. \quad (8)$$

Here $\boldsymbol{\sigma}$ is the true Cauchy stress, $J = \det \mathbf{F}$ is the Jacobian, and Ψ is the specific Helmholtz free energy per unit undeformed volume.

Pressure dependent yield surface (surface of perfect plasticity)

$$\varphi = \sqrt{(3/2) \mathbf{s} : \mathbf{s}} - \sigma_y(p) = 0, \quad (9)$$

where \mathbf{s} is the deviatoric part of Cauchy stress $\boldsymbol{\sigma}$, and σ_y is the yield strength in compression.

Plastic flow rule

$$\mathbf{D}_p = \lambda \mathbf{s} / \sqrt{\mathbf{s} : \mathbf{s}}, \quad (10)$$

where $\lambda \geq 0$ is a scalar determined from the consistency condition $\dot{\varphi} = 0$.

The rate of accumulated plastic strain (plotted in Figs. 5-8)

$$\dot{q} = \left(2 \mathbf{D}_p : \mathbf{D}_p / 3 \right)^{0.5} = \sqrt{2/3} \lambda, \quad (11)$$

Equilibrium condition

$$\nabla \cdot \boldsymbol{\sigma} = 0, \quad (12)$$

where $\nabla \cdot$ is the divergence operator in the deformed configuration.

The yield strength in compression

We assume $\sigma_y = \sigma_{0y} + ap$ with two material parameters, which, after calibration, results in

$$\sigma_y = 1.8 + 0.1p; \quad p \leq 225 \text{ GPa}. \quad (13)$$

Limitation on the pressure exists because, in FEM solutions plastic flow does not occur for $p > 225 \text{ GPa}$, despite the maximum pressure of 380 GPa.

Nonlinear Isotropic Elasticity for Sample

The third-order nonlinear elastic Murnaghan potential is used:

$$\Psi(\mathbf{B}_e) = \frac{\lambda + 2G}{2} I_1^2 - 2GI_2 + \frac{l + 2m}{3} I_1^3 - 2mI_1I_2 + nI_3, \quad (14)$$

where λ, G, l, m, n are material parameters and I_1, I_2, I_3 are invariants of the elastic strain tensor:

$$I_1 = \text{trace}(\mathbf{B}_e), \quad I_2 = B_{e22}B_{e33} - B_{e23}^2 + B_{e11}B_{e33} - B_{e13}^2 + B_{e22}B_{e11} - B_{e12}^2, \quad I_3 = \det \mathbf{B}_e. \quad (15)$$

Furthermore, we have:

$$\begin{aligned} \frac{\partial I_1}{\partial \mathbf{B}_e} &= \mathbf{I}, \quad \frac{\partial I_2}{\partial \mathbf{B}_e} = -\mathbf{B}_e + I_1 \mathbf{I}, \\ \frac{\partial I_3}{\partial \mathbf{B}_e} &= \begin{bmatrix} B_{e22}B_{e33} - B_{e23}B_{e32} & B_{e23}B_{e31} - B_{e33}B_{e21} & B_{e21}B_{e32} - B_{e22}B_{e31} \\ B_{e23}B_{e31} - B_{e33}B_{e21} & B_{e11}B_{e33} - B_{e13}B_{e31} & B_{e12}B_{e31} - B_{e11}B_{e32} \\ B_{e21}B_{e32} - B_{e22}B_{e31} & B_{e12}B_{e31} - B_{e11}B_{e32} & B_{e11}B_{e22} - B_{e12}B_{e21} \end{bmatrix}. \end{aligned} \quad (16)$$

Therefore, according to the elasticity rule Eq. (8), the Cauchy stress can be determined as:

$$\boldsymbol{\sigma} = J^{-1} (2\mathbf{B}_e + \mathbf{I}) \cdot \left[\lambda I_1 \mathbf{I} + 2G\mathbf{B}_e + l I_1^2 \mathbf{I} + 2m I_1 \mathbf{B}_e - 2m I_2 \mathbf{I} + n \frac{\partial I_3}{\partial \mathbf{B}_e} \right]. \quad (17)$$

Nonlinear Anisotropic Elasticity for Diamond

To study the finite elastic strains in diamond, a free energy which includes the fourth-order terms of the Lagrangian strains $\mathbf{E}_e = 0.5(\mathbf{F}_e^T \cdot \mathbf{F}_e - \mathbf{I})$ is utilized as [41]:

$$\begin{aligned}
\Psi = & \frac{1}{2}C_{11}(\eta_1^2 + \eta_2^2 + \eta_3^2) + C_{12}(\eta_1\eta_2 + \eta_2\eta_3 + \eta_1\eta_3) + \frac{1}{2}C_{44}(\eta_4^2 + \eta_5^2 + \eta_6^2) \\
& + \frac{1}{6}C_{111}(\eta_1^3 + \eta_2^3 + \eta_3^3) + \frac{1}{2}C_{112}[\eta_1^2(\eta_2 + \eta_3) + \eta_2^2(\eta_1 + \eta_3) + \eta_3^2(\eta_1 + \eta_2)] \\
& + C_{123}\eta_1\eta_2\eta_3 + C_{456}\eta_4\eta_5\eta_6 + \frac{1}{2}C_{144}(\eta_1\eta_4^2 + \eta_2\eta_5^2 + \eta_3\eta_6^2) \\
& + \frac{1}{2}C_{155}[\eta_4^2(\eta_2 + \eta_3) + \eta_5^2(\eta_1 + \eta_3) + \eta_6^2(\eta_1 + \eta_2)] \\
& + \frac{1}{24}C_{1111}(\eta_1^4 + \eta_2^4 + \eta_3^4) + \frac{1}{6}C_{1112}[\eta_1^3(\eta_2 + \eta_3) + \eta_2^3(\eta_1 + \eta_3) + \eta_3^3(\eta_1 + \eta_2)] \\
& + \frac{1}{4}C_{1122}(\eta_1^2\eta_4^2 + \eta_2^2\eta_5^2 + \eta_3^2\eta_6^2) + C_{1123}\eta_1\eta_2\eta_3(\eta_1 + \eta_2 + \eta_3) \\
& + \frac{1}{4}C_{1155}[\eta_1^2(\eta_6^2 + \eta_5^2) + \eta_2^2(\eta_6^2 + \eta_4^2) + \eta_3^2(\eta_5^2 + \eta_4^2)] \\
& + \frac{1}{2}C_{1255}[\eta_1\eta_2(\eta_4^2 + \eta_5^2) + \eta_3\eta_2(\eta_6^2 + \eta_5^2) + \eta_1\eta_3(\eta_6^2 + \eta_4^2)] \\
& + \frac{1}{2}C_{1266}(\eta_1\eta_2\eta_6^2 + \eta_2\eta_3\eta_4^2 + \eta_1\eta_3\eta_5^2) + C_{1456}\eta_4\eta_5\eta_6(\eta_1 + \eta_2 + \eta_3) \\
& + \frac{1}{24}C_{4444}(\eta_4^4 + \eta_5^4 + \eta_6^4) + \frac{1}{4}C_{4455}(\eta_4^2\eta_5^2 + \eta_6^2\eta_5^2 + \eta_4^2\eta_6^2),
\end{aligned} \tag{18}$$

where

$$\eta_1 = \mathbf{E}_{e11}, \quad \eta_2 = \mathbf{E}_{e22}, \quad \eta_3 = \mathbf{E}_{e33}, \quad \eta_4 = 2\mathbf{E}_{e23}, \quad \eta_5 = 2\mathbf{E}_{e31}, \quad \eta_6 = 2\mathbf{E}_{e12}. \tag{19}$$

Therefore, based on the elasticity law, the Cauchy stress in the diamond can be determined as:

$$\boldsymbol{\sigma} = \frac{1}{J} \mathbf{F}_e \cdot \frac{\partial \Psi}{\partial \mathbf{E}_e} \cdot \mathbf{F}_e^T. \tag{20}$$

Material Properties

Diamond

All elastic material constants are taken from Telichko et al. [42], which, to the authors' knowledge, is the only reference that provides all third- and fourth-order elastic constants for diamond. These were determined using first principle simulations. Thus, we used the following elastic constants in our simulations:

$$\begin{aligned}
C_{11} &= 1081.9, C_{12} = 125.2, C_{44} = 578.6, \\
C_{111} &= -7611, C_{112} = -1637, C_{123} = 640, C_{144} = -199, C_{166} = -4000, C_{456} = -1148, \\
C_{1111} &= 26687, C_{1112} = 31214, C_{1122} = 20044, C_{1123} = -425, C_{1144} = -1385, C_{1155} = 10741, \\
C_{1255} &= -264, C_{1266} = 819, C_{1456} = 487, C_{4444} = 11328, C_{4455} = 528 \text{ GPa}.
\end{aligned} \tag{21}$$

Since available data for the third-order elastic constants from different references have significant scatter [43-46], we assume that some of the fourth-order elastic constants are not precise either. Indeed, for the elastic constants from Telichko et al. [42], we were unable to obtain the experimental equation of state collected in Maezono et al. [47]. Thus, we changed C_{1112} , C_{1122} , and C_{1266} to the values indicated in Eq. (21) in order to received good correspondence with the equation of state from Sato et al.[48]; see Figure 12, and sample profile at highest pressure, see Figure 2c.

A majority of equations of state of diamond determined by different methods [51,52] falls in between those from Sato et al. [48] and McSkimin et al. [50]. Modifying the higher-order elastic properties of the diamond is another advancement over ref. [27].

Tungsten

The elastic constants of the polycrystalline tungsten from Vekilov et al. [53] are used in this study, with some modifications:

$$\lambda = 206.5, G = 150.3, l = -404, m = -1,081, n = -1,164 \text{ GPa}. \tag{22}$$

The third order constants m and n for polycrystal have been found from the elastic constants for single crystal using the simplest Voight averaging scheme. Thus, they may have significant indeterminacy. We changed n and m to obtain a slightly better fit to the experimental pressure distribution curves for three lowest pressure.

Geometric Interpretation of the Postulate of Perfect Plasticity [24]

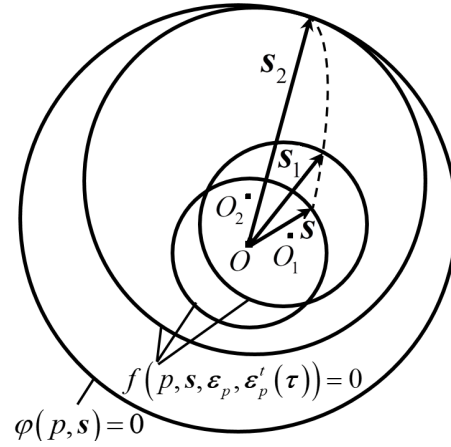


Figure 13. Schematic of evolution of the yield surface $f(p, s, \epsilon_p, \epsilon_p^t(\tau)) = 0$ until it reaches the fixed surface of perfect plasticity $\varphi(p, s) = 0$ in a “five-dimensional” space of deviatoric stresses s at fixed pressure p . The initial yield surface and the fixed surface of perfect plasticity $\varphi(p, s) = 0$ are isotropic and pictured here as circles with their center at O . Two other yield surfaces depend on plastic strain ϵ_p at the current time t and the entire plastic strain history $\epsilon_p^t(\tau)$ before time t . These surfaces acquire strain-induced anisotropy, which is depicted by the shifted centers of the surfaces O_1 and O_2 . However, when the yield surface reaches the fixed surface of perfect plasticity $\varphi(p, s) = 0$, which is isotropic and plastic strain- and plastic strain history-independent, moves along it at further loading, the material deforms as perfectly plastic, isotropic with the fixed surface of perfect plasticity $\varphi(p, s) = 0$.

Data Availability

The authors declare that the main data supporting the findings of this study are available within the article. Extra data are available from the corresponding author upon request.

Acknowledgements

We thank Bing Li for sharing some details for sample in their paper [6]. Support from Army Research Office (Grant W911NF-17-1-0225), National Science Foundation (Grant DMR-1904830), and Office of Naval Research (Grant N00014-19-1-2082) is greatly acknowledged. Some computations have been performed using the Extreme Science and Engineering Discovery Environment (XSEDE allocations TG MSS170003 and MSS170015).

Competing interests

The Authors declare no Competing Financial or Non-Financial Interests.

Author Contributions

VL designed and supervised research, developed model, analyzed results and wrote paper. MK modified and extended the FEM algorithm, performed all simulations, and participated in analysis and writing paper. BF developed FEM algorithm and ABAQUS subroutines.

References

- [1] Shen, G. Mao, H. K. High-pressure studies with x-rays using diamond anvil cells. *Rep. Prog. Phys.* **80**, 016101 (2017).
- [2] Mao, H. K. Chen, X. J. Ding, Y. Li, B. Wang, L. Solids, liquids, and gases under high pressure. *Rev. Mod. Phys.* **90**, 015007 (2018).
- [3] Dubrovinsky, L. et al. The most incompressible metal osmium at static pressures above 750 gigapascals. *Nature* **525**, 226-229 (2015).
- [4] Goettel, K. A. Mao, H. Bell, P. M. Generation of static pressures above 2.5 megabars in a diamond-anvil pressure cell. *Rev. Sci. Instrum.* **56**, 1420-1427 (1985).
- [5] Hemley, R. J. et al. D. X-ray imaging of stress and strain of diamond, iron, and tungsten at megabar pressures. *Science* **276**, 1242-1245 (1997).

- [6] Li, B. et al. Diamond anvil cell behavior up to 4 mbar, PNAS 115, 1713-1717 (2018).
- [7] Jeanloz, R. Godwal, B. K. Meade, C. Static strength and equation of state of rhenium at ultra-high pressures. Nature 349, 687-689 (1991).
- [8] Wenk, H. R. Matthies, S. Hemley, R. J. Mao, H. K. Shu, J. The plastic deformation of iron at pressures of the earth's inner core. Nature 405, 1044–1047 (2000).
- [9] Deb, S. K. Wilding, M. Somayazulu, M. McMillan, P. F. Pressure-induced amorphization and an amorphous-amorphous transition in densified porous silicon. Nature 414, 528–530 (2001).
- [10] Mao, H. K. Shu, J. Shen, G. Hemley, R. J. Li, B. Singh, A. K. Elasticity and rheology of iron above 220 GPa and the nature of the earth's inner core. Nature 396, 741–743 (1998).
- [11] Dias, R. P. Silvera, I. F. Observation of the Wigner-Huntington transition to metallic hydrogen. Science 355, 715-718 (2017).
- [12] Ji, C. Levitas, V. I. Zhu, H. Chaudhuri, J. Marathe, A. Ma, Y. Shear-induced phase transition of nanocrystalline hexagonal boron nitride to wurtzitic structure at room temperature and low pressure. PNAS USA. 109, 19108-19112 (2012).
- [13] Meade, C. Jeanloz, R. Effect of a coordination change on the strength of amorphous SiO₂. Science 241, 1072-1074 (1988).
- [14] Bridgman, P. W. Effects of high shearing stress combined with high hydrostatic pressure. Phys. Rev. 48, 825–847 (1935).
- [15] Levitas, V. I. High-pressure mechanochemistry: conceptual multiscale theory and interpretation of experiments. Phys. Rev. B 70, 184118 (2004).
- [16] Barge, N. V. Boehler, R. Effect of non-hydrostaticity on the α - ϵ transition of iron. High Press. Res. 6, 133–140 (2006).
- [17] Downs, R. Singh, A. Analysis of deviatoric stress from nonhydrostatic pressure on a single crystal in a diamond anvil cell: the case of monoclinic aegirine, NaFeSi₂O₆. J. Phys. Chem. Solids 67, 1995-2000 (2006).
- [18] Duffy, T. S. et al. Lattice strains in gold and rhenium under nonhydrostatic compression to 37 GPa. Phys. Rev. B 60, 15063 (1999).
- [19] Merkel, S. Liermann, H. P. Miyagi, L. Wenk, H. R. In situ radial x-ray diffraction study of texture and stress during phase transformations in bcc-, fcc- and hcp-iron up to 36 GPa and 1000 K. Acta Mater. 61, 5144-5151 (2013).

- [20] Levitas, V. I. High pressure phase transformations revisited. *J. Physics: Condensed Matter* 30, 163001 (2018).
- [21] Levitas, V. I. Shvedov, L. K. Low pressure phase transformation from rhombohedral to cubic BN: experiment and theory. *Phys. Rev. B* 65, 104109 (2002).
- [22] Blank, V. D. Estrin, E. I. *Phase Transitions in Solids under High Pressure* (New York, CRC Press, 2014).
- [23] Moss, W. C. Hallquist, J. O. Reichlin, R. Goettel, K. A. Martin, S. Finite-element analysis of the diamond anvil cell - achieving 4.6 Mbar. *Appl. Phys. Lett.* 48, 1258-1260 (1986).
- [24] Levitas, V. I. *Large Deformation of Materials with Complex Rheological Properties at Normal and High Pressure* (Nova Science Publishers, New York, 1996).
- [25] Levitas, V. I. Polotnyak, S. B. Idesman, A. V. Large elastoplastic strains and the stressed state of a deformable gasket in high pressure equipment with diamond anvils. *Strength Mater.* 3, 221-227 (1996).
- [26] Merkel, S. Hemley, R. J. Mao, H. K. Finite-element modeling of diamond deformation at multimegabar pressures. *Appl. Phys. Lett.* 74, 656-658 (1999).
- [27] Feng, B. Levitas, V. I. Hemley, R. J. Large elastoplasticity under static megabar pressures: formulation and application to compression of samples in diamond anvil cells. *Int. J. Plast.* 84, 33-57 (2016).
- [28] Feng, B. Levitas, V. I. Coupled elastoplasticity and plastic strain-induced phase transformation under high pressure and large strains: formulation and application to BN sample compressed in a diamond anvil cell. *Int. J. Plast.* 96, 156-181 (2017).
- [29] Feng, B. Levitas, V. I. Pressure self-focusing effect and novel methods for increasing the maximum pressure in traditional and rotational diamond anvil cells. *Sci. Rep.* 7, 45461 (2017).
- [30] Lubliner, J. *Plasticity Theory* (Macmillan, New York, 1990).
- [31] Fleck, N. A. Muller, G. M. Ashby, M. F. Hutchinson, J. W. Strain gradient plasticity - theory and experiment. *Acta Metall. Mater.* 42, 475-487 (1994).
- [32] Chakravarthy, S. S. Curtin, W. A. Stress-gradient plasticity. *PNAS USA.* 108, 15716-15720 (2011).
- [33] Liu, D. B. Dunstan, D. J. Material length scale of strain gradient plasticity: a physical interpretation. *Int. J. Plast.* 98, 156-174 (2017).

- [34] Levitas, V. I. Ma, Y. Selvi, E. Wu, J. Patten, J. High-density amorphous phase of silicon carbide obtained under large plastic shear and high pressure. *Phys. Rev. B* 85, 054114 (2012).
- [35] Levitas, V. I. High-pressure phase transformations under severe plastic deformation by torsion in rotational anvils. *Material Transactions*, 60 (7), (2019), doi:10.2320/matertrans.MF201923.
- [36] Gao, Y. Ma, Y. An, Q. Levitas, V. I. Zhang, Y. Feng, B. Chaudhuri, J. Goddard III, W. A. Shear driven formation of nano-diamonds at sub-gigapascals and 300 K. *Carbon*. 146, 364-368 (2019).
- [37] Feng, B. Levitas, V. I. Large elastoplastic deformation of a sample under compression and torsion in a rotational diamond anvil cell under megabar pressures. *Int. J. Plasticity* 92, 79–95 (2017).
- [38] Umeno, Y. Černý, M. Effect of normal stress on the ideal shear strength in covalent crystals. *Physical Review B* 77, 100101 (2008).
- [39] Černý, M. Rehak, P. Umeno, Y. Pokluda. J. Stability and strength of covalent crystals under uniaxial and triaxial loading from first principles. *J. Phys. Condens. Matter*. 25, 035401 (2013).
- [40] Hsieh, S. Bhattacharyya, P. Zu, C. Mittiga, T. Smart, T. J. Machado, F. Kobrin, B. Höhn, T. O. Rui, N. Z. Kamrani, M. Chatterjee, S. Choi, S. Zaletel, M. Struzhkin, V. V. Moore, J. E. Levitas, V. I. Jeanloz, R. Yao, N. Y. Imaging stress and magnetism at high pressures using a nanoscale quantum sensor. *Science*, resubmitted (2019); arXiv:1812.08796 [cond-mat.mes-hall; cond-mat.mtrl-sci], December 20, 2018, 68 P.
- [41] Vekilov, Y. K. Krasilnikov, O. M. Lugovskoy, A. V. Elastic properties of solids at high pressure. *Physics-Uspekhi* 58, 1106-1114 (2014).
- [42] Telichko, A. V. et al. Diamond's third-order elastic constants: ab initio calculations and experimental investigation. *J. Mater. Sci.* 52, 3447-3456 (2017).
- [43] Hmiel, A. Winey, J. M. Gupta, Y. M. Desjarlais, M. P. Nonlinear elastic response of strong solids: first-principles calculations of the third-order elastic constants of diamond. *Phys. Rev. B* 93, 174113 (2016).
- [44] Winey, J. M. Hmiel, A. Gupta, Y. M. Third-order elastic constants of diamond determined from experimental data. *J. Phys. Chem. Solids* 93, 118-120 (2016).
- [45] Lang, J. M. Gupta, Y. M. Experimental determination of third-order elastic constants of diamond. *Phys. Rev. Lett.* 106, 125502 (2011).

- [46] Keating, P. N. Theory of the third order elastic constants of diamond-like crystals. *Phys. Rev.* 149, 674-678 (1966).
- [47] Maezono, R. Ma, A. Towler, M. D. Needs, R. J. Equation of state and raman frequency of diamond from quantum monte carlo simulations. *Phys. Rev. Lett.* 98, 025701 (2007).
- [48] Sato, T. Ohashi, K. Sudoh, T. Haruna, K. Maeta, H. The ambient-pressure lattice constants of pure diamond with natural isotopic composition are given as 3.566 88 Å at 300 K and 3.566 505 Å at 0 K. *Phys. Rev. B* 65, 092102 (2002).
- [49] Occelli, F. Loubeyre, P. LeToullec, R. Properties of diamond under hydrostatic pressures up to 140 GPa. *Nat. Mater.* 2, 151-154 (2003).
- [50] McSkimin, H. J. Andreatch, P. Elastic moduli of diamond as a function of pressure and temperature. *J. Appl. Phys.* 43, 2944-48 (1972).
- [51] Holzapfel, W. B. Refinement of the ruby luminescence pressure scale. *J. Appl. Phys.* 93, 1813-18 (2003).
- [52] Kunc, K. Loa, I. Syassen, K. Equation of state and phonon frequency calculations of diamond at high pressures. *Phys. Rev. B* 68, 094107 (2003).
- [53] Vekilov, Y. K. Krasilnikov, O. M. Lugovskoy, A. V. Lozovik, Y. E. Higher-order elastic constants and megabar pressure effects of bcc tungsten: ab initio calculations. *Phys. Rev. B* 94, 104114 (2016).

CHAPTER 5. IMAGING STRESS AND MAGNETISM AT HIGH PRESSURES USING A NANOSCALE QUANTUM SENSOR

This Section reproduces paper S. Hsieh, P. Bhattacharyya, C. Zu1, T. Mittiga, T. J. Smart, F. Machado, B. Kobrin, T. O. Höhn, N. Z. Rui1, M. Kamrani, S. Chatterjee, S. Choi, M. Zalete, V. V. Struzhkin, J. E. Moore, V. I. Levitas, R. Jeanloz, N.Y.Yao, Imaging stress and magnetism at high pressures using a nanoscale quantum sensor, *Science* 366, 1349–1354 (2019).

Abstract

Pressure alters the physical, chemical, and electronic properties of matter. The diamond anvil cell enables tabletop experiments to investigate a diverse landscape of high-pressure phenomena. Here, we introduce and use a nanoscale sensing platform that integrates nitrogen-vacancy (NV) color centers directly into the culet of diamond anvils. We demonstrate the versatility of this platform by performing diffraction-limited imaging of both stress fields and magnetism as a function of pressure and temperature. We quantify all normal and shear stress components and demonstrate vector magnetic field imaging, enabling measurement of the pressure-driven $\alpha \rightarrow \epsilon$ phase transition in iron and the complex pressure-temperature phase diagram of gadolinium. A complementary NV-sensing modality using noise spectroscopy enables the characterization of phase transitions even in the absence of static magnetic signatures.

In hybrid quantum-sensing devices, sensors are directly integrated into existing toolsets ranging from biological imaging to materials spectroscopy [1-4]. Here, we demonstrate the

versatility of a platform based on quantum spin defects combined with static high-pressure technologies [5, 6]. In particular, we instrument diamond anvil cells (DACs) with a layer of nitrogen-vacancy (NV) centers directly at the culet, enabling the pursuit of two complementary objectives in high pressure science: understanding the strength and failure of materials under pressure (e.g., the brittle-ductile transition) and discovering and characterizing exotic phases of matter (e.g., pressure-stabilized high-temperature superconductors) [7–11]. Achieving these goals hinges upon the sensitive in situ imaging of signals within the high-pressure chamber. For the first goal, measuring the local stress environment permits the direct observation of inhomogeneities in plastic flow and the formation of line defects. For the second goal, the ability to spatially resolve field distributions can provide a direct image of complex order parameters and textured phenomena such as magnetic domains. However, the enormous stress gradients generated near the sample limit the utility of most conventional tabletop spectroscopy techniques; as a result, one is often restricted to measuring bulk properties averaged over the entire DAC geometry. Our approach to these challenges is to use an ensemble of NV centers [~ 1 part per million (ppm) density] implanted ~ 50 nm from the surface of the diamond anvil culet (Figure 1, A and B). Each NV center represents an atomic scale defect (i.e., a substitutional nitrogen impurity adjacent to a vacancy) inside the diamond lattice and exhibits an $S = 1$ electronic spin ground state [12]. In the absence of external fields, the $|m_s = \pm 1\rangle$ spin sublevels are degenerate and separated by $D_{gs} = (2\pi) \times 2.87$ GHz from the $|m_s = 0\rangle$ state. Crucially, both the nature and energy of these spin states are sensitive to local changes in stress, temperature, and magnetic and electric fields (Figure 1C) [13–19]. These spin states can be optically initialized and read out, as well as coherently manipulated through microwave fields. Their energy levels can be probed by performing optically detected magnetic resonance (ODMR)

spectroscopy, which measures a change in the NV's fluorescence intensity when an applied microwave field is on resonance between two NV spin sublevels (Figure 1D), thus enabling a variety of external signals to be sensed over a wide range of environmental conditions [1, 20, 21].

Here, we focus on the sensing of stress and magnetic fields, wherein the NV is governed by the Hamiltonian [18, 22], $H = H_0 + H_B + H_S$ with $H_0 = D_{gs}S_z^2$ (zero-field splitting), $H_S = \gamma_B \vec{B} \cdot \vec{S}$ (Zeeman splitting), and $H_S = [\alpha_1(\sigma_{xx} + \sigma_{yy}) + \beta_1\sigma_{zz}]S_z^2 + [\alpha_2(\sigma_{yy} - \sigma_{xx}) + \beta_2(2\sigma_{xz})](S_y^2 - S_x^2) + [\alpha_2(2\sigma_{xy}) + \beta_2(2\sigma_{yz})](S_xS_y + S_yS_x)$ capturing the NV's response to the local diamond stress tensor, $\vec{\sigma}$ (Figure 1C). In the above, $\gamma_B \approx (2\pi) \times 2.8$ MHz/G is the gyromagnetic ratio, $\{\alpha_{1,2}, \beta_{1,2}\}$ are the stress susceptibility coefficients [17–19, 23], \tilde{Z} is the NV orientation axis, and \tilde{X} is defined such that the xz plane contains one of the carbon-vacancy bonds (Figure 1E). In general, the resulting ODMR spectra exhibit eight resonances arising from the four possible crystallographic orientations of the NV (Figure 1D). By extracting the energy shifting and splitting of the spin sublevels for each NV orientation group, one obtains an over constrained set of equations enabling the reconstruction of either the (six component) local stress tensor or the (three component) vector magnetic field [23].

In our experiments, we use a miniature DAC (Figure 1, A and B) consisting of two opposing anvils compressing either a beryllium copper or rhenium gasket [24]. The sample chamber defined by the gasket and diamond-anvil culets is filled with a pressure-transmitting medium (either a 16:3:1 methanol/ethanol/water solution or cesium iodide) to provide a quasi-hydrostatic environment. Microwave excitation is applied with a 4-mm-thick platinum foil compressed between the gasket and anvil pavilion facets (figure S1); scanning confocal

microscopy (with a transverse diffraction-limited spot size of ~ 600 nm, containing $\sim 10^3$ NVs) allows us to obtain two dimensional ODMR maps across the culet.

We begin by probing the stress tensor across the culet surface (up to $P=48$ GPa as shown in figure S7) using two different cuts of diamond [i.e., (111)-cut and (110)-cut culet]. For a generic stress environment, the intrinsic degeneracy associated with the four NV orientations is not sufficiently lifted, implying that individual resonances cannot be resolved. To resolve these resonances while preserving the stress contribution, we sequentially tune a precisely controlled external magnetic field to be perpendicular to each of the different NV orientations (23). For each perpendicular field choice, three of the four NV orientations exhibit a strong Zeeman splitting proportional to the projection of the external magnetic field along their symmetry axes. Notably, this enables one to resolve the stress information encoded in the remaining NV orientation, whereas the other three groups of NVs are spectroscopically split away. Using this method, we obtain sufficient information to extract the full stress tensor, as depicted in Figure 2. A number of intriguing features are observed at the interface between the culet and the sample chamber, which provide insight into both elastic (reversible) and plastic (irreversible) deformations.

At low pressures ($P=4.9$ GPa), the normal stress along the loading axis, σ_{zz} , is spatially uniform (Figure 2A), whereas all shear stresses, $\{\sigma_{xy}, \sigma_{xz}, \sigma_{yz}\}$, are minimal (Figure 2B). The axes $\{\hat{X}, \hat{Y}, \hat{Z}\}$, correspond to the lab frame, whereas $\{\hat{x}, \hat{y}, \hat{z}\}$ correspond to the NV frame (Figure 1, A and E). These observations are in agreement with conventional stress continuity predictions for the interface between a solid and an ideal fluid (25). Moreover, σ_{zz} is consistent with the independently measured pressure inside the sample chamber (by ruby fluorescence), demonstrating the NV's potential as a built-in pressure scale [26]. In contrast to the uniformity of

σ_{zz} , the field profile for the mean lateral stress, $\sigma_{\perp} = \frac{1}{2}(\sigma_{xx} + \sigma_{yy})$, exhibits a concentration of forces toward the center of the culet (Figure 2A). Using the measured σ_{zz} as a boundary condition, we perform finite-element simulations to reproduce this spatial pattern [23].

Upon increasing pressure ($P=13.6$ GPa), a spatial gradient in σ_{zz} emerges (Figure 2B, inset). This qualitatively distinct feature is consistent with the solidification of the pressure transmitting medium into its glassy phase above $P_g \approx 10.5$ GPa (27). Crucially, this demonstrates our ability to characterize the effective viscosity of solids and liquids under pressure. To characterize the sensitivity of our system, we perform ODMR spectroscopy with a static applied magnetic field and pressure under varying integration times and extract the frequency uncertainty from a Gaussian fit. We observe a stress sensitivity of $\{0.023, 0.030, 0.027\} \text{ GPa}/\sqrt{\text{Hz}}$ for hydrostatic, average normal, and average shear stresses, respectively. This is consistent with the theoretically derived stress sensitivity, $\eta_s \sim \frac{\Delta\nu}{\zeta C \sqrt{Nt}} = \{0.017, 0.022, 0.020\} \text{ GPa}/\sqrt{\text{Hz}}$, where N is the number of NV centers, $\Delta\nu$ is the linewidth, ζ is the relevant stress susceptibility, t is the integration time, and C is an overall factor accounting for measurement infidelity [23]. In combination with diffraction-limited imaging resolution, this sensitivity makes it possible to measure and ultimately control the full stress tensor distribution across a sample.

Having characterized the stress environment, we use the NV centers as an in situ magnetometer to detect phase transitions inside the high pressure chamber. Analogous to the case of stress, we observe a magnetic sensitivity of $12 \mu\text{T}/\sqrt{\text{Hz}}$, in agreement with the theoretically estimated value, $\eta_B \sim \frac{\delta\nu}{C\gamma_B B \sqrt{Nt}} = 8.8 \mu\text{T}/\sqrt{\text{Hz}}$. Assuming a point dipole located a distance $d \sim 5$ nm from the NV layer, this corresponds to an experimentally measured magnetic moment sensitivity: $7.5 \times 10^{-12} \text{ emu}/\sqrt{\text{Hz}}$ (Figure 1F).

After determining the sensitivity, we begin by directly measuring the magnetization of iron as it undergoes the pressure-driven $\alpha \leftrightarrow \epsilon$ phase transition from body-centered cubic (bcc) to hexagonal close-packed (hcp) crystal structures [28]; crucially, this structural phase transition is accompanied by the depletion of the magnetic moment, and it is this change in the iron's magnetic behavior that we image. The sample chamber is loaded with a ~ 10 -mm polycrystalline iron pellet as well as a ruby microsphere (pressure scale), and we apply an external magnetic field $B_{\text{ext}} \sim 180$ G. As before, by performing a confocal scan across the culet, we acquire a two-dimensional magnetic resonance map (Figure 3). At low pressures (Figure 3A), near the iron pellet, we observe substantial shifts in the eight NV resonances, owing to the presence of a ferromagnetic field from the iron pellet. As one increases pressure (Figure 3B), these shifts begin to diminish, signaling a reduction in the magnetic susceptibility. Finally, at the highest pressures ($P \sim 22$ GPa, Figure 3C), the magnetic field from the pellet has decreased by more than two orders of magnitude.

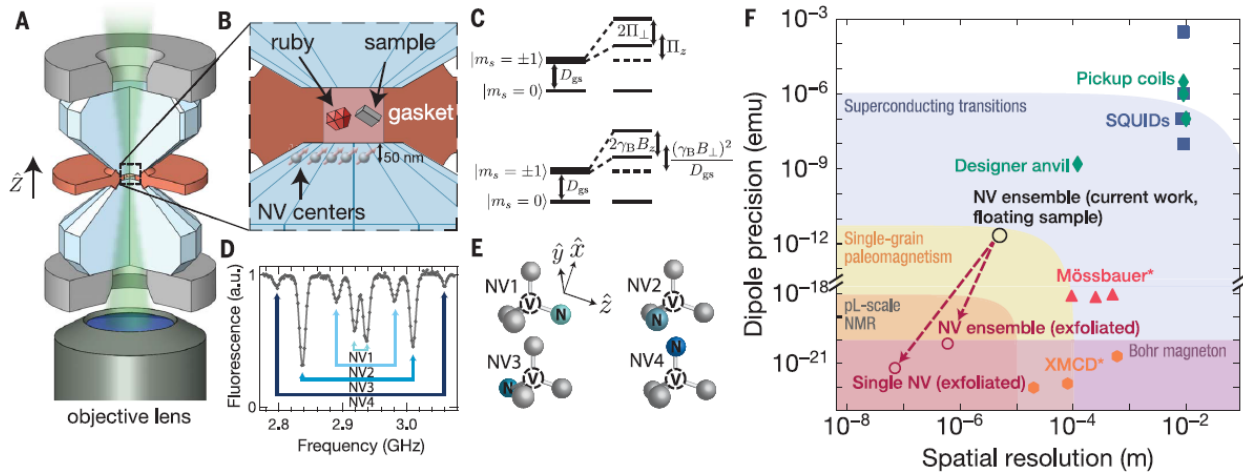


Figure 1. NV centers integrated into a diamond anvil cell. (A) Schematic of the DAC geometry.

Two opposing anvils are compressed by a nonmagnetic steel cell and cubic boron nitride backing plates (gray). NV centers are initialized and read out using a 532-nm laser focused to a

diffraction-limited spot (~ 600 nm), which is scanned across the culet surface. (B) The DAC sample chamber is defined by the gasket-anvil assembly (diagram not to scale); it is loaded with the sample of interest, a pressure-transmitting medium, and a single ruby microsphere (pressure calibration). A ~ 50 -nm layer of NV centers is embedded into the diamond anvil directly below the sample chamber. (C) Top: Stress both shifts and splits the $m_s = \pm 1$ sublevels at first order; in particular, the shifting is characterized by $\Pi_Z = \alpha_1(\sigma_{xx} + \sigma_{yy}) + \beta_1\sigma_{zz}$, and the splitting is characterized by $\Pi_{\perp}^2 = [\alpha_2(\sigma_{yy} - \sigma_{xx}) + \beta_2(2\sigma_{xz})]^2 + [\alpha_2(2\sigma_{xy}) + \beta_2(2\sigma_{yz})]^2$. Bottom: An axial magnetic field splits the $m_s = \pm 1$ sublevels at first order, but a transverse magnetic field leads to shifts only at second order. (D) A representative ODMR spectrum from an NV center ensemble under an applied magnetic field. (E) Each pair of resonances in (D) corresponds to one of the four NV crystallographic orientations. (F) Comparison of high-pressure magnetometry techniques. We define the spatial resolution as a characteristic sensor length scale over which the sample magnetism is integrated. Estimates for our current work are shown assuming a sample suspended in a pressure medium 5 mm away from the culet (black open circle). We project that by exfoliating a sample directly onto the culet surface and using 5-nm implanted NV centers, the distance from the sample can be substantially reduced, thus improving both dipole precision and spatial resolution (open red circles). Inductive methods [pickup coils (green diamonds) and superconducting quantum interference devices (SQUIDs) (blue squares)] integrate the magnetization of a sample over the coil's area [23]; to this end, the diameter associated with the coil is taken as the "spatial resolution" although in principle, the sample inside the chamber can be substantially smaller. By contrast, high-energy photon scattering techniques [x-ray magnetic circular dichroism (orange hexagons), and Mössbauer spectroscopy (pink triangles)] probe

atomic-scale magnetism [23]; the length scale for these methods is shown here as the spot size of the excitation beam.

To quantify this phase transition, we reconstruct the full vector magnetic field produced by the iron sample from the aforementioned two-dimensional NV magnetic resonance maps (Figure 3, D to F). We then compare this information with the expected field distribution at the NV layer inside the cuilet, assuming the iron pellet generates a dipole field (23). This enables us to extract an effective dipole moment as a function of applied pressure (Figure 3G). To identify the critical pressure, we fit the transition using a logistic function (23). This procedure yields the transition at $P=16.7 \pm 0.7$ GPa (Figure 3J).

In addition to changes in the magnetic behavior, another key signature of this first order transition is the presence of hysteresis. We investigate this by slowly decompressing the diamond anvil cell and monitoring the dipole moment; the decompression transition occurs at $P=10.5 \pm 0.7$ GPa (Figure 3J), suggesting a hysteresis width of ~ 6 GPa, consistent with a combination of intrinsic hysteresis and finite shear stresses in the methanol/ethanol/ water pressure-transmitting medium [28]. Taking the average of the forward and backward hysteresis pressures, we find a critical pressure of $P_c=13.6 \pm 3.6$ GPa, in excellent agreement with independent measurements by Mössbauer spectroscopy, where $P_c \approx 12$ GPa (Figure 3J) [28].

Next, we demonstrate the integration of our platform into a cryogenic system, enabling us to make spatially resolved in situ measurements across the pressure-temperature (P-T) phase diagram of materials. Specifically, we investigate the magnetic P - T phase diagram of the rare-earth element gadolinium (Gd) up to pressures $P \approx 8$ GPa and between temperatures $T = 25$ to

340 K. Owing to an interplay between localized 4f electrons and mobile conduction electrons, Gd represents an interesting playground for studying metallic magnetism; in particular, the itinerant electrons mediate RKKY-type interactions between the local moments, which in turn induce spin-polarization of the itinerant electrons [29]. Moreover, much like its rare-earth cousins, Gd exhibits a series of pressure driven structural phase transitions from hcp to samarium-type (Sm-type) to double hcp (dhcp) (Figure 4) [30]. The interplay between these different structural phases, various types of magnetic ordering, and metastable transition dynamics leads to a complex magnetic P - T phase diagram that remains the object of study to this day [29–31].

In analogy to our measurements of iron, we monitor the magnetic ordering of a Gd flake by using the NV's ODMR spectra at two different locations inside the culet: close to and far away from the sample (the latter to be used as a control) (figure S15). Because of thermal contraction of the DAC (which induces a change in pressure), each experimental run traces a distinct non-isobaric path through the P - T phase diagram (Figure 4C, blue curves). In addition to these DC magnetometry measurements, we also operate the NV sensors in a complementary mode, i.e., as a noise spectrometer.

We begin by characterizing Gd's well-known ferromagnetic Curie transition at ambient pressure, which induces a sharp jump in the splitting of the NV resonances at $T_C = 292.2 \pm 0.1$ K (Figure 4D). As depicted in Figure 4A, upon increasing pressure, this transition shifts to lower temperatures, and consonant with its second-order nature (32), we observe no hysteresis (Figure 4A, inset); this motivates us to fit the data and extract T_C by solving a regularized Landau free-energy equation [23].

Combining all of the low pressure data (Figure 4C, red squares), we find a linear decrease in the Curie temperature at a rate $dT_C/dP = -18.7 \pm 0.2$ K/GPa, consistent with prior studies using both DC conductivity and AC-magnetic susceptibility [30]. Unexpectedly, this linear decrease extends well into the Sm-type phase. Upon increasing pressure above ~ 6 GPa (path [b] in Figure 4C), we observe the loss of ferromagnetic (FM) signal (Figure 4B), indicating a first-order structural transition into the paramagnetic (PM) dhcp phase [30]. In stark contrast to the previous Curie transition, there is no revival of a ferromagnetic signal even after heating up (~ 315 K) and substantially reducing the pressure (to < 0.1 GPa).

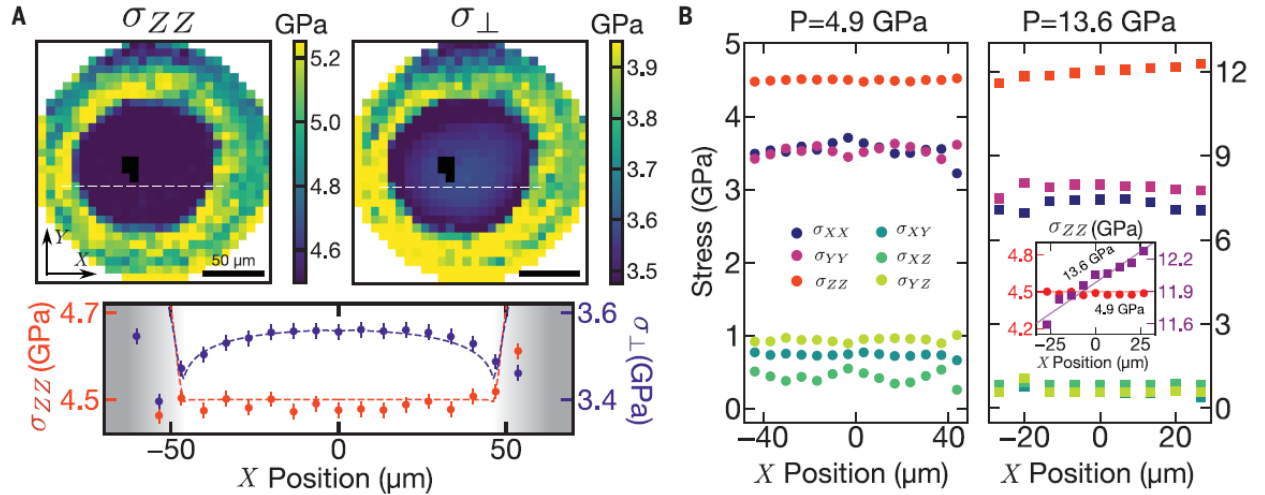


Figure 2. Full tensorial reconstruction of the stresses in a (111)-cut diamond anvil. (A) Spatially resolved maps of the loading stress (left) and mean lateral stress (right), $\sigma_{\perp} = \frac{1}{2}(\sigma_{XX} + \sigma_{YY})$, across the culet surface. In the inner region, where the culet surface contacts the pressure-transmitting medium (16:3:1 methanol/ethanol/water), the loading stress is spatially uniform, whereas the lateral stress is concentrated toward the center; this qualitative difference is highlighted by a linecut (taken along the white-dashed line) of the two stresses (below), and reconstructed by finite-element analysis (orange and purple dashed lines). The black pixels indicate where the NV spectrum was obfuscated by the ruby microsphere. (B) Comparison of all

stress tensor components in the fluid-contact region at $P = 4.9$ GPa and $P = 13.6$ GPa. At $P = 13.6$ GPa, the pressure-transmitting medium has entered its glassy phase, and we observe a spatial gradient in the loading stress σ_{zz} (inset).

A few remarks are in order. The linear decrease of T_C well beyond the ~ 2 -GPa structural transition between hcp- and Sm-type is consistent with the “sluggish” equilibration between these two phases at low temperatures [30]. The metastable dynamics of this transition are strongly pressure and temperature dependent, suggesting that different starting points (in the P-T phase diagram) can exhibit markedly different behaviors [30]. To highlight this, we probe two different transitions out of the paramagnetic Sm-type phase by tailoring specific paths in the P-T phase diagram. By taking a shallow path in P-T space, we observe a small change in the local magnetic field across the structural transition into the PM dhcp phase at ~ 6 GPa (Figure 4C, path [c], orange diamonds). By taking a steeper path in P-T space, one can also investigate the magnetic transition into the antiferromagnetic (AFM) Sm-type phase at ~ 150 K (Figure 4C, path [d], green triangle). In general, these two transitions are extremely challenging to probe via DC magnetometry because their signals arise only from small differences in the susceptibilities between the various phases (figure S18).

To this end, we demonstrate a complementary NV sensing modality based on noise spectroscopy, which can probe phase transitions even in the absence of a direct magnetic signal [33]. Specifically, returning to Gd’s ferromagnetic Curie transition, we monitor the NV’s depolarization time, T_1 , as the phase transition is crossed (Figure 4D). Normally, the NV’s T_1 time is limited by spin-phonon interactions and increases sharply as the temperature is decreased. Here, we observe a markedly disparate behavior. In particular, using nano-diamonds drop-cast

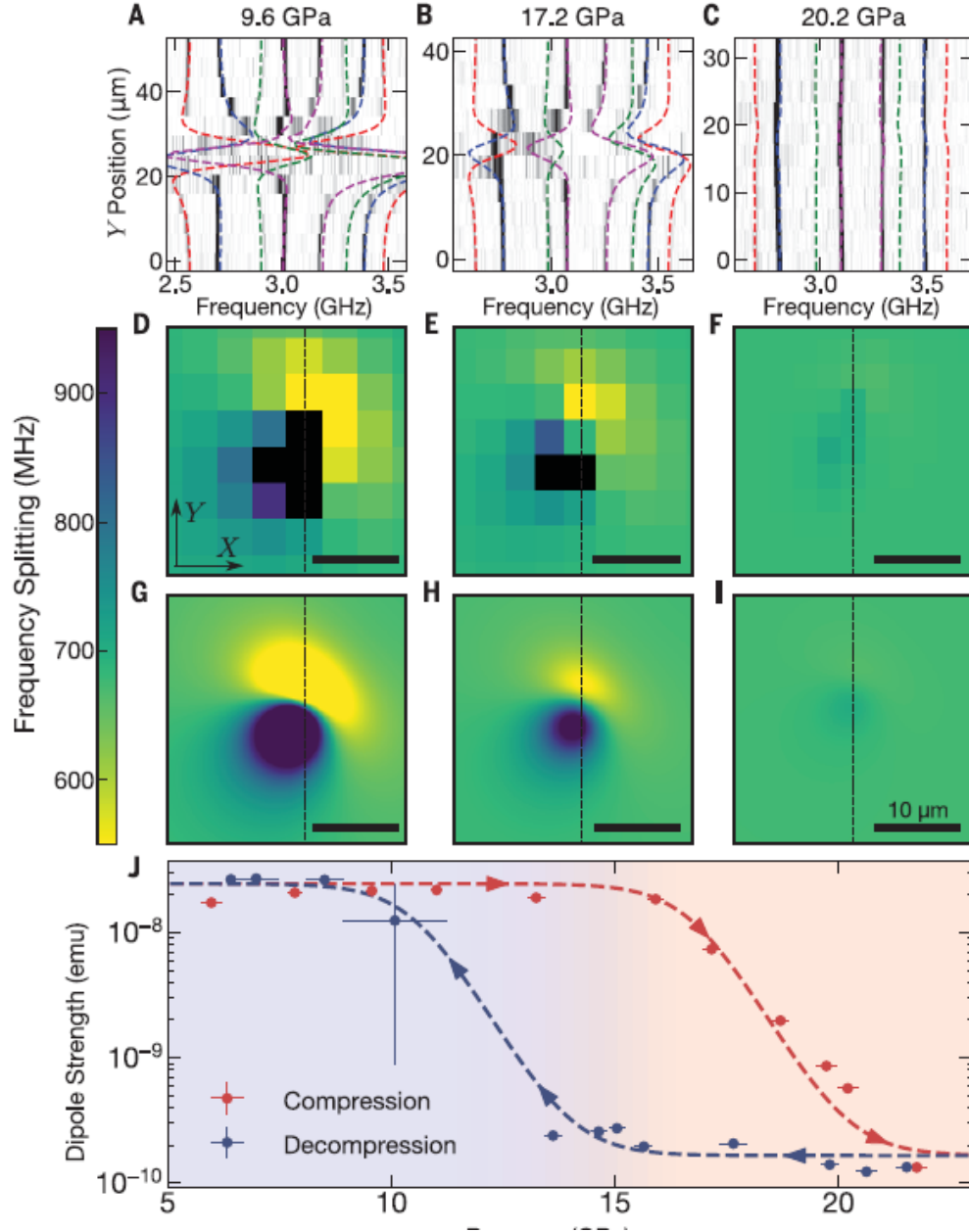


Figure 3. Imaging iron's $\alpha \leftrightarrow \epsilon$ phase transition. Applying an external magnetic field ($B_{\text{ext}} \sim 180$ G) induces a dipole moment in the polycrystalline iron pellet that generates a spatially varying magnetic field across the culet of the diamond anvil. By mapping the ODMR spectra across the culet surface, we reconstruct the local magnetic field that characterizes the iron pellet's magnetization. (A to C) Comparison between the measured ODMR spectra (dark regions correspond to resonances) and the theoretical resonance positions (different colors correspond to

different NV crystallographic orientations) across vertical spatial cuts (i.e., Y position indicates location along the black-dashed line shown in the two-dimensional scans below) at pressures of 9.6, 17.2, and 20.2 GPa, respectively (16:3:1 methanol/ethanol/water solution). (D to F) Map of the measured energy difference of a particular NV crystallographic orientation [blue lines in (A) to (C)]. Black pixels correspond to ODMR spectra where the splitting could not be accurately extracted owing to large magnetic field gradients (figure S12). (G to I) Theoretical reconstruction of the energy differences shown in (D) to (F) [23]. Data depicted in (A) to (C) are taken along the thin black dashed lines. (J) Measured dipole moment of the iron pellet as a function of applied pressure at room temperature, for both compression (red) and decompression (blue). Based on the hysteresis observed (~ 6 GPa), we find the critical pressure $P_c = 13.6 \pm 3.6$ GPa, in excellent agreement with previous studies [28].

on a Gd foil at ambient pressure, we find that the NV T_1 is nearly temperature independent in the paramagnetic phase, before exhibiting a kink and subsequent decrease upon entering the ferromagnetic phase (Figure 4D). We note two intriguing observations: first, one possible microscopic explanation for this behavior is that T_1 is dominated by Johnson-Nyquist noise from the thermal fluctuations of charge carriers inside Gd [34, 35]. Gapless critical spin fluctuations or magnons in the ordered phase, although expected, are less likely to cause this signal [23]. Second, we observe that the Curie temperature, as identified by T_1 -noise spectroscopy, is ~ 10 K higher than that observed via DC magnetometry (Figure 4D). Similar behavior has previously been reported for the surface of Gd [29, 36], suggesting that our noise spectroscopy could be more sensitive to surface physics.

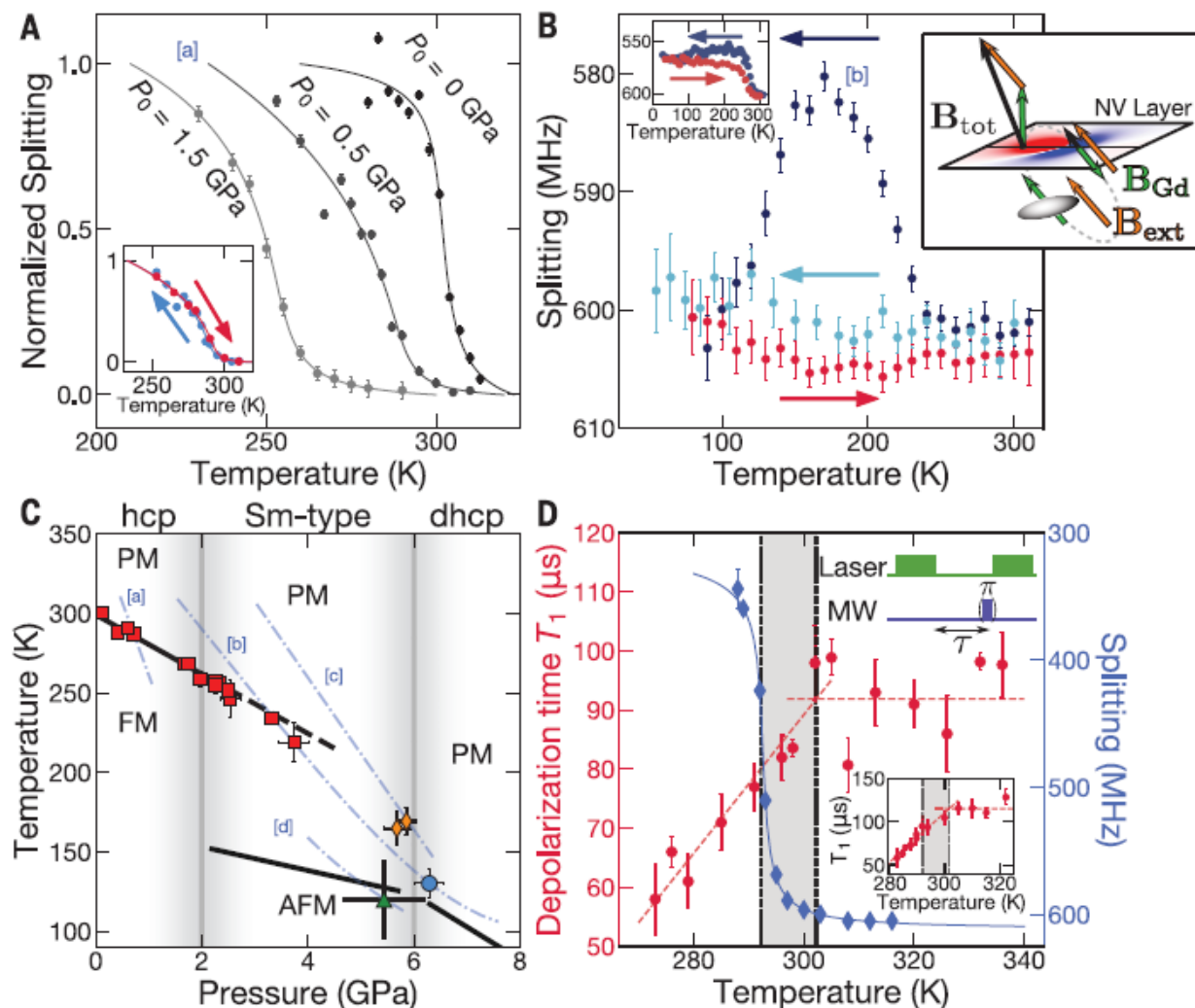


Figure 4. Magnetic P-T phase diagram of gadolinium. A ~ 30 mm by 30 mm by 25 mm polycrystalline Gd foil is loaded into a beryllium copper gasket with a cesium iodide pressure medium. An external magnetic field, $B_{\text{ext}} \sim 120$ G, induces a dipole field, B_{Gd} , detected by the splitting of the NVs [right inset, (B)]. (A) The FM Curie temperature T_C decreases with increasing pressure up to ~ 4 GPa. NV splittings for three P-T paths, labeled by their initial pressure P_0 , are shown. The P-T path for run [a] ($P_0 = 0.5$ GPa) is shown in (C). The cool-down (blue) and heat-up (red) of a single P-T cycle shows negligible hysteresis (inset). (B) If a P-T path starting in hcp is taken into the dhcp phase (at pressures ≥ 6 GPa) (30), the FM signal is lost and not reversible, as shown in (C) (path [b]). Upon cool-down (dark blue), we observe the

aforementioned Curie transition, followed by the loss of FM signal at 6.3 GPa, 130 K. But upon heat-up (red) and second cooldown (light blue), the FM signal is not recovered. When the pressure does not go beyond ~ 6 GPa, the FM signal is recoverable (left inset) [23]. (C) Magnetic P - T phase diagram of Gd. At low pressures, we observe the linear decrease of TC (black line) with slope -18.7 ± 0.2 K/GPa, in agreement with previous measurements [30]. This linear regime extends into the Sm-type phase (black dashed line) owing to the slow dynamics of the hcp \rightarrow Sm-type transition [30]. When starting in the Sm-type phase, we no longer observe a FM signal, but rather a small change in the magnetic field at either the transition from Sm-type to dhcp (orange diamonds) or from PM to AFM (green triangle), depending on the P - T path. The bottom two phase boundaries (black lines) are taken from [31]. (D) At ambient pressure, we observe a Curie temperature, $T_C = 292.2 \pm 0.1$ K, by using DC magnetometry (blue data). Using nanodiamonds drop-cast onto a Gd foil (and no applied external magnetic field), we find that the depolarization time (T_1) of the NVs is qualitatively different in the two phases (red data). T_1 is measured using the pulse sequence shown in the top right inset. The T_1 measurement on another nanodiamond exhibits nearly identical behavior (bottom inset).

Further stress characterization of other fluids and solids may provide insights into mechanical phenomena such as viscous flow, plastic deformation, and pressure-dependent yield strength. Such information is challenging to obtain by either numerical finite element simulations or more conventional experimental methods and may ultimately allow control of the deviatoric- as well as normal-stress conditions in high-pressure experiments [37].

The high sensitivity and close proximity of our sensor enables the measurement of signals in settings that are beyond the capabilities of existing techniques (Figure 1F). Such

settings include, for example, nuclear magnetic resonance (NMR) at picoliter volumes [38] and single-grain remnant magnetism [39], as well as phenomena that exhibit spatial textures such as magnetic skyrmions [4] and superconducting vortices [40].

Although our work uses NV centers, the techniques developed here can be readily extended to other atomic defects. For instance, recent developments on all-optical control of silicon-vacancy centers in diamond may allow for microwave-free stress imaging with improved sensitivities [41]. In addition, one can consider defects in other anvil substrates beyond diamond; indeed, recent studies have shown that moissanite (6H silicon carbide) hosts optically active defects that show promise as local sensors [41]. In contrast to millimeter-scale diamond anvils, moissanite anvils can be manufactured at centimeter or larger scales, and therefore support larger sample volumes that ameliorate the technical requirements of many experiments. Finally, the suite of sensing capabilities previously demonstrated for NV centers (i.e., electric, thermal, gyroscopic precession, etc.) can now straightforwardly be extended to high-pressure environments, opening up a large range of experiments for quantitatively characterizing materials at such extreme conditions.

References

- [1] G. Kucsko et al., *Nature* 500, 54–58 (2013).
- [2] P. Maletinsky et al., *Nat. Nanotechnol.* 7, 320–324 (2012).
- [3] J. Cai, F. Jelezko, M. B. Plenio, *Nat. Commun.* 5, 4065 (2014).
- [4] Y. Dovzhenko et al., *Nat. Commun.* 9, 2712 (2018).
- [5] A. Jayaraman, *Rev. Mod. Phys.* 55, 65–108 (1983).
- [6] H. Mao, X.-J. Chen, Y. Ding, B. Li, L. Wang, *Rev. Mod. Phys.* 90, 015007 (2018).
- [7] E. Wigner, H. Huntington, *J. Chem. Phys.* 3, 764–770 (1935).

- [8] H. Horii, S. Nemat-Nasser, *Philos. Trans. A Math. Phys. Eng. Sci.* 319, 337–374 (1986).
- [9] E. Gilioli, L. Ehm, *IUCrJ* 1, 590–603 (2014).
- [10] A. P. Drozdov, M. I. Eremets, I. A. Troyan, V. Ksenofontov, S. I. Shylin, *Nature* 525, 73–76 (2015).
- [11] M. Somayazulu et al., *Phys. Rev. Lett.* 122, 027001 (2019).
- [12] M. W. Doherty et al., *Phys. Rep.* 528, 1–45 (2013).
- [13] V. M. Acosta et al., *Phys. Rev. Lett.* 104, 070801 (2010).
- [14] J. R. Maze et al., *Nature* 455, 644–647 (2008).
- [15] F. Dolde et al., *Nat. Phys.* 7, 459–463 (2011).
- [16] P. Ovartchaiyapong, K. W. Lee, B. A. Myers, A. C. B. Jayich, *Nat. Commun.* 5, 4429 (2014).
- [17] M. W. Doherty et al., *Phys. Rev. Lett.* 112, 047601 (2014).
- [18] M. S. J. Barson et al., *Nano Lett.* 17, 1496–1503 (2017).
- [19] L. G. Steele et al., *Appl. Phys. Lett.* 111, 221903 (2017).
- [20] F. Casola, T. van der Sar, A. Yacoby, *Nat. Rev. Mater.* 3, 17088 (2018) Review Article.
- [21] T. Mittiga et al., *Phys. Rev. Lett.* 121, 246402 (2018).
- [22] P. Udvarhelyi, V. O. Shkolnikov, A. Gali, G. Burkard, A. Pályi, *Phys. Rev. B* 98, 075201 (2018).
- [23] E. Sterer, M. P. Pasternak, R. D. Taylor, *Rev. Sci. Instrum.* 61, 1117–1119 (1990).
- [24] G. Falkovich, *Fluid Mechanics* (Cambridge Univ. Press, ed. 2, 2018).
- [25] A. Dewaele, P. Loubeyre, M. Mezouar, *Phys. Rev. B Condens. Matter Mater. Phys.* 70, 094112 (2004).
- [26] S. Klotz, J.-C. Chervin, P. Munsch, G. Le Marchand, *J. Phys. D Appl. Phys.* 42, 075413 (2009).
- [27] R. Taylor, M. Pasternak, R. Jeanloz, *J. Appl. Phys.* 69, 6126–6128 (1991).

- [28] L. Oroszlány, A. Deák, E. Simon, S. Khmelevskiy, L. Szunyogh, *Phys. Rev. Lett.* 115, 096402 (2015).
- [29] A. Jayaraman, in *Metals*, vol. 1 of *Handbook on the Physics and Chemistry of Rare Earths* (Elsevier, 1978), pp. 707–747.
- [30] G. K. Samudrala, G. M. Tsoi, S. T. Weir, Y. K. Vohra, *High Press. Res.* 34, 385–391 (2014).
- [31] P. Hargraves, R. A. Dunlap, D. J. W. Geldart, S. P. Ritcey, *Phys. Rev. B Condens. Matter* 38, 2862–2864 (1988).
- [32] S. Chatterjee, J. F. Rodriguez-Nieva, E. Demler, *Phys. Rev. B* 99, 104425 (2019).
- [33] S. Kolkowitz et al., *Science* 347, 1129–1132 (2015).
- [34] As opposed to isolated NV samples, where T1 is limited by spin-phonon interactions.
- [35] H. Tang et al., *Phys. Rev. Lett.* 71, 444–447 (1993).
- [36] B. Feng, V. I. Levitas, R. J. Hemley, *Int. J. Plast.* 84, 33–57 (2016).
- [37] P. Kehayias et al., *Nat. Commun.* 8, 188 (2017).
- [38] D. R. Glenn et al., *Geochem. Geophys. Geosyst.* 18, 3254–3267 (2017).
- [39] L. Thiel et al., *Nat. Nanotechnol.* 11, 677–681 (2016).
- [40] M. Atatüre, D. Englund, N. Vamivakas, S.-Y. Lee, J. Wrachtrup, *Nat. Rev. Mater.* 3, 38–51 (2018).
- [41] S. Hsieh et al., *Imaging stress and magnetism at high pressures using a nanoscale quantum sensor*, Zenodo (2019); doi.org/10.5281/zenodo.3334404.

Acknowledgments

We gratefully acknowledge fruitful discussions with J. Analytis, R. Birgeneau, J. Choi, K. de Greve, M. Eremets, Z. Geballe, F. Hellman, A. Jarmola, J. Jeffries, I. Kim, M. Kunz, D.-H. Lee, S. Lewin, P. Maurer, R. Ramesh, G. Samudrala, E. Zepeda-Alarcon, and R. Zieve. We thank D. Budker, P. Fischer, and H. Zhou for a careful reading of the manuscript and helpful comments. We are especially grateful to M. Barson and M. Doherty for sharing their raw data on

stress susceptibilities. We thank C. Laumann for introducing us to the idea of integrating NV centers into diamond anvil cells.

Funding

This work was supported as part of the Center for Novel Pathways to Quantum Coherence in Materials, an Energy Frontier Research Center funded by the U.S. Department of Energy, Office of Science, Basic Energy Sciences under Award no. DE-AC02-05CH11231. N.Y.Y. acknowledges support from the David and Lucile Packard foundation and the W. M. Keck foundation. S.H. acknowledges support from the National Science Foundation Graduate Research Fellowship under grant no. DGE-1752814. T.J.S. and R.J. acknowledge support from the U.S. Department of Energy National Nuclear Security Administration under grant no. DE-NA0003842. V.I.L. and M.K. acknowledge support from the Army Research Office (grant W911NF-17-1-0225) and the National Science Foundation (grants CMMI-1536925 and DMR-1904830).

Author Contributions

S.H., P.B., C.Z., T.M., T.J.S., and T.O.H. performed the experiments and collected data. F.M., B.K., N.Z.R., S. Chatterjee, S. Choi, M.Z., J.E.M., and N.Y.Y. developed theoretical models and methodology. S.H, P.B., C.Z., T.M., T.O.H., F.M., B.K., and S. Chatterjee performed the data analysis. M.K. and V.I.L. performed the finite-element simulations. V.V.S. provided equipment and technical expertise for the diamond anvil cells. N.Y.Y. and R.J. conceived the study and supervised the project. All authors contributed to discussions of the data and to the writing of the manuscript.

Competing Interests

University of California (coinventors S.H., P.B., C.Z., T.M., T.J.S., F.M., B.K., S.C., J.E.M., R.J., and N.Y.Y.) filed for a provisional patent (62/782,262) that relates to sensing at high pressures using an apparatus that integrates defects in diamond with diamond anvil cells.

Data and Materials Availability

Published data are available on the Zenodo public database [42].

Supplementary Materials

Finite Element Simulations of the Stress Tensor

Using equations from elasticity theory under the finite element approach, a numerical simulation was coded in ABAQUS for the stress and strain tensor fields in the diamond anvil cell. The diamond anvil cell is approximately axially symmetric about the diamond loading axis, in this case the crystallographic (111) axis (i.e. the Z axis). This permits us to improve simulation efficiency by reducing the initially 3D tensor of elastic moduli to the 2D axisymmetric cylindrical frame of the diamond as follows. Initially, the tensor can be written in 3D with cubic axes $c_{11} = 1076$ GPa, $c_{12} = 125$ GPa, $c_{44} = 577$ GPa. Next, we rotate cubic axes such that the (111) direction is along the Z axis of the cylindrical coordinate system. Finally, the coordinate system is rotated by angle θ around the Z axis and the elastic constants are averaged over 360° rotation. The resulting elasticity tensor in the cylindrical coordinate system is

$$\begin{bmatrix} 1177.5 & 57.4 & 91 & 0 \\ 57.4 & 1211.6 & 57.4 & 0 \\ 91 & 57.4 & 1177.5 & 0 \\ 0 & 0 & 0 & 509.2 \end{bmatrix} [\text{GPa}].$$

The geometry of the anvil and boundary conditions (Figure S8) are as follows:

1. The top surface of the anvil is assumed to be fixed. The distribution of stresses or displacements along this surface does not affect our solution close to the diamond culet line AB.
2. The normal stress (σ_{ZZ} along the line AB is taken from the experimental measurements (main text Figure 2A and S9). The pressure-transmitting medium/gasket boundary runs along the innermost $47 \mu m$ of this radius.
3. Along the pressure-transmitting medium/anvil boundary ($r \leq 47 \mu m$) and also at the symmetry axis $r = 0$ (line AE) shear stress σ_{RZ} is zero. Horizontal displacements at the symmetry axis are also zero.
4. Normal and shear contact stresses along all other contact surfaces are determined from the best fit to the mean in-plane stress distribution $\sigma_{\perp} = 0.5(\sigma_{RR} + \sigma_{\theta\theta})$ measured in the experiment (main text Figure 2A and Figure S9). We chose to fit to σ_{\perp} rather than to other measured stresses is because it has the smallest noise in experiment. With this, the normal stress on the line BD with the origin at point B is found to be

$$\sigma_c = 3.3 \times 10^5 x^4 - 7.5 \times 10^4 x^3 + 4.5 \times 10^3 x^2 - 10^2 x + 4.1, \quad (S27)$$

Where σ_c is in units of GPa, and the position x along the lateral side is in units of mm.

The distribution of the normal stresses is shown in Figure S8B and Figure S10.

5. At the contact surface between the gasket and the anvil, a Coulomb friction model is applied. The friction coefficient on the culet is found to be 0.02 and along the inclined surface of the anvil (line BD) is found to vary from 0.15 at point B to 0.3 at $80 \mu m$ from the culet. The distribution of shear stresses is shown in Figure S8C and Figure S10.

6. Other surfaces not mentioned above are stress-free.

The calculated distributions of the stress tensor components near the tip of the anvil are shown in Figure S11.

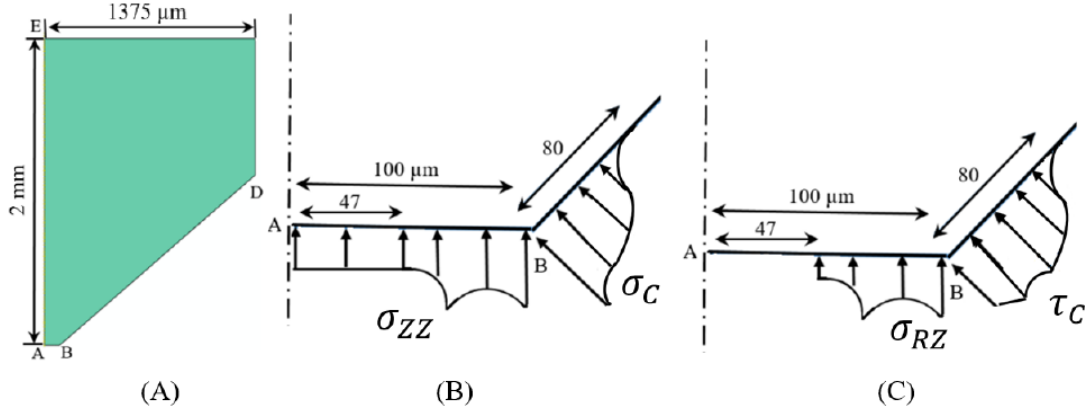


Figure S8. (A) Diamond geometry, (B) anvil tip with distribution of the applied normal stress, (C) distribution of the applied shear stress. Normal stress σ_{ZZ} at the culet and zero shear stress σ_{RZ} along the pressure-transmitting medium/anvil boundary ($r \leq 47 \mu\text{m}$) are taken from experiment. Normal and shear contact stresses along all other contact surfaces are determined from the best fit of the mean in-plane stress distribution $\sigma_{\perp} = 0.5(\sigma_{RR} + \sigma_{\theta\theta})$ to experiment (main text Figure 2A and Figure S9)

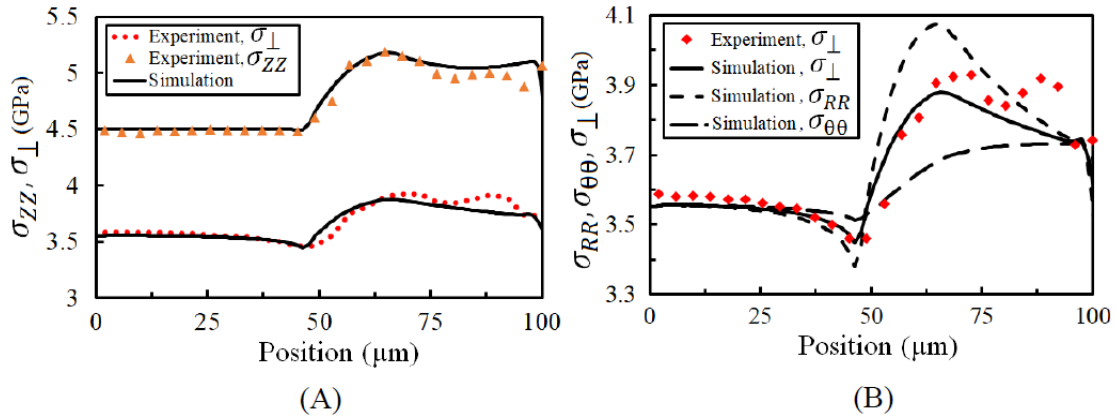


Figure S9. (A) Distribution of applied normal stress σ_{ZZ} and the mean in-plane stress σ_{\perp} along the culet surface of the diamond from the experiment and FEM simulations. (B) Distribution of

the mean in-plane stress σ_{\perp} (experimental and simulated) as well as the simulated radial σ_{RR} and circumferential $\sigma_{\theta\theta}$ stresses along the culet surface of the diamond.

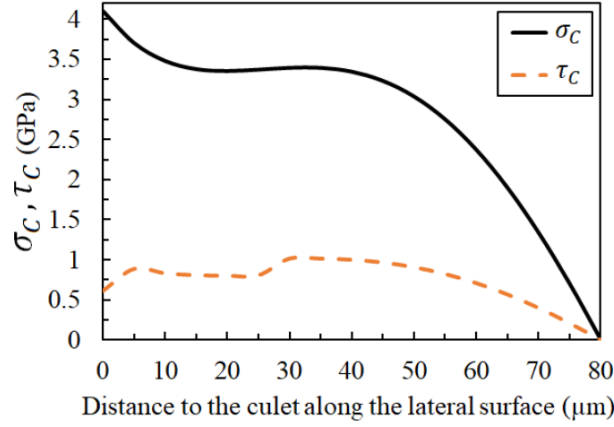


Figure S10. Distribution of applied normal and shear stress along the lateral surface of the diamond determined from the best fit of the mean in-plane stress distribution σ_{\perp} to experiment (main text Figure 2A and Figure S9).

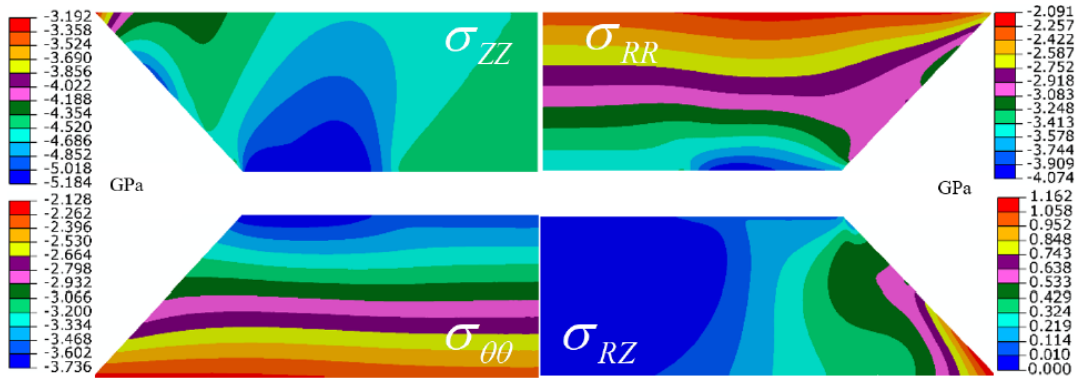


Figure S11. Calculated distributions of the components of stress tensor in the anvil for $r < 150$ and $z < 475 \mu\text{m}$.

CHAPTER 6. CONCLUSION

1. In chapter 2 the behavior of a copper sample under HPT in a quasi-constraint configuration is studied using FEM method. The effect of different contact conditions and material properties on the distribution of different fields and torque-rotation angle response of the sample is shown.

Results show that the torque-rotation angle behavior of the sample is highly dependent on the friction condition in the flash region, which was ignored in the analyses of experiments due to its small size compared to the initial diameter of the sample. Also, the torque-rotation angle curve is practically independent of the saturation strain m . Both results show that the torque-rotation angle cannot be used for determining the stress-strain curve of materials.

Our simulations showed that determination of m in HPT experiments based on determination of plastic strain required for saturation of the hardness contained large errors. At the same time the methods for determining the stress-strain curves for the homogeneous compression test of a special sample is strict and gives $m=1$ for preliminary-treated material and an extrapolated value of $m=1.57$ for annealed copper.

2. In chapter 3 strain induced $\alpha \rightarrow \omega$ phase transformation in Zr was studied in RDAC. During the rotation of an anvil at fixed force, the radial shear (and twisting) stress increases at the center of a sample due to a stronger ω phase and corresponding to material hardening of the $\alpha + \omega$ phase mixture during PT, and the sample thickness reduces due to the material radial flow. This leads to a drastic increase in the pressure gradient and pressure at the center of sample. In this manner, we reproduced the pressure self-multiplication effect observed experimentally.

Due to the radial material flow, the ω phase can be observed in the region where pressure is lower than the minimum pressure for strain-induced PT, p_{ε}^d , which may lead to misinterpretation of the experimental data for determination of the minimum PT pressure.

By comparison between the process with rotation and without rotation of an anvil, we find that the volume fraction of the ω phase is very small at the small normal applied load, but after torsion at the same load (i.e. the averaged pressure), a large transformed zone and volume fraction of the ω phase can be obtained. If an increase in the volume fraction of the ω phase in DAC is desired, the only way to produce plastic straining is to increase the applied load σ_n , which leads to higher pressure in both diamond and sample, in comparison to PT in the RDAC. This is the main reason for reporting the experimental PT pressure difference with and without torsion.

3. In chapter 4, we suggested a novel coupled experimental-theoretical-computational approach that allowed us to extract complete information about elastoplastic properties and friction rules, as well as all complex tensorial fields for materials compressed in a DAC under extreme pressure. In particular, we refined, calibrated, and verified models for elastoplastic behavior of a sample and contact friction for W up to 400 GPa and reconstruct fields of all components of stress and large plastic strain tensors in W and diamond. In addition to quantitative information on the pressure dependence of the yield strength and friction, as well as higher-order elastic constants, we justify some general unique properties of elastoplastic behavior under very large strains and pressures:

Despite the generally accepted strain-induced anisotropy, strain hardening, and path-dependent plasticity, W after large plastic strains behaves isotropically and does not exhibit strain hardening and path-independence.

Despite the μm -sized sample thickness and huge stress ($5 \text{ GPa}/\mu\text{m}$) and plastic strain gradients, scale-independence of elastoplastic properties is found.

The field of all components of the stress tensor in diamond are the basis for the development of criteria for fracture of diamond. We illustrated the concept by considering fracture due to compression along one of the experimentally observed directions. This is an important step which will allow optimization of the design of anvils and loading conditions for further increase in achievable pressure.

4. In the final chapter, a novel method to determine stress components as an in-situ measurement was introduced. A procedure was proposed to simplify a 3D geometry into a 2D-axisymmetric formulation. Then we showed that our novel coupled experimental-theoretical-computational approach can be used to not only determine the contact condition but also validate the experimental stress distribution along the contact surface. Besides, this method can provide the fields of all stress tensor components within the entire diamond.